

Charles University in Prague
Faculty of Mathematics and Physics

DIPLOMA THESIS



Martin Slezák

The source of monoenergetic electrons for the monitoring of spectrometer in the KATRIN neutrino experiment

Nuclear Physics Institute
Academy of Sciences of the Czech Republic

Supervisor: Mgr. Drahoslav Vénos, CSc.

Study programme: Physics

Specialization: Nuclear and particle physics

Prague 2011

Acknowledgements

I would like to express my sincere gratitude to Drahoslav Vénos for his professional approach, unremitting support, valuable ideas and comments during writing of this diploma thesis. I also greatly appreciate the support, thoughts and stimulating conversations from Otokar Dragoun. I wish to thank Ondřej Lebeda for help with the preparation of the $^{83}\text{Rb}/^{83\text{m}}\text{Kr}$ gamma sources. I am grateful to Stanislav Pospíšil, Carlos Granja, Jan Jakubek and Jan Žemlička for the possibility to use the Timepix detector at IEAP, for explaining its functions and for help with the measurements and analysis. I also gratefully acknowledge the willingness of the entire electron spectroscopy group at NPI Rež and people involved in KATRIN for discussions about the fundamentals of the KATRIN experiment, the monitor spectrometer and neutrino physics. Above all, I am indebted to my family for their everlasting support and encouragement.

I declare that I carried out this diploma thesis independently, and only with the cited sources, literature and other professional sources.

I understand that my work relates to the rights and obligations under the Act No. 121/2000 Coll., the Copyright Act, as amended, in particular the fact that the Charles University in Prague has the right to conclude a license agreement on the use of this work as a school work pursuant to Section 60 paragraph 1 of the Copyright Act.

Prague, 4 April 2011

Martin Slezák

Název práce: Zdroj monoenergetických elektronů pro monitorování spektrometru v neutrinovém experimentu KATRIN

Autor: Martin Slezák

Katedra / Ústav: Ústav jaderné fyziky, Akademie věd České republiky, v.v.i.

Vedoucí diplomové práce: Mgr. Drahošlav Vénoš, CSc., Oddělení jaderné spektroskopie

Abstrakt: Mezinárodní projekt KATRIN (KARlsruhe TRItium Neutrino experiment) je experiment nové generace využívající beta rozpad tritia. Je navržen, aby umožnil změřit hmotnost elektronového antineutrina pomocí unikátního elektronového spektrometru s citlivostí $0.2 \text{ eV}/c^2$, což znamená zlepšení o jeden řád oproti stávajícím výsledkům. Významná část měření bude spočívat v nepřetržitém přesném monitorování vysokého napětí hlavního spektrometru KATRIN. Monitorování bude uskutečňováno s využitím elektronů vnitřní konverze emitovaných z pevného zdroje založeného na rozpadu ^{83}Rb . Vlastnosti několika těchto zdrojů jsou studovány v této práci pomocí polovodičové gama spektroskopie. Zaprvé je popsáno měření přesné energie jaderného přechodu 9.4 keV pozorovaného v rozpadu ^{83}Rb , ze které je odvozena energie konverzních elektronů. Zadruhé je popsáno měření rozložení aktivity pevných zdrojů pomocí detektoru typu Timepix. Nakonec je popsáno měření retence rozpadového produktu ^{83}Rb , isomerního stavu $^{83\text{m}}\text{Kr}$, v pevných zdrojích.

Klíčová slova: KATRIN, neutrino, gama spektroskopie, rubidium, Timepix

Title: The source of monoenergetic electrons for the monitoring of spectrometer in the KATRIN neutrino experiment

Author: Martin Slezák

Department: Nuclear Physics Institute, Academy of Sciences of the Czech Republic

Supervisor: Mgr. Drahošlav Vénoš, CSc., Department of nuclear spectroscopy

Abstract: The international project KATRIN (KARlsruhe TRItium Neutrino experiment) is a next-generation tritium beta decay experiment. It is designed to measure the electron antineutrino mass by means of a unique electron spectrometer with sensitivity of $0.2 \text{ eV}/c^2$. This is an improvement of one order of magnitude over the last results. Important part of the measurement will rest in continuous precise monitoring of high voltage of the KATRIN main spectrometer. The monitoring will be done by means of conversion electrons emitted from a solid source based on ^{83}Rb decay. Properties of several of these sources are studied in this thesis by means of the semiconductor gamma-ray spectroscopy. Firstly, measurement of precise energy of the 9.4 keV nuclear transition observed in ^{83}Rb decay, from which the energy of conversion electrons is derived, is reported. Secondly, measurement of activity distribution of the solid sources by means of the Timepix detector is described. Finally, a report on measurement of retention of ^{83}Rb decay product, the isomeric state $^{83\text{m}}\text{Kr}$, in the solid sources is given.

Keywords: KATRIN, neutrino, gamma spectroscopy, rubidium, Timepix

Contents

Preface	1
1. Neutrinos - theoretical and experimental overview	3
1.1. Beta decay.....	3
1.2. Neutrino oscillations.....	5
1.3. Importance of neutrino mass.....	6
1.4. Important historical milestones.....	7
1.5. KATRIN experiment.....	8
1.5.1. The MAC-E filter.....	9
1.5.2. Monitoring of the KATRIN experiment.....	10
2. Solid $^{83}\text{Rb}/^{83\text{m}}\text{Kr}$ sources	12
2.1. ^{83}Rb production method.....	12
2.2. Vacuum evaporation method.....	13
2.3. Implantation method.....	13
3. Precise energy of 9.4 keV γ-ray transition in $^{83\text{m}}\text{Kr}$	14
3.1. Experimental method.....	15
3.2. Measurement apparatus and setup.....	15
3.3. Systematic effects.....	17
3.3.1. Satellite lines.....	17
3.3.2. Radiative Auger effect.....	19
3.4. Description of lines.....	23
3.5. Spectra analysis.....	27
3.6. Measurement results.....	33
3.7. Determination of systematic error.....	38
3.8. Discussion of results.....	39
3.9. Conclusion.....	39
4. Rubidium activity distribution	40
4.1. Timepix measurement.....	40
4.2. Manual scan equipment measurement.....	45
4.3. ^{83}Rb areal density.....	48
4.4. Discussion of results.....	49
4.5. Conclusion.....	51
5. $^{83\text{m}}\text{Kr}$ retention	52
5.1. Method 1: Comparison of 32 keV and 9.4 keV lines intensities.....	52
5.1.1. Theory.....	52
5.1.2. Measurement results and discussion.....	53
5.2. Method 2: Closeable chamber.....	54
5.2.1. Method description.....	54
5.2.2. Correction for ^{83}Rb decay.....	54
5.2.3. $^{83\text{m}}\text{Kr}$ transient equilibrium with ^{83}Rb in closed chamber.....	56
5.2.4. Correction for finite volume of closed chamber.....	57
5.2.5. Monte Carlo simulation to improve inverse square law dependence..	60
5.2.6. Retention measurement results and discussion.....	64
5.3. Conclusion.....	66
6. Conclusion	67
References	68

Preface

In a few recent decades effort put into research in particle physics led to remarkable successes. One of the major achievements is the direct detection of elementary particle called neutrino and, in addition, establishment of existence of its mass. Neutrino was postulated by W. Pauli in 1930 in order to explain the continuous energy spectrum of electrons emitted in β -decay. Without taking this particle into consideration, the process seems to be violating the fundamental conservation law of energy and momentum and together with that also the conservation law of angular momentum. Later the experiment by C. Cowan and F. Reines [1] directly confirmed the existence of such particle and established Pauli's proposal as a correct one.

Since then neutrinos were incorporated into a theoretical model, which was developed and improved over time. Now at its present state we recognize it as the Standard Model of particle physics (SM). It is known that one of the fundamental interactions, the weak interaction, is responsible for the β -decay and it is also included in the model. Despite the remarkable success in prediction of various phenomena with the SM, which were confirmed by experiments, it is generally believed this theoretical framework is not the final one and a deeper theory lies underneath.

Specifically, the neutrinos are assumed to be massless in the SM [2]. Although it is not difficult to add their masses into the theory, there are no means of predicting the actual values of the masses. They have to be included as free parameters, which increases the already high number of 17 free parameters [3] in the model. Evidence or even precise knowledge of the neutrino masses would allow insights on possible suitable theories beyond the SM and besides particle physics it would also have impact on astrophysics and cosmology.

At present day it is known there exist exactly three flavours of weak-interacting neutrinos from observation of decay width of the Z-boson [4], which is the mediating particle of neutral currents of the weak interaction. It can be shown that if at least one neutrino mass is nonzero the flavours can be seen transformed into each other, a process known as neutrino oscillations. Any persuasive evidence for the oscillations among any flavour would then confirm non-zero neutrino mass. Observation of neutrino oscillations was indeed confirmed by experiments with almost total exclusion of other phenomena possibly explaining the results [5, 6, 7, 8, 9]. Nevertheless, it should be noted that from such positive results only differences of neutrino masses squared can be extracted and there is no possibility to obtain the individual values. From the results only the lower limit on heaviest neutrino of 0.05 eV could be established [5].

Different processes have to be investigated to establish the absolute value of the neutrino mass. Among such processes one is especially attractive for investigation; it is the β -decay itself. Already in 1934 E. Fermi showed [10] that it is possible to extract the neutrino mass from the shape of the continuous energy spectrum of β -electrons, specifically at the endpoint region. Extremely suitable for experiments is the β^- -decay of tritium. By measuring the corresponding energy spectrum the electron antineutrino mass can be extracted. So far the experiments, despite great advance in both technology and systematic effects elimination, have always given only upper limits for the mass. The current limit is $2 \text{ eV}/c^2$ [11]. It is the task of new generation experiment KATRIN (KARlsruhe TRITium Neutrino experiment) to push the sensitivity on neutrino mass down to $0.2 \text{ eV}/c^2$ [12].

Such sensitivity requires long-term measurement with as stable conditions as possible. Much effort is thus required on monitoring the conditions. As described in more detail in the next chapter, the measurement of tritium β -spectrum in KATRIN will

be possible with a special type of electrostatic spectrometer, the MAC-E filter (Magnetic Adiabatic Collimation combined with Electrostatic filter). One of crucial parts of the measurement will be the task to monitor the retarding high voltage (18 kV) applied to this main spectrometer with ppm (parts per milion) sensitivity.

One method to accomplish this is as follows. The same type of spectrometer (former University of Mainz spectrometer used for measurement of the neutrino mass), denoted monitoring spectrometer, is set to common retarding voltage with the main spectrometer. The monitoring spectrometer is then equipped with a stable source of mono-energetic electrons. Energy of these electrons is measured by varying the voltage on the source. Any change in this energy from the expected one points to a possible change of voltage of the main spectrometer.

Conversion electrons emitted from decay of ^{83m}Kr with energy 800 eV below the tritium spectrum endpoint can be used for this purpose [12]. This krypton isomer has a half-life of only 1.8 hours [13] and has to be replenished. The replenishment is provided by decay of ^{83}Rb , which has a sufficiently long half-life of 86.2 days [13]. A radioactive source made by ^{83}Rb atoms thus provides the necessary mono-energetic electron source for monitoring in the KATRIN experiment.

It is the purpose of this diploma thesis to report on studies of properties of several radioactive sources of such kind. The thesis is organized as follows.

In the first chapter a brief overview of history of neutrino physics, which led to present state of particle physics with non-zero mass neutrinos, is given. Also described is the quantum mechanical treatment of neutrino oscillations and summary of results of experiments which confirmed existence of this effect. Next, the importance of knowledge of the value of neutrino mass is briefly pointed out. As a last part the KATRIN experiment is described with emphasis on the monitoring task.

The second chapter gives a description of the radioactive sources which were under study, their production and measured activities.

The third chapter deals with the task of determination of precise energy of the 9.4 keV γ -ray transition in ^{83m}Kr . The energy of conversion electrons is derived from the energy of the corresponding nuclear transition. For systematic checks and possibly for absolute calibration of the monitoring (or main) spectrometer in KATRIN it is required to know this energy with sub-eV precision. Current experimental data do not satisfy this requirement. Specifically, in this chapter fine effects which may have influenced the energy determination are investigated and taken into account and the energy of 9.4 keV γ -ray transition is presented as a result.

The fourth chapter deals with pixel detector measurement of activity profile of the individual sources. This information is necessary for proper fine adjustment of position of the source in the spectrometer. Together with that the maximum ^{83}Rb atoms areal density can be determined. Knowledge on this provides a check in case of sources produced by implantation whether serious local damages in the source substrate can or can not be expected.

In the fifth chapter γ -spectroscopy measurement of the so-called krypton retention of the ^{83}Rb sources is reported. The retention is a property which is given by the ratio of number of ^{83m}Kr atoms decaying in the source to the number of those produced by decay from ^{83}Rb (the rest escapes the source into free space). In the MAC-E filter the source is expected to be placed in a limited space and only electrons emitted from the source can reach the spectrometer detector. Knowledge on the number of electrons leaving the source thus provides an important information on the detector load.

The last chapter briefly summarizes the results and gives a commentary on overall applicability of the sources in monitoring of the KATRIN experiment.

1. Neutrinos - theoretical and experimental overview

1.1. Beta decay

The nuclear β -decay, which played the main role during process of discovery of neutrinos, is a decay of isotope X with atomic number Z and mass number A into another isotope Y



This mode is known as β^- -decay as negative charged electrons are produced. Also other two modes for the decay are possible, namely β^+ -decay



and electron capture from atomic subsheel of X



On the quark level the process (1) is understood as decay of a down quark into an up quark



The other modes (2) and (3) can be understood in a analogous way. Such three-particle decay ensures the observed continuous energy spectrum of electrons as both the electron and the neutrino share the released energy. Assuming the (anti)neutrino to be a fermion with spin $\frac{1}{2}$ also conservation of angular momentum is guaranteed¹. It can be shown from simple kinematic considerations and Lorentz invariance that the electron energy spectrum has a maximum E_0 determined purely by masses of the particles (and/or nuclei) involved [3]. This maximum is called the endpoint of the spectrum. As the electrons are relativistic in this process, quantum field theory (QFT) treatment of its dynamics is necessary.

Without going into many details of the theory, which can be found elsewhere [3], let us state that in QFT the fermions are described by four-component wavefunctions $\psi(x)$ which obey the Dirac equation. These wavefunctions become operators on Fock space as a result of quantization procedure. The interactions of particles are described by the interaction Hamiltonian or, equivalently, the interaction Lagrangian density operator. Currently, the decay (4) is described by the corresponding part of electro-weak interaction Lagrangian in the Glashow - Weinberg - Salam model. It can be shown that for low energies this Lagrangian reduces effectively to an extended version of the one originally written down by E. Fermi.

The reduced Lagrangian describes β^- -decay in eq. (4) as four-point interaction (also known as the V-A theory) [3]

¹ E.g. in β^- -decay decay of carbon ${}^{14}_6\text{C} \rightarrow {}^{14}_7\text{N}$ existence of only one spin $\frac{1}{2}$ particle in the final state would point to non-conservation of angular momentum as spin of ${}^{14}_6\text{C}$ is 0 and spin of ${}^{14}_7\text{N}$ is 1 [14].

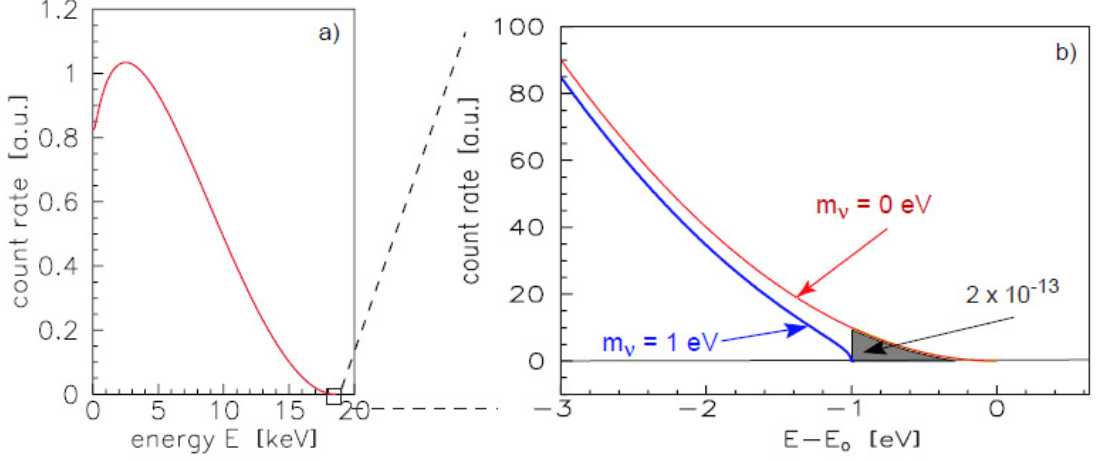


Fig. 1. Electron energy spectrum of tritium β -decay: a) complete, b) endpoint region with signature of neutrino mass of $1 \text{ eV}/c^2$. The number indicates fraction of electrons which falls into the filled region.

$$\mathcal{L} = \frac{G_F}{\sqrt{2}} [\bar{\psi}_e \gamma_\mu (1 - \gamma_5) \psi_\nu] [\bar{\psi}_u \gamma^\mu (1 - \gamma_5) \psi_d], \quad (5)$$

where G_F is the Fermi constant, ψ_i are the wavefunctions of the corresponding particles, γ_μ are the Dirac matrices in standard representation and the bar represents Dirac conjugation. A slight modification of eq. (5) is needed when considering nucleons instead of quarks due to renormalization effects in quantum chromodynamics.

From the theory it is possible to obtain the β -decay rate for production of an electron in energy interval between E and $E + dE$ in the form

$$\frac{dN}{dt dE} = C F(Z, E) p(E + m_e c^2) (E_0 - E) \sqrt{(E_0 - E)^2 - m_\nu^2} \Theta(E_0 - E - m_\nu), \quad (6)$$

where C is a constant, $F(Z, E)$ is a correction function, which takes into account the Coulomb interaction between the electron and the nucleus, p is the electron momentum, E is the electron kinetic energy, m_e and m_ν are masses of the electron and the neutrino and the Heaviside step function Θ assures energy conservation. In the result in eq. (6) the recoil of the daughter nucleus is neglected. The example of the energy spectrum in eq. (6) for tritium is shown in Fig. 1 with signature of non-zero neutrino mass of $1 \text{ eV}/c^2$ as taken from [12].

If there is a possibility for the daughter atom to end in an excited state after the decay (atomic shell and rotational-vibrational excitations) the formula (6) has to be modified in order to take these effects into account. A modification also has to be made when neutrino mixing (see next section) takes place, see [2], eq. (6.32). However, as long as the experimental resolution is larger than the mass differences of two neutrino states the resulting spectrum can be analysed in terms of a single observable, the electron antineutrino mass.

There are certain demands on possible isotopes as sources for β -electrons. Extracting the neutrino mass from the β -spectrum is extremely advantageous for tritium. As both the constant C and the function F are independent of m_ν the dependence of spectral shape on m_ν in eq. (6) is given by the phase space factor only. Therefore, the process is based only on kinematical conservation laws and is completely model-independent.

Together with that no assumption of the nature of neutrino, i.e. whether it is a Dirac or a Majorana particle² [2] is made.

As can be seen from Fig. 1 only a very small fraction of electrons falls within the region of interest. From eq. (6) follows that lowering the endpoint energy increases this fraction. Therefore, tritium with its second lowest endpoint energy of 18.6 keV is one of the most suitable isotopes [12]. Its half-life of 12.3 years is sufficiently short. Moreover, tritium and its daughter product have simple electron shell configurations. The Coulomb corrections and excitation states can be calculated relatively simply with enough precision. Also, due to small Z of tritium, the inelastic scattering cross-section for the electrons is small which also improves the fraction of no-loss electrons which can be detected. Finally, the decay is a super-allowed transition resulting in no need for corrections from nuclear transition matrix elements.

1.2. Neutrino oscillations

The phenomenon of neutrino oscillations is closely related to existence of non-vanishing neutrino mass. As the quantum mechanical derivation is straightforward and simple it is described here in more detail to explicitly show the origin of the relationship. Namely, in case of such non-vanishing mass the weak flavour and mass eigenstates are not necessarily identical. We will closely follow the derivation based on assumption of propagation of neutrinos as free particles (i.e. plane waves) as described e.g. in [2].

Let us have n orthonormal flavour neutrino eigenstates $|\nu_\alpha\rangle$ and n mass eigenstates $|\nu_k\rangle$. These states are connected via unitary matrix U (the bar represents antineutrino states)

$$|\nu_\alpha\rangle = \sum_k U_{\alpha k} |\nu_k\rangle, \quad |\bar{\nu}_\alpha\rangle = \sum_k U_{\alpha k}^* |\bar{\nu}_k\rangle. \quad (7)$$

The mass eigenstates are stationary states and their dependence on time t and space coordinate x with energy E_k is expressed in the form

$$|\nu_k(x, t)\rangle = e^{-iE_k t} |\nu_k(x, 0)\rangle = e^{i(px - E_k t)} |\nu_k\rangle, \quad (8)$$

assuming flavour neutrinos with momentum p emitted by a source positioned at $x = 0$. The neutrinos are assumed to be highly relativistic, i.e. $p \gg m_k$ and $E \approx p$ as flavour neutrino energy (with $c = 1$). This means for the energy E_k

$$E_k = \sqrt{m_k^2 + p_k^2} \approx p_k + \frac{m_k^2}{2p_k} \approx E + \frac{m_k^2}{2E}. \quad (9)$$

From eq. (7) and (8) follows that neutrinos with flavour α will develop in time t into the state described by

$$|\nu_\alpha(x, t)\rangle = \sum_k U_{\alpha k} e^{i(px - E_k t)} |\nu_k\rangle = \sum_{k, \beta} U_{\alpha k} U_{\beta k}^* e^{i(px - E_k t)} |\nu_\beta\rangle, \quad (10)$$

² Since neutrino has no electric charge it is yet unclear whether it is its own antiparticle (Majorana particle) or not (Dirac particle). Investigations are underway to resolve this puzzle [15, 16, 17, 18, 19].

where we have utilized the unitarity of U and reverted eq. (7). The transition probability is then

$$P(\alpha \rightarrow \beta)(t) = \left| \langle \nu_\beta | \nu_\alpha(x, t) \rangle \right|^2 = \sum_{k,j} U_{\alpha k} U_{\alpha j}^* U_{\beta k} U_{\beta j} e^{-i(E_k - E_j)t}. \quad (11)$$

We now utilize eq. (9) and define the distance between source and detector as $L \equiv ct = t$ and we get

$$P(\alpha \rightarrow \beta)(L) = \sum_k |U_{\alpha k} U_{\beta k}|^2 + 2 \operatorname{Re} \sum_{j>k} U_{\alpha k} U_{\alpha j}^* U_{\beta k} U_{\beta j} \exp\left(-i \frac{\Delta m_{kj}^2 L}{2E}\right) \quad (12)$$

with $\Delta m_{kj}^2 \equiv m_k^2 - m_j^2$. Finally, assuming CP invariance (meaning the coefficients $U_{\alpha i}$ are real)

$$\begin{aligned} P(\alpha \rightarrow \beta)(L) &= \sum_k U_{\alpha k}^2 U_{\beta k}^2 + 2 \sum_{j>k} U_{\alpha k} U_{\alpha j} U_{\beta k} U_{\beta j} \cos\left(\frac{\Delta m_{kj}^2 L}{2E}\right) \\ &= \delta_{\alpha\beta} - 4 \sum_{j>k} U_{\alpha k} U_{\alpha j} U_{\beta k} U_{\beta j} \sin^2\left(\frac{\Delta m_{kj}^2 L}{4E}\right) \end{aligned} \quad (13)$$

From this important result we indeed see oscillatory behaviour as a function of L/E . The oscillations will occur only if at least one neutrino mass is non-zero and if there is a mixing between individual flavours (meaning non-diagonal terms in U). Besides, measuring the oscillation probability P allows one to determine only the differences of masses squared and thus no absolute neutrino mass values.

Experimental detection of neutrino oscillations can be done in two ways. Firstly, it is observed whether less than the expected number of neutrinos of a specific flavour is detected (disappearance mode). In this mode also neutrino energy spectrum shape changes can be searched for. Secondly, searches for possible new flavours, which do not exist in the original beam, are done or enhancement of an existing flavour is searched for (appearance mode). In this mode identification of flavour relies on detection of the corresponding charged leptons produced in charged current interactions with hadrons

$$\nu_l + N \rightarrow l + N', \quad l \equiv e, \mu, \tau. \quad (14)$$

1.3. Importance of neutrino mass

The non-vanishing neutrino mass has great impact on particle physics, cosmology and astrophysics. As said before in the SM neutrinos are assumed to be massless. Masses of charged leptons and quarks are generated via the Higgs mechanism, but they are arbitrary and their pattern has no natural explanation in the SM [3]. The same mechanism can be applied also to neutrinos after introducing their right-handed form into the theory but this procedure has the same imperfection as for the charged leptons. Therefore, non-zero neutrino masses point to new physics beyond the SM.

Some theories work with the so-called see-saw effect as one of the mechanisms for neutrino mass generation [20, 21, 22]. In the first type of see-saw a heavy right-handed neutrino is introduced in order to get very light left-handed one. This mechanism requires hierarchical pattern of the three light neutrino masses, i.e. $m_1 \ll m_2 \ll m_3$. The second type of see-saw predicts existence of a new Higgs triplet and as a result more degenerate or quasi-degenerate neutrino mass pattern, i.e. $m_1 \approx m_2 \approx m_3$. Clearly distinction of which pattern is the correct one, which KATRIN experiment is capable of, would point to the right way to go beyond the SM.

In cosmology neutrinos play also an important role. It is predicted there should be about 10^9 times more neutrinos than baryons to be remaining from the Big Bang [23]. These relic neutrinos could thus act as a neutrino hot dark matter³ in the evolution of the so-called large scale structures. The corresponding cosmological models are strongly dependent on relative amounts of this hot dark matter and cold dark matter, for which candidates such as super-symmetric particles are considered. Determination of neutrino contribution to the total dark matter content of the universe is thus important for understanding of such structures.

Neutrino masses are crucial in studies of ultra-high energy (UHE) cosmic rays [24, 25]. Proton events with energy of more than 10^{20} eV have been reported. These must have been produced at local distances up to ~ 50 Mpc as the so-called Greisen - Zatsepin - Kuzmin cutoff should eliminate all UHE protons coming from larger distances via their interaction with photons of the cosmic microwave background and leave only protons with energy lower than $\sim 4 \times 10^{19}$ eV. One possible explanation for such UHE events could be in the so-called Z-burst effect: interaction of UHE neutrinos with massive relic neutrinos to produce the Z boson, from which the UHE protons via hadronic mode decays could be created. The UHE neutrinos would not be attenuated even on cosmological distances. Neutrino mass estimates from measurements of the UHE cosmic ray spectrum⁴ can be compared with laboratory measurements of KATRIN and test the Z-burst hypothesis.

Last but not least neutrino mass result from KATRIN could contribute to understanding of a future supernova neutrino signal to be detected in existing experiments. In particular, a better understanding of star core neutronization process and emission of gravitational waves could be achieved [27].

1.4. Important historical milestones

Since Pauli's proposal of neutrino existence experiments were dedicated to directly detect the particle and confirm his idea. The first evidence came from experiment with electron capture (EC) on ^{37}Ar [28]. A delayed coincidence measurement was applied, started by Auger electrons emitted after EC and stopped by detecting the recoil nucleus. Indeed, a signal was found corresponding with time of flight of the nucleus (which depends on known energy released during the decay).

Final confirmation came from C. Cowan and F. Reines [1]. They detected nuclear reactor neutrinos via the reaction

$$\bar{\nu}_e + p \rightarrow e^+ + n. \quad (15)$$

The measurement was based on coincidence measurement of 511 keV photons emitted after positron annihilation and of photons emitted after neutron capture in ^{113}Cd a few μs later. Positive signal from this measurement was interpreted as a signal for detection of the reaction (15) and thereby observing the particle.

Since then, various experiments were in search for finite neutrino mass utilizing the shape of energy spectrum of β -electrons in the endpoint region and tritium as a suitable source. However, until now all experiments reported negative m_ν^2 values, clearly indicating presence of unrecognized systematic errors [29, 30, 31, 32, 33, 34]. The last and so far most accurate results from Mainz and Troitsk neutrino mass experiments are compatible with each other with upper limits on m_ν of $2.05 \text{ eV}/c^2$ (95 % C.L.) for

³ The adjective "hot" refers to matter composed of relativistic particles when decoupling from matter, whereas "cold" refers to non-relativistic particles.

⁴ In progress in the Pierre Auger Observatory experiment [26].

Troitsk [35] and 2.3 eV (95 % C.L.) for Mainz [36]. Such a sensitivity resulted from careful analysis of the systematic effects and the use of the MAC-E filter spectrometer, which is described in more detail later.

These results are still compatible with zero neutrino mass and do not determine whether a non-vanishing mass exists. The confirmation of non-zero mass came from neutrino oscillations experiments. The Super-Kamiokande experiment [5], a giant water Cherenkov detector, investigated the so-called atmospheric neutrinos. These are produced in decays of muons and mesons, which are created by interactions of cosmic rays within the Earth's atmosphere. The neutrinos were detected via the reaction (14) as the created lepton (electron or muon) radiated the Cherenkov light which was collected by photomultipliers. It was clearly shown that a deficit in upward going muon-like events exists in the data which means less than the expected number of neutrinos in a no-oscillation scenario was observed. These results were further supported by results of the accelerator oscillation experiment K2K [9].

Regarding solar neutrinos, which come to Earth from fusion reactions taking place inside the Sun, the first experiment was done by R. David Jr. [37] indicating a deficit in observed number of neutrino reactions than expected from the solar model, known as the solar neutrino problem. After clear confirmation of this deficit the solution came from the Sudbury neutrino observatory (SNO) experiment [7]. Utilization of heavy water, which has deuterium built in instead of normal hydrogen, enabled one to observe also neutral current interactions of neutrinos of the type



which are independent of the participating neutrino flavour and thus any oscillations. The observed number of these reactions completely agreed with prediction of the solar model, while the number of charged current reactions of electron neutrinos showed a deficit from the expected one. This clearly indicated the neutrinos oscillation scenario and thus non-vanishing neutrino mass. Such results were then supported also by the reactor neutrinos experiment KamLAND [8].

1.5. KATRIN experiment

The KATRIN experiment is designed to measure the electron antineutrino mass from the tritium β -spectrum at the endpoint region with a sensitivity of 0.2 eV/ c^2 at 90 % C.L. [12]. This is an improvement by a factor of 10 over the sensitivity of the most recent experiments in Mainz and Troitsk. Experience from these experiments with the measurement itself as well as with systematic issues handling is utilized. Moreover, one magnitude larger analyzing system is designed in order to obtain enough luminosity. The outstanding instrumental resolution of 0.93 eV is planned to be achieved as well. The experiment is being built on the side of the Tritium Laboratory Karlsruhe which will provide the necessary infrastructure for tritium handling.

The design setup, shown in Fig. 2, corresponds to an approximately 70 m long linear configuration with about 40 superconducting solenoids, which will guide the β -electrons from the source to the detector. Detailed information about individual components can be found in [12]. The main parts of the design of KATRIN, as shown in the figure, are:

- Windowless gaseous tritium source (WGTS) as the primary high-luminous source for β -electrons.
- Differential pumping section (DPS) and cryogenic pumping section (CPS) serving for both tritium flow reduction and as electron transport systems.

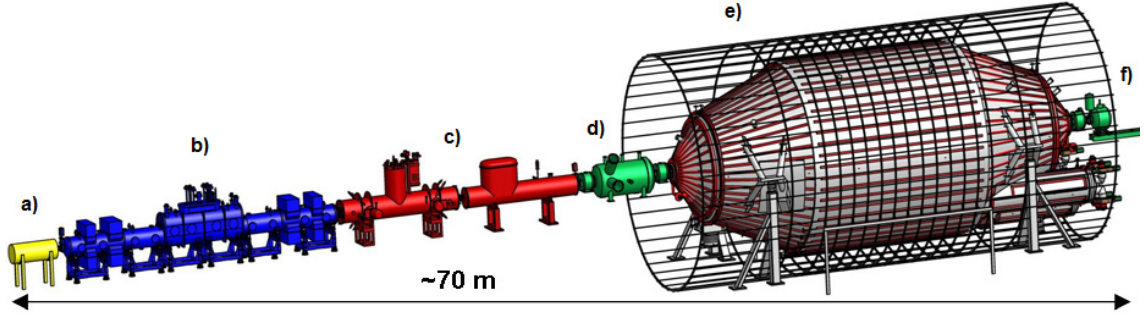


Fig. 2. The KATRIN design setup with the primary components: *a*) electron gun, *b*) windowless gaseous tritium source (WGTS), *c*) transport and pumping sections (DPS and CPS), *d*) pre-spectrometer, *e*) main spectrometer, *f*) semiconductor multi-pixel detector.

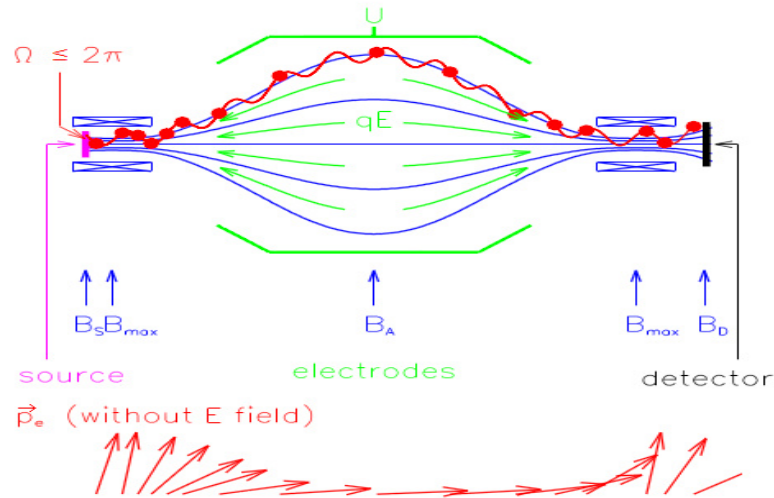


Fig. 3. Principle of the MAC-E filter. The upper part shows the trajectory (in red) of an electron along a magnetic field line emitted from the source on the left side going towards the detector on the right side. The bottom part shows the momentum vector of such electron along the path.

- Two MAC-E filter type spectrometers. The first and smaller one, known as the pre-spectrometer, acts as a pre-filter of electrons with small energy and thus lets through only the electrons from the endpoint region. The second, much larger one, is the main spectrometer and its purpose is to analyze the energy of the electrons with the resolution of 0.93 eV.
- Multi-pixel semiconductor detector for counting of electrons.
- Electron gun part placed before the WGTS serving as a tool for check of tritium gas and spectrometer properties.
- Separate independent 5 m long beam line with another MAC-E filter (not shown in figure) serving as the monitor spectrometer (described further).

1.5.1. The MAC-E filter

The MAC-E filter (Magnetic Adiabatic Collimation combined with Electrostatic filter) [38, 39, 40, 41] is an electrostatic retarding spectrometer which offers both high luminosity and high energy resolution. These two properties are the necessary prerequisites for measuring of the tritium β -spectrum endpoint region. Its main principle is illustrated in Fig. 3. Two superconducting solenoids are placed at both ends and produce a magnetic guiding field with its maximum B_{max} . An electron is emitted from the source on the left side into the right hemisphere (solid angle $\Omega = 2\pi$ for the

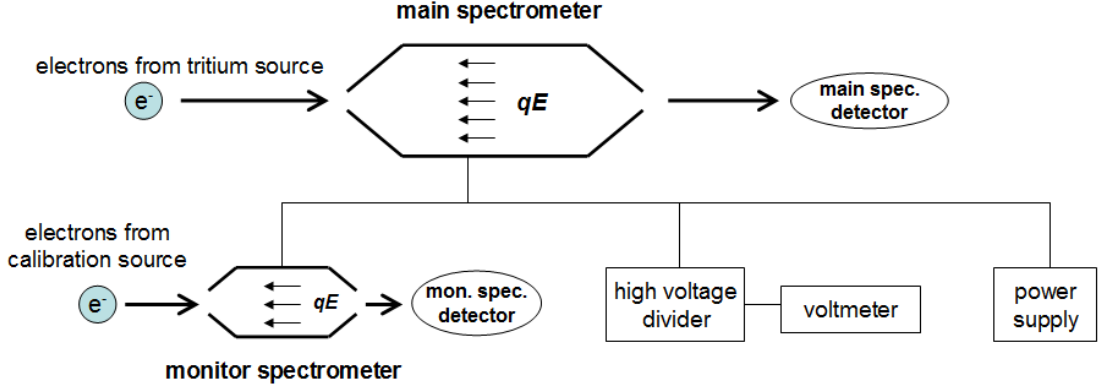


Fig. 4. The KATRIN monitoring concept. The high voltage applied to the main spectrometer, which analyses the β -electrons, is reduced by a high voltage divider and measured by a precision voltmeter. The same high voltage is applied to the monitor spectrometer, which measures conversion electrons from a stable calibration source.

source situated at maximal magnetic field B_{max}). On its way it is guided by a cyclotron motion along the magnetic field lines into the volume of the spectrometer.

Due to slowly varying magnetic field the momentum of the electron transforms adiabatically keeping its magnetic moment constant. This results in transforming of most of the electron cyclotron energy into longitudinal motion as indicated in the figure by the momentum vector \vec{p}_e . As the electron gets into the so-called analysing plane in the middle (where magnetic field is at its minimal value B_A) it runs into an electrostatic field E created by cylindrical electrodes on which the voltage U is applied. If it has enough energy it will pass through the potential barrier, get reaccelerated and detected by the detector (which is situated at position with magnetic field B_D). If not it will be reflected and will not reach the detector. This means that all electrons having their energy equal or larger to qU , where q is the charge of the electron, will be detected. Thus, applying stepped voltage to the retarding electrodes enables one to analyse the electron energy in an integrating mode.

Usually, the source is placed in slightly lower field B_S resulting in lowering the acceptance angle from 2π . This is to avoid extra long electron path in the source with finite thickness which would increase the chance of the electron being inelastically scattered.

1.5.2. Monitoring of the KATRIN experiment

In order to measure the electron energy one must know precisely the retarding voltage being applied as it is clear from the description of the MAC-E filter principle. Together with that also stability during each step of the retarding voltage is needed. When reaching for sensitivity of $0.2 \text{ eV}/c^2$ for the neutrino mass the requirements for high voltage monitoring are demanding. Explicitly, it has been shown that a long-term precision of 3 ppm is crucial [12]. As the endpoint energy of tritium is around 18.6 keV this means $\pm 60 \text{ mV}$ for the absolute precision.

Important check of the long-term stability issues and also a check for systematic errors will be provided by means of direct absolute calibration of the main spectrometer. This will be done with either a photoelectron or a conversion electron source with well-defined energy and narrow line shape. This method can not be applied online (during tritium runs) and has to be done in regular intervals between the measurements.

In order to achieve the desired precision in online monitoring of the retarding high voltage two independent methods will be applied:

- Direct measurement of the high voltage. Low voltages up to 20 V are ideally suited for state of the art measurements. Therefore, the high voltage applied to the retarding electrode will be firstly reduced by a high voltage divider, see Fig. 4, with very stable dividing ratio to the range ≤ 20 V. This divider was developed inside the KATRIN Collaboration in cooperation with PTB Braunschweig.
- Utilization of another MAC-E filter (monitor spectrometer concept). The former spectrometer from the Mainz experiment will be plugged to the same high voltage as the main spectrometer, see Fig. 4. A conversion electron source will be inserted into the monitor spectrometer and a sharp and energetically well-known conversion electron line will be measured by varying the voltage applied to the source. Any change of the line position could indicate an instability of the high voltage determined by the divider-voltmeter setup. This will allow practically continuous monitoring of the high voltage of the main spectrometer. Therefore, this represents an important tool for KATRIN and a powerful alternative to the first method.

It is clear that proper functioning of the monitor spectrometer concept requires a source with long-term stable conversion electron line, ideally with energy close to the endpoint of the tritium β -spectrum. The isomeric state ^{83m}Kr with half-life of 1.8 hours provides conversion electrons with energy of only 800 eV below the tritium endpoint [13] with a narrow line width of 2.7 eV. It is thus suitable for KATRIN needs. Due to its short half-life it is replenished by decay from ^{83}Rb with half-life of 86.2 days [13]. Following, ^{83}Rb sources are in the center of attention for possible use in monitoring of KATRIN. Some properties of solid ^{83}Rb sources were investigated and are reported in this thesis in subsequent chapters.

2. Solid $^{83}\text{Rb}/^{83\text{m}}\text{Kr}$ sources

The conversion electrons emitted from the isomeric state $^{83\text{m}}\text{Kr}$ can have various discrete energies depending on which subshell the electron was emitted from. The most important conversion electron line for KATRIN is the K-32 line, which corresponds to electrons emitted from the K shell due to the conversion of the 32 keV nuclear transition in $^{83\text{m}}\text{Kr}$, see Fig. 5. It has energy of 17824.3(5) eV and line width of 2.70(6) eV [42]. The 32 keV transition is also highly converted, the total conversion coefficient amounts to $\alpha_{32} = 2010$. The line energy, its reasonable width and high conversion coefficient make it suitable for KATRIN needs, as the difference of the line energy and the tritium endpoint is only about 800 eV.

The half-life of $^{83\text{m}}\text{Kr}$ is only 1.83(2) hours. Thus, with such a short half-life one avoids any long-term contamination of the electron spectrometer. On the other hand, replenishment of $^{83\text{m}}\text{Kr}$ is necessary for any measurement lasting more than several hours. The replenishment can be done by means of the isotope ^{83}Rb with long enough half-life of 86.2(1) days which decays by pure electron capture to the isomeric state $^{83\text{m}}\text{Kr}$, see Fig. 5. The method is to capture $^{83\text{m}}\text{Kr}$ within the ^{83}Rb sample until its decay. The mother isotope is either vacuum evaporated on or implanted in a suitable substrate and is captured there. In this way a solid $^{83}\text{Rb}/^{83\text{m}}\text{Kr}$ source is made. As the dimensions of the substrate are usually a few mm such source is also very easy to handle.

2.1. ^{83}Rb production method

The production of ^{83}Rb isotope is done at the U-120M cyclotron at Nuclear Physics Institute in Řež with a proton beam. The reaction is $^{nat}\text{Kr}(p, xn)^{83}\text{Rb}$ with use of a water cooled krypton target. Its design and construction were reported in [43]. Pressurized krypton gas with absolute pressure of 7.5 bar at room temperature in volume of 22 cm³ is exposed to external 6 μA proton beam for 12 hours which results in total beam charge of 250 mC. Primary energy of the proton beam is 27 MeV. Due to energy degradation in the cyclotron output aluminium window, the target titanium input window and the krypton gas itself a beam of about 19.5 - 24.1 MeV arrives at the gas. This range is optimal for ^{83}Rb production rate and minimizing amount of ^{84}Rb .

The irradiated target is left for a week to let short lived activities to decay. After that

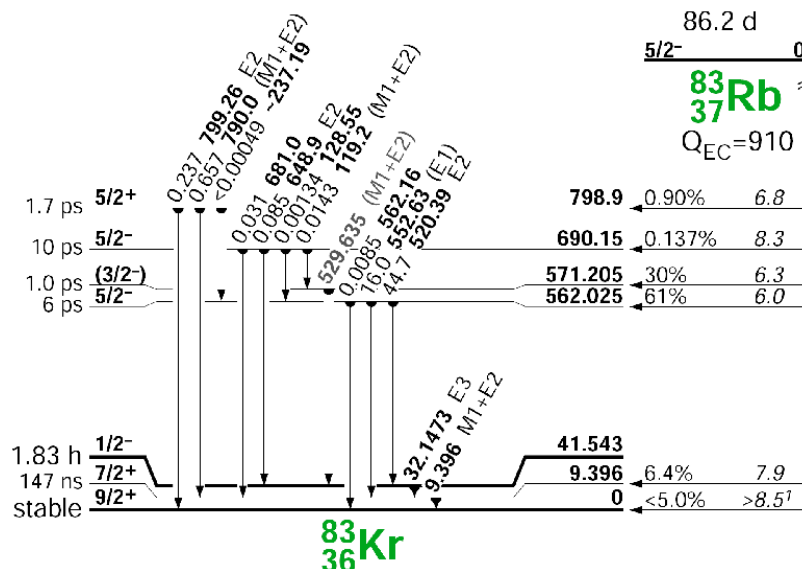


Fig. 5. ^{83}Rb decay scheme and $^{83\text{m}}\text{Kr}$ energy levels [44]. The isomeric state $^{83\text{m}}\text{Kr}$ corresponds to the excited level with energy of 41.543 keV and half-life of 1.83 hours.

the mixture of rubidium isotopes deposited on the target walls is two times washed out by about 25 cm³ of distilled water. Complete activity of ⁸³Rb in water solution is about 100 MBq [45].

2.2. Vacuum evaporation method

Vacuum evaporation of ⁸³Rb atoms is done by means of the modular high vacuum coating system MED 020 from BAL-TEC. It is equipped with an oil-free vacuum system which enables one to achieve the pressure of about 3·10⁻⁶ mbar. The rubidium water solution is put into the tantalum boat and let to evaporate using infra lamp. Then the boat is installed into MED 020 and pre-heated to 200 °C for 5 - 10 minutes to avoid possible impurities. Evaporation of ⁸³Rb is done at about 800 °C for 30 - 60 seconds through a mask with diameter of 8 mm.

Various sources were produced by this method and a report about them can be found in [42]. The source studied in this thesis is denoted S28 and was produced in 7 / 2008 on a 0.2 mm thick carbon foil. The rubidium solution activity in the boat was about 18 MBq. Its activity to the reference date of 20 November 2009 was measured to be 0.101(4) MBq. The activity measurement was done by means of a HPGe detector by measuring the area of the 520 keV γ -line in ⁸³Rb decay, see Fig. 5. The intensity value (available from the decay scheme) and the detector efficiency for detecting the 520 keV radiation at a particular geometry setup allowed us to establish the activity of the source with enough precision.

2.3. Implantation method

Implantation of ⁸³Rb atoms is done at the On-line Isotope Mass Separator ISOLDE at CERN. Radioactive nuclides are produced by interaction of a 1.4 GeV proton beam with a uranium carbide - tantalum (UC_x-Ta) target and are extracted as an ion beam with 30 keV of energy. The General Purpose Separator is then used for extraction of high purity ⁸³Rb beam. Typically, the system is able to deliver the activity of 1 MBq per hour. A system of retardation electrodes can be used for access to lower implantation energies. The atoms are implanted into a substrate with diameter of 12 mm, which is held at room temperature, inside a vacuum chamber with pressure of about 10⁻⁵ mbar.

In this way four solid implanted sources, which are studied in this thesis, were produced. Tab. 1 gives the materials from which the substrates are made, the implantation energies and purities of the substrates. Also given is the month of production of the sources and their measured activities for particular reference date. Denomination of the sources is done by the system: "substrate - implantation energy", e.g. Pt-30, see the table. The activities of the sources were measured in similar way as the activity of the source S28.

Source	Substrate	Purity [%]	Implantation energy [keV]	Month of production	Activity [MBq]
Pt-30 #1	platinum	99.7*	30	11 / 2008	0.16(1)
Pt-30 #2	platinum	99.99**	30	6 / 2009	1.35(5)
Au-30	gold	99.99**	30	6 / 2009	0.91(4)
Pt-15	platinum	99.99**	15	6 / 2009	0.54(2)

Tab. 1. Properties of the solid implanted sources produced at ISOLDE. Reference date for the measured activities is 20 November 2009. * 40 μ m thick foil with 0.3 % of rhodium impurity was used. ** A foil from the Goodfellow company with thickness of 25 μ m was used.

3. Precise energy of 9.4 keV γ -ray transition in $^{83\text{m}}\text{Kr}$

For the precise monitoring of the KATRIN experiment, as described in more detail in the previous chapter, a stable conversion electron source $^{83}\text{Rb}/^{83\text{m}}\text{Kr}$ will be utilized. In general, for $^{83\text{m}}\text{Kr}$ atoms in gaseous form the kinetic energy of a conversion electron E_{kin} is given by [12]

$$E_{kin} = E_{\gamma} - E_{bin}^{vac} + E_{\gamma,rec} - E_{e,rec} - (\phi_{spectr} - \phi_{source}), \quad (17)$$

where E_{γ} is the energy of the corresponding γ -ray transition, E_{bin}^{vac} is the binding energy of the electron, $E_{\gamma,rec}$ is the energy of the recoil atom after γ -ray emission, $E_{e,rec}$ is the energy of the recoil atom after emission of the conversion electron, ϕ_{spectr} is the work function of the spectrometer and ϕ_{source} is the work function of the source. In order to check the properties of both the source and spectrometer parts in KATRIN as well as to do an absolute energy calibration one has to know precisely the individual terms in eq. (17).

Specifically, regarding the γ -ray energy E_{γ} the convenient option is to measure it precisely with γ -spectroscopy method. In $^{83\text{m}}\text{Kr}$ there are two possibilities for a γ -ray transition, namely the 32 keV transition and the 9.4 keV transition, see the decay scheme in Fig. 5. The first transition is the most important as the corresponding K shell conversion electron line K-32 has energy of about 800 eV below the tritium endpoint energy. The 32 keV transition energy was measured using γ -spectroscopy with enough precision earlier [46].

The 9.4 keV transition energy was already measured by means of γ -spectroscopy, but with a precision of about 10 eV [47, 48, 74], which is completely inadequate for KATRIN needs. Other results for this energy come from conversion electron spectroscopy [49, 50] and the most accurate ones [51, 52] were obtained by using theoretically corrected binding energies. The list of available 9.4 keV transition energies is given in Tab. 2.

The available results imply the need for precise determination of the transition energy using γ -spectroscopy and simultaneously confirmation of more precise electron spectroscopy results with an independent method. It is the purpose of this chapter to report on measurement, which was done by means of γ -spectroscopy. In subsequent sections the 9.4 keV line will always be referred to as $\gamma_{9.4}$ and its energy as $E_{9.4}$. This work is an improvement over the analysis which was reported in the bachelor thesis of the author [53].

Year	Value [eV]	Type of meas.	Ref.
1971	9400(20)	γ -spectroscopy	47
1972	9400(10)	conversion e^{-} spectr.	49
1972	9400(30)	γ -spectroscopy	48
1976	9390(10)	γ -spectroscopy	74
1992	9405.9(8)	conversion e^{-} spectr.	51
1993	9396(3)	conversion e^{-} spectr.	50
2008	9404.71(35)	conversion e^{-} spectr.	52

Tab. 2. Published energy values of the 9.4 keV γ -ray transition in $^{83\text{m}}\text{Kr}$. The values in brackets indicate one standard deviation for the last digits.

Firstly, the experimental approach to the problem of $E_{9,4}$ determination is explained and the measurement apparatus and setup are described. Then, systematic effects which may influence the data analysis are addressed. Next, description of lines in γ -detector energy spectra is given. After that background lines in the spectra are discussed. Finally, the results of the measurement are given and discussed with regard to the existing values of $E_{9,4}$. Also given are the results of measurement of Ga $K\alpha_1$ line energy, which was done in order to verify the approach for energy determination.

3.1. Experimental method

The determination of precise energy $E_{9,4}$ using semiconductor γ -spectroscopy relies on precise energy calibration of the γ -detector. For that the energies of calibration lines have to be known to a high degree of accuracy. A number of two calibration lines is sufficient. The ideal situation is established when the observed $\gamma_{9,4}$ line is energetically situated between energies of the two calibration lines, the region spanned by them is reasonable in size and all lines can be observed at once in one spectrum. Then the energy $E_{9,4}$ can be determined using linear interpolation, i.e. it is obtained from the linear channel-to-energy relation. This technique, which rests upon linearity of the spectrometric chain, is successfully used and well described [54, 55].

In case of $E_{9,4}$ its determination represents a unique process because in this energy region no suitable γ -rays for the calibration exist. Therefore, characteristic x-ray lines have to be used instead. As these x-rays correspond uniquely to specific elements, this gives one an ability to choose the right calibration lines by choosing the appropriate elements. The $^{83}\text{Rb}/^{83\text{m}}\text{Kr}$ source also provides an advantage as strong K_α and K_β x-ray lines observed in the decay cause fluorescence in nearby material. This means if the elements are intentionally embedded near the source one is able to detect all the lines simultaneously.

After careful consideration the $K\alpha_1$ lines⁵ of nickel (Ni) and arsenic (As) were chosen as the energy calibration lines. Energies of these lines are known to a precision of better than 1 ppm [56] from diffraction spectroscopy measurements. Pieces of these elements can also be obtained in high element purity form, i.e. 99.999 %, which minimizes the risk of presence of parasitic KX lines from other elements in the spectra. By inserting appropriate amount of Ni foil and As powder together with the $^{83}\text{Rb}/^{83\text{m}}\text{Kr}$ source for detection by the γ -spectrometer one is able to achieve similar intensity on the corresponding calibration lines and $\gamma_{9,4}$. Such calibration spectra are then analysed using PC (personal computer) software and the positions of the lines in channels are determined.

3.2. Measurement apparatus and setup

In the measurements a commercial apparatus was used. It consists of a silicon lithium detector of $80 \text{ mm}^2 \times 5 \text{ mm}$ with built-in preamplifier and spectroscopy amplifier, models SL80175 and 2026 from the Canberra company. The detector is equipped with beryllium window with thickness of 0.05 mm. The resolution of the detector amounts to 220 eV at energy of 7.5 keV (Ni K_α). Computer-based ADC (analogue to digital converter) card TRUMP from the EG&G Ortec company digitizes the amplifier output signals into 8192 channels which can be seen in PC software as a

⁵ The component $K\alpha_1$ ($K\alpha_2$) is emitted when an electron drops from the L_3 (L_2) subshell to a vacancy on the K shell. The transition from L_1 to K is forbidden due to conservation of angular momentum and is not considered further.



Fig. 6. The Canberra Si(Li) γ -spectrometry apparatus.

spectrum, i.e. counts per channels. In Fig. 6 a photograph of the γ -spectrometry apparatus is shown.

The geometry used throughout the measurements is based on one general setup, see scheme in Fig. 7. The detector is highlighted by grey filling. It is closed in cylindrical stainless steel endcup with the beryllium window. Pure aluminium construction, which is hatched in the figure, supports aluminium collimator and plastic interchangeable cylinder with a lid. The cylinder with a suitable height G allows to establish the desired distance of the radioactive source to the detector. The value $coll$ denotes the inner diameter of the collimator construction and was fixed to 6 mm. The radioactive source together with the Ni and As pieces are situated on top of the lid in the 24 mm diameter hollow.

Regarding the radioactive source the parent generator ^{83}Rb was produced at U-120M cyclotron of the Nuclear Physics Institute (NPI) in Řež and after simple laboratory procedure obtained in the form of rubidium water solution. The production process is described in detail in the previous chapter. The radioactive source for the measurement was made in a way that part of the solution was deposited on a polyethylene (PET) foil, dried and sealed with another PET foil. A few MBq of activity was obtained.

The γ -detector energy spectra analysis was done by means of the data analysis framework ROOT [57], which provides libraries for numerical fitting of spectra. Namely, the Simplex and the Migrad routines from the Minuit library were utilized. The fit is based on minimizing the chi-square function over the space of free variables, such as peak amplitude, centroid and width (and more). If the fit converges the parameter values together with estimates of their errors are returned. Goodness of the fit is characterized by the chi-square value at the minimum divided by the number of degrees of freedom in the fit, the so-called reduced chi-square χ_{red}^2 . For fit quality check also visual inspection of the so-called normalized residual plot is done. The normalized residuals are differences of numerical and calculated values divided by errors of the numerical values (which are just square roots of the numerical values).

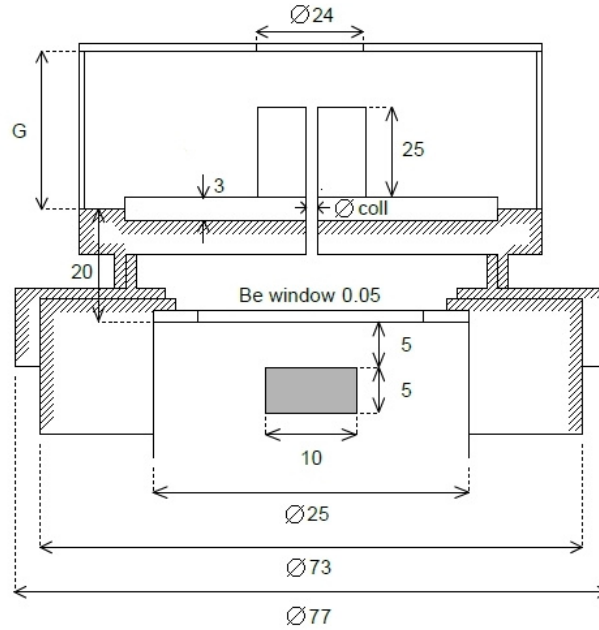


Fig. 7. Sketch of the experimental source-detector geometry. The dimensions are given in mm. For further description see the text.

3.3. Systematic effects

The line $\gamma_{9.4}$ originates in the atomic nucleus, whereas the characteristic x-ray lines originate in the atomic shell. This difference can be a source of systematic errors. Specifically, fine atomic shell processes such as emission of additional weak lines, which accompanies the characteristic x-ray emission, can not take place inside the nucleus and thus can not be seen accompanying the γ -line. Their presence in γ -detector energy spectra may, however, influence the determination of position of the characteristic x-rays.

In this section two fine atomic shell features, namely the satellite lines and the radiative Auger effect, are described in detail. Both effects result in emission of weak x-rays which are energetically close to the characteristic x-rays. The properties of the weak x-rays such as energy, intensity and width are examined in order to include them in spectra analysis. The respective inclusion is described in the section *Description of lines*.

3.3.1. Satellite lines

In the atomic shell when an electron de-excites from a higher atomic subshell to a lower vacant subshell the excess energy can be emitted in the form of a characteristic x-ray. Its energy is given by difference of the electron binding energies on the individual subshells. Therefore, the x-ray uniquely corresponds to the electron transition and the atom involved and is called a diagram line. However, the same energy of the x-ray can only be observed for single-ionized atoms, i.e. atoms with one electron vacancy. If the atom is multiply ionized the energy is slightly shifted towards higher energies [58, 59]. This shift results from a small change of effective screening potential of the remaining electrons. Specifically, the potential gets weaker as there are less electrons present in the atomic shell. These x-rays are weak in

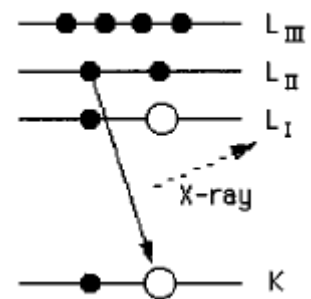


Fig. 8. X-ray satellite line emission.

intensity compared to the diagram lines and are called the satellite lines. The process is illustrated in Fig. 8.

The shifts in energy of the satellite lines are at the order of tens of eV and the intensities relatively to the diagram lines vary from almost zero to a few per mille [58, 59]. Such lines are thus indistinguishable from the diagram lines with a standard Si(Li) detector with a resolution of about 200 eV. Nevertheless, in spectra analysis their presence may influence the determination of a diagram line position and represent an unaccounted systematic error if not taken into consideration properly.

In our situation the characteristic x-rays are induced by incident radiation from the $^{83}\text{Rb}/^{83\text{m}}\text{Kr}$ source. For the source activities of a few MBq the probability of double ionizing an atom with two different photons during the lifetime of an electron vacancy of the orders of 10^{-15} s is negligibly small. Thus multiple ionization can only be caused by a single incident event. This is only possible if the incoming radiation has enough energy to eject both K and L or K and M shell electron together. Then, in dependence on which electron has been ejected, a specific satellite line can be emitted.

For Ni, Ga and As the highest electron binding energies are for the K shell and the L_1 subshell. Taking a sum of them we get roughly 9.3 keV for Ni, 11.7 keV for Ga and 13.4 keV for As[60]. Most photons emitted from the radioactive source have energies of 12.6 keV ($K\alpha$) and 14.1 keV ($K\beta$) [56]. From this we see that the radiation is indeed capable of multiply ionizing the Ni, Ga and As atoms. For the last one, however, only the less intensive $K\beta$ has such property. This means the intensity of the satellite lines will be somehow lower for As relatively to the diagram line. Nevertheless, the problem was approached as the intensity was full and from possible deviations from this value the systematic error for $E_{9,4}$ was determined (see further).

In order to investigate the intensities of the satellite lines in comparison to the diagram lines a dedicated study was made [61]. A diffraction spectrometer was used for detection of x-rays from Ti sample which was irradiated by x-rays from an x-ray tube. The dependence of the intensities on the tube voltage was observed. It was shown that for the voltage above about twice the excitation potential the intensities reached an upper bound and further remained constant. This means one can work with the upper

Ni	α_3	α_4	α_3'
Energy [eV]	7507.54	7512.10	7514.92
Intensity relative to $K_{\alpha 1}$ [%]	0.25	0.27	0.11
Line width [eV]	4.37	4.49	4.51
Ga	α_3	α_4	α_3'
Energy [eV]	9284.23	9290.02	9295.81
Intensity relative to $K_{\alpha 1}$ [%]	0.14	0.23	0.10
Line width [eV]	4.31	4.73	5.14
As	α_3	α_4	α_3'
Energy [eV]	10578.68	10584.57	10592.27
Intensity relative to $K_{\alpha 1}$ [%]	0.13	0.16	0.09
Line width [eV]	4.58	5.13	5.92

Tab. 3. Numerical values of properties of the satellite lines of Ni, Ga and As. The intensities were taken directly from papers [58, 59]. The energies and widths in eV were calculated from wave-length values in x units (xu) using the conversion coefficient in [56], p. 96, Tab. VI: $E \times \lambda = 12732.7227(40) \text{ eV} \times \text{xu}$ for Cu $K_{\alpha 1}$. In addition, the widths were corrected for finite resolving power of the diffraction spectrometer using eq. (1) in [58], p. 12 (as in the papers no correction was done).

intensities and determine the systematic error from errors of these intensities. The systematic error determination is described in more detail in the section *Determination of systematic error*.

The intensities of the satellite lines for Ni, Ga and As as well as their energies (wavelengths respectively) and widths were reported in the papers [58, 59]. These values are given in Tab. 3 for the three most intensive lines α_3 , α_4 and α_3' . Errors of the energies are for all lines 0.09 eV [58]. Errors of the widths were neglected. Errors of the relative intensities can be attributed to 3 % of the individual intensity values [59]. However, we know the intensities can in fact be lower (but not higher), especially for the case of As and it is extremely difficult to estimate to how much extent. Therefore it was decided to take single-way errors of the intensities as + 3% and -25 % of the values. The way of including the satellite lines into spectra analysis is described in the section *Description of lines*.

3.3.2. Radiative Auger effect

In the atomic shell the energy released during de-excitation of an electron is most often emitted via either a characteristic x-ray or an Auger electron, which is just a knocked-out atomic shell electron. However, there is a non-zero probability the photon and the Auger electron will be emitted at once, sharing the released energy. This process is called the radiative Auger effect (RAE) and is illustrated in Fig. 9. Specifically, it is illustrated when an electron from L_2 subshell fills the vacancy on the K shell. An x-ray together with an electron from the L_3 subshell are emitted. For this case the denomination $K-L_2L_3$ is used.

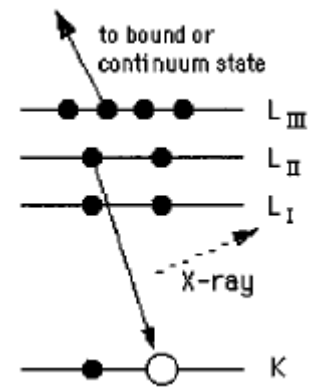


Fig. 9. The radiative Auger effect (here $K-L_2L_3$).

Presence of three objects in the final continuum state (electron shake-off effect) implies continuous energy of photons with upper bound corresponding to the situation when the emitted electron has zero kinetic energy. The energy spectrum is superimposed with discrete lines resulting from the situation when the final state electron is excited to a higher bound state (shake-up effect). Combination of shake-off and shake-up effects results in complicated structure of the photon energy spectrum.

The intensity of the RAE is low compared to the intensity of the diagram lines and the structures in the photon energy spectrum vary on the level of tens to a few hundreds of eV [62, 63, 64]. When observed with a Si(Li) detector such effects are completely smeared by the detector resolution and are not resolvable at all. As in the case of the satellite lines presence of the RAE may, nevertheless, influence the determination of the diagram line position in spectra analysis and also represent an unaccounted systematic error. The lines K-LM and K-MM are of main concern since they are situated energetically near the calibration lines and their intensity is large enough for them to be noticeable.

Intensity of RAE

There are numerous experimental values available for the intensities of K-LM and K-MM lines [62, 63, 64]. These values are shown graphically in Fig. 10 and Fig. 11. Together with that also theoretical calculations are available [65] and are shown in the figures as well. One can see in the low Z region an overall disagreement with the theory. Besides, for K-MM more experimental values exist for particular Z . The question now arises which intensities should be used in γ -detector energy spectra analysis.

Regarding K-MM there is exactly one experimental value for Ni ($Z = 28$) and As ($Z = 33$) and no value for Ga ($Z = 31$). As for K-LM there is also one value for As and no values for Ni and Ga. Thus, we can work with the measured values and interpolate the missing ones. Tab. 4 gives numerically such intensities. The interpolation was done by means of cubic splines available in ROOT. The multiple values were treated with an average of those values.

Regarding the uncertainties of the intensities it is known that for Kr ($Z = 36$) it amounts to 25 % [64]. With respect to differences between individual experimental multiple values and also between experimental and theoretical values it was decided to take 25 % as the error for all values in Tab. 4. From these errors the systematic error for $E_{9,4}$ was determined, see the section *Determination of systematic error*.

Shape of the RAE photon spectrum

According to [63] the highest intensity of the RAE peak is observed at the upper photon energy boundary and drops down to zero for lower photon energies. That is, however, the only specific information one is able to obtain about the general shape of the spectrum. Up to now there seems to be no theoretical prediction of the spectrum shape available [62]. Moreover, the spectrum shape details are unique for each element as apparent from the figures in the papers [62, 63]. Unfortunately, for Ni, Ga and As no graphs and also no numerical points, i.e. tabulated data for the RAE spectra, are available.

This forces one to adopt a phenomenological shape $R_{phen}(x)$, inspired by available data, roughly describing the general behavior of the photon spectrum. This shape is shown in Fig. 12. $R_{phen}(x)$ is a composition of three parts for boundaries $x_1 = 0$ and $x_2 = 25$ (in arbitrary units):

- for $x_1 \leq x \leq x_2$ a sum of the Lorentzian function $L(x)$ and linear function $P_1(x)$ with parameters A_L , Γ , k and q which are defined as

$$L(x) = A_L \frac{\Gamma^2/4}{(x-x_2)^2 + \Gamma^2/4}, P_1(x) = kx + q \quad (18)$$

- for $x \leq x_1$ only the function $L(x)$
- for $x \geq x_2$ the Gaussian function $G(x)$ with parameters A_G and σ defined as

$$G(x) = A_G \exp\left[-\frac{(x-x_2)^2}{2\sigma^2}\right]. \quad (19)$$

The individual parameters control the shapes and amplitudes of the corresponding functions and they are set in a way to reasonably model the general shape of the RAE peak. Numerical values of the parameters are given in Tab. 5. The functions used have no physical meaning, they were chosen purely for the peak shape construction. The Gaussian part ensures quick descent from maximum intensity to zero for increasing energies and the Lorentzian part combined with the linear function ensures slow descent for decreasing energies.

When considering use of the phenomenological shape in spectra analysis one has to recalculate the individual parameters in a way the resulting shape approximates real situation. This means one has to consider the energy (i.e. channel, see further) interval

for the RAE peak and its intensity in relation with the corresponding diagram line. The intensity is directly related to the area of the phenomenological shape. This area can be easily evaluated as all functions in eq. (18) and (19) are analytically integrable. When the integration of $R_{phen}(x)$ is performed (with respect to the definition scopes of the individual parts) the peak area A_{RAE} is given by

$$A_{RAE} = A_G \left(\sqrt{\frac{\pi}{2}} \sigma + \frac{5\pi}{12} \Gamma + \frac{1}{12} (x_2 - x_1) \right). \quad (20)$$

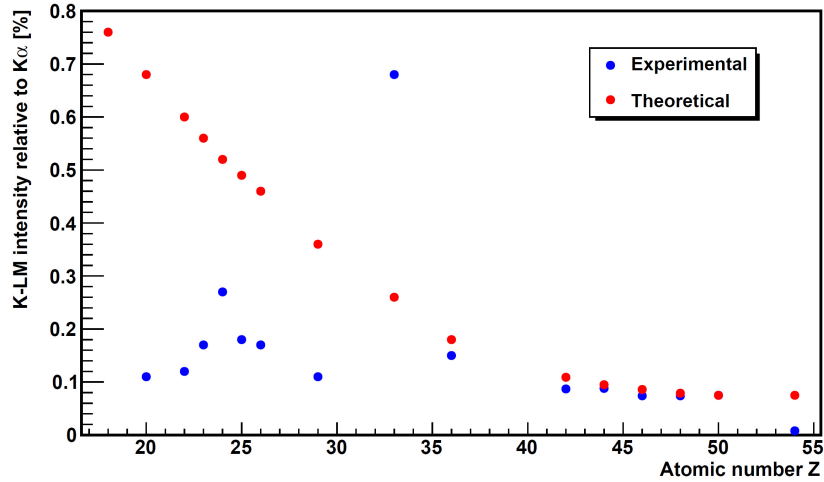


Fig. 10. Experimental and theoretical intensities of the K-LM radiative Auger effect. The experimental values were taken from [64], table V., and from [62]. The theoretical values were taken from [65].

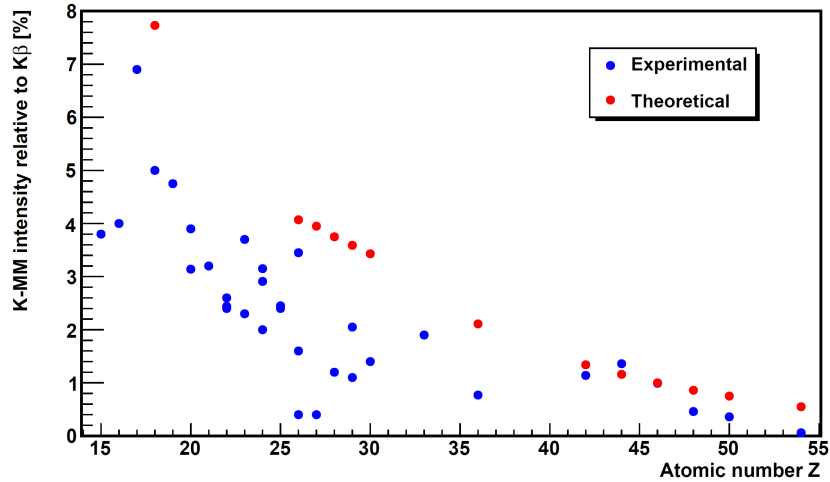


Fig. 11. Experimental and theoretical intensities of the K-MM radiative Auger effect. The experimental values were taken from [64], table VI. The theoretical values were taken from [65]. The points with more than one value indicate that more values for the particular Z are available.

	Ni	Ga	As
$I_{rel}(\text{K-LM})$ [%]	0.114*	0.31*	0.68
$I_{rel}(\text{K-MM})$ [%]	1.20	1.49*	1.90

Tab. 4. Intensities of the K-LM (K-MM) radiative Auger lines relatively to $K\alpha$ ($K\beta$) lines. The values with an asterisk were obtained by interpolation of available experimental data.

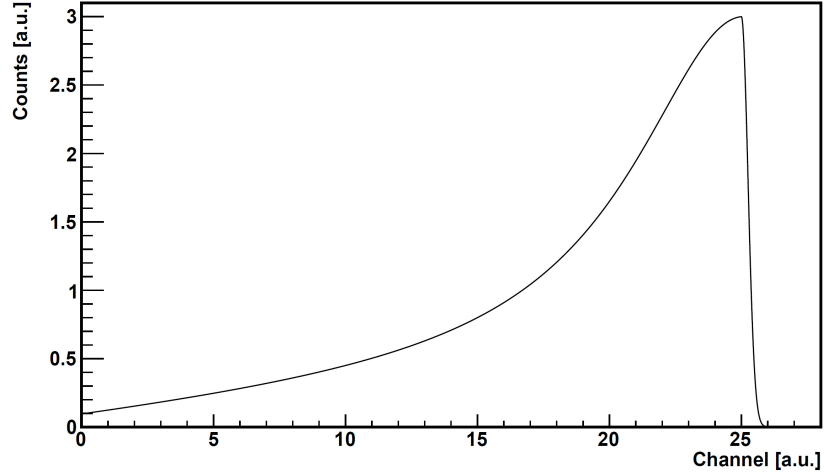


Fig. 12. The phenomenological shape $R_{phen}(x)$ of the radiative Auger effect photon energy spectrum.

Then, if the intensity of $K\alpha$ ($K\beta$) line is $I_{K\alpha}$ ($I_{K\beta}$) one can adjust the parameter A_G (the other parameters are set only by energy considerations, see further) so that it is satisfied

$$\frac{A_{RAE}}{I_{K\alpha}} = K \quad \text{or} \quad \frac{A_{RAE}}{I_{K\beta}} = K, \quad (21)$$

where K is the relative RAE peak intensity according to Tab. 4.

Concerning the energy scale one has to firstly determine the boundaries x_1 and x_2 . The upper boundary is given by the maximum photon energy as discussed previously. Thus x_2 is given by difference of the diagram line energy and the binding energy of the most weakly binded electron, i.e. the energetically highest Auger electron. A sort of uncertainty remains for the lower boundary because it is not precisely defined due to the fact the whole peak extends slowly to zero in intensity for decreasing energy. Nevertheless, in final the peak will be convoluted with the detector Gaussian response function and thus the lower boundary is not needed to be defined exactly. As an approximation it can be given by the energy of the energetically lowest Auger electron. Its energy can also be calculated by difference of the diagram line energy and the corresponding electron binding energy (the highest one). The lower and upper boundaries are given numerically in Tab. 6.

Having now the energy spread $x_2 - x_1$ the remaining parameters σ and Γ are calculated from direct proportion by the rule of three, i.e.

$$\sigma = \frac{x_2 - x_1}{x_{2o} - x_{1o}} \sigma_o \quad \text{and} \quad \Gamma = \frac{x_2 - x_1}{x_{2o} - x_{1o}} \Gamma_o, \quad (22)$$

where the index o indicates the values to be used from Tab. 5. This calculation then scales the shape of the RAE peak to the corresponding energy range. Description of the way of taking this phenomenological RAE peak into spectra analysis is given in section *Description of lines*.

Parameter	x_1	x_2	A_G	σ	A_L	Γ	k	q
Value	0	25	3	0.25	$\frac{5}{6} A_G$	20	$\frac{1}{6(x_2-x_1)} A_G$	$\frac{-x_1}{6(x_2-x_1)} A_G$

Tab. 5. Numerical values of the individual parameters used for constructing of the phenomenological shape of the RAE peak.

	K-LM		K-MM	
	x_1 [eV]	x_2 [eV]	x_1 [eV]	x_2 [eV]
Ni	7195.6	7399.4	8111.4	8156.0
Ga	8889.4	9223.4	10050.9	10329.5
As	10114.0	10489.2	11457.6	11620.6

Tab. 6. Lower and upper energy boundaries for the K-LM and K-MM radiative Auger peaks. The values were determined from the difference of the corresponding radiative transition energies [56] and the electron binding energies [60] as discussed in the text.

3.4. Description of lines

Determination of precise position of the x-ray and γ -ray peaks in the spectra is essential to this measurement. The lines have natural shape described by the Lorentzian function, see eq. (18) with $x_0 \equiv x_2$ as the peak centroid, with a specific line width Γ . This width is given by a sum of natural widths Γ_i , $i = 1, 2$, of the corresponding energy levels. The natural widths are related to the mean lifetime τ of vacancies of the corresponding energy levels via the so-called energy-time ‘‘uncertainty relation’’

$$\Gamma_i \cdot \tau_i \approx \frac{\hbar}{2}, i = 1, 2, \quad (23)$$

where \hbar is the reduced Planck constant⁶. The lifetime of the 9.4 keV level in ^{83m}Kr is about $1.5 \cdot 10^{-7}$ s [13] and corresponds to the natural width of about 10^{-9} eV which is completely negligible. However, the lifetime of inner electron levels is of the orders of 10^{-16} s corresponding to widths of a few eV [66] which should be taken into account.

The detector response function is modelled by the Gaussian function, see eq. (19). This means that the lines in spectra are described by the Voigt function $V(x)$ which is a convolution of the Gaussian and the Lorentzian function

$$V(x) = \int_{-\infty}^{+\infty} L(x') G(x-x') dx'. \quad (24)$$

The function is normalized in ROOT code (meaning the intergral of $V(x)$ over the whole real axis is one). In order to include the amplitude A , which describes the number of counts at the peak centroid x_0 , the peak is described as function $P(x)$ with the index *norm* indicating normalized Voigt function

$$P(x) = A \frac{V_{norm}(x)}{V_{norm}(x_0)}, \quad (25)$$

which gives exactly A for $x = x_0$.

The observed peaks are not ideal Voigt functions but also show asymmetric shape on the lower energy side. This asymmetry comes from incomplete charge collection in the detector, especially when the detector edges are hit by x-ray or γ -ray photons. The effect

⁶ Curent value of the reduced Planck constant is $6.582\ 118\ 99(16) \times 10^{-22}$ MeV·s [11].

was significantly reduced by introducing a 6 mm diameter aluminium collimator, see geometry sketch in Fig. 7, but it can not be removed completely and the asymmetry part of the peaks is needed to be taken into account.

The model for describing the asymmetry was taken from [67]. It is called the slope function $S(x)$ and is given by the expression

$$S(x) = \frac{1}{2} A_s \exp\left(\frac{x-x_0}{\beta}\right) \operatorname{erfc}\left(\frac{x-x_0}{\sqrt{2}\sigma} + \frac{\sigma}{\sqrt{2}\beta}\right), \quad (26)$$

where A_s is the amplitude of the slope function, β controls the width of the function, $\operatorname{erfc}(x)$ is the complementary error function and the other parameters have the same meaning as before. The complementary error function is defined as

$$\operatorname{erfc}(x) = \frac{2}{\sqrt{\pi}} \int_x^{+\infty} e^{-t^2} dt. \quad (27)$$

All peaks are superimposed on varying background $B(x)$. In suitable region it can well be described by maximally second order polynomial with appropriate parameters m , k and q

$$B(x) = mx^2 + kx + q. \quad (28)$$

Most often parameters corresponding up to only the linear term in eq. (28) are used.

As said before the characteristic $K\alpha_1$ x-ray lines are used for detector calibration. However, these lines are accompanied by the $K\alpha_2$ lines which are energetically very close and both lines are unresolvable from each other by the detector. Although both can be added to the fit and their parameters can be fitted separately, this leads to unphysical fit results, e.g. large energy spacing between the two. In order to preserve clear interpretation of the centroid position of the individual peaks the parameters of the $K\alpha_2$ were held fixed relatively to the parameters of $K\alpha_1$. This means the amplitude ratio of the lines was fixed, difference in position of the centroids was fixed and the difference in σ -widths was fixed. The Γ -widths were held fixed separately for both lines. Then the chi-square function is minimized only over some parameters of $K\alpha_1$ and the fit converges in a physical minimum.

The amplitude ratios and energy differences for Ni, Ga and As are known [44, 56] and are given numerically in Tab. 7. Changes in intensity ratios due to change in detector efficiency with energy can be neglected with regard to the errors of the ratios. In the fit the energy difference has to be included in units of channels and not in units of energy. The conversion, however, requires the channel-to-energy calibration relation to be known a priori. This can be overcome in the following way. A preliminary calibration of the detector is done by means of a simple fit, i.e. with single Gaussian lines only with no fixed parameters. Weighted averages of energies of $K\alpha_1$ and $K\alpha_2$ can be used as calibration values. Then the required energy difference in channels is calculated using the preliminary calibration and included in the full fit, i.e. with double constrained lines. An improved calibration is obtained and the energy difference is recalculated using the improved version. The fit is done again and the process is repeated until convergence of the parameter is achieved. This usually occurs after one or two full fits.

	$E(K\alpha_1)$ [eV]	$E(K\alpha_1) - E(K\alpha_2)$ [eV]	$I(K\alpha_2) / I(K\alpha_1)$	$\Gamma(K\alpha_1)$ [eV]	$\Gamma(K\alpha_2)$ [eV]
Ni	7478.2521(45)	17.2718(64)	0.508(34)	1.92	2.37
Ga	9251.674(66)	26.839(71)	0.510(28)	2.53	2.53
As	10543.2674(81)	35.77(15)	0.514(26)	3.03	3.04

Tab. 7. Energies of $K\alpha_1$ lines and numerical values for fixed parameters used in the fit. E denotes energy, I denotes intensity and Γ denotes natural width. The widths were derived from the recommended widths of electron atomic levels from [66].

The fixed difference in σ -widths was obtained in a similar way by doing a channel-to-width calibration. The values of the Γ -widths were derived from the recommended widths of electron atomic levels in [66] in a way that the width for $K\alpha_1$ ($K\alpha_2$) is the sum of the widths of K shell and the width of L_3 (L_2) subshell. Numerical values are given in Tab. 7. The values were converted to channels from eV in a similar way as the energy differences.

In slope function $S(E)$ another two free parameters appear, namely the amplitude A_S and the width β . It was found that fixing these parameters as well in the fit results in improvement of the fit quality among different spectra, i.e. the values $E_{9,4}$ obtained from various spectra tend to be significantly less scattered from each other. Determination of the two slope function parameters was done in two ways. Firstly, the parameters were obtained as weighted averages from fit of the line $\gamma_{9,4}$ (as there are no disturbances from the satellite lines or the RAE) measured without the Ni and As lines. Then these values were held fixed in fits of Ni, As and $\gamma_{9,4}$ lines in the calibration spectra with A_S relatively to amplitude of the corresponding line and β in absolute units. This procedure was used in phase I of $E_{9,4}$ determination (see section *Measurement results*).

Secondly, separate spectra with Ni or As calibration lines only were measured. This was done by slightly moving the radioactive source from the hollow of the lid but not moving the Ni and As pieces. With use of a tin collimator (with 6 mm in diameter) minimum radiation from the source could be detected, but the calibration x-rays were still well visible due to fluorescence. The slope function parameters were obtained from these spectra for Ni and As separately and then held fixed in fitting of calibration spectra. The slope function parameters for $\gamma_{9,4}$ were obtained from different separate spectra where only the radioactive source was placed above the detector. This procedure was used in phase II and III of $E_{9,4}$ determination.

Regarding the satellite lines they also have a natural shape described by the Lorentzian function. Therefore, in the spectra they were considered also as Voigt lines with fixed amplitudes relatively to $K\alpha_1$, fixed energy difference from energy of $K\alpha_1$ and fixed line widths, all known from Tab. 3 (in the table absolute energies of the satellite lines are given, the differences can be obtained with use of the energy calibration values $E(K\alpha_1)$ in Tab. 7). The σ -widths were held for simplicity the same as for $K\alpha_1$. This ensured the satellite lines to be binded to $K\alpha_1$ line in the same way as the $K\alpha_2$ line. For the satellite lines no slope function is added as due to their small intensity its contribution is negligible. Also the detector efficiency change with energy is again neglected.

Concerning the RAE peaks (K-LM and K-MM) a phenomenological shape $R_{phen}(x)$ approximates the real shape as discussed previously. Such a shape also has to be convoluted with the Gaussian detector response function. Calculating numerically the convolution each time a fit is done would significantly and unnecessarily increase computing time. It is thus worth to calculate the convolution in advance (with enough precision) and save the results as discrete numerical data. These data are then loaded

into the fit and the cubic spline interpolation available in ROOT is utilized to return values in between the discrete points. The numerical data are spaced in small steps to assure smooth interpolation.

The convolution calculation is done with respect to some fixed value of the $K\alpha_1$ line position x_{0c} , chosen usually to be close to the position seen in the spectra. This means the distance $x_{0c} - x_2$ is known (see the part *Radiative Auger effect*). Then in the fit the position of the RAE peak is taken with respect to the position of $K\alpha_1$ utilizing the value x_{0c} . If the convoluted RAE peak is described by a function $R_{conv}(x)$ (which is just the interpolation function mentioned)

$$R_{conv}(x) = \int_{-\infty}^{+\infty} G(x') R_{phen}(x - x') dx' \quad (29)$$

then in the fit it is included as $R(x)$

$$R(x) = R_{conv}(x - (x_0 - x_{0c})), \quad (30)$$

where x_0 indicates the centroid of $K\alpha_1$ which is being fitted. This ensures correct binding of the RAE peak to the $K\alpha_1$ line. Any transformation of parameters from energy scale to channels was done in the same way as other energy-like parameters.

The amplitude A_G of the RAE is taken equal to one in the convolution calculation. The RAE peak area is given by eq. (20) and its intensity by eq. (21). This means that in the fit A_G , now a free parameter, can also be fixed relatively to the amplitude of $K\alpha_1$ if this amplitude is related to the intensity of the $K\alpha_1$ line, which is just the area of the line. The area can be calculated because in ROOT the Voigt function representing the line is normalized. Therefore, with respect to eq. (21) and (25)

$$A_{RAE} = K \left(\frac{A_{K\alpha_1}}{V_{norm}(E_0(K\alpha_1))} + \frac{A_{K\alpha_2}}{V_{norm}(E_0(K\alpha_2))} \right). \quad (31)$$

However, including this into the fit increased computing time. If the area of the Voigt function is approximated by the area of the Gaussian function the RAE area is calculated as

$$A_{RAE} \approx K \sqrt{2\pi} (A_{K\alpha_1} \sigma_{K\alpha_1} + A_{K\alpha_2} \sigma_{K\alpha_2}). \quad (32)$$

The difference between areas for the RAE peak calculated by eq. (31) and (32) amounts to only about 1 %. Taking into account the errors of the RAE intensities are 25 % this can safely be neglected and the area can be calculated from the Gaussian function. For the K-MM peak its intensity is given relatively to the $K\beta$ lines. If such lines are not included in the fit the intensity is calculated relatively to the $K\alpha$ lines using relative intensities of $K\alpha$ and $K\beta$, given numerically in Tab. 8. These intensities need to be corrected for a small change of detector efficiency (about 1.35 %). Any efficiency dependence for the individual RAE peaks is neglected due to their large intensity uncertainties.

In the end the complete function describing the x-ray line in the γ -detector energy spectrum is a sum of

	$I(K\beta) / I(K\alpha)$
Ni	0.121(4)
Ga	0.125(4)
As	0.134(4)

Tab. 8. Intensities of the $K\beta$ series relatively to intensities of the $K\alpha$ series [44].

- two Voigt functions $P(x)$, eq. (25), for the $K\alpha_1$ and $K\alpha_2$ lines, the second one constrained to the $K\alpha_1$ line
- two constrained slope functions $S(x)$, eq. (26), one for each of the $K\alpha$ lines
- three Voigt functions $P(x)$ for the satellite lines constrained to the $K\alpha_1$ line
- two convoluted RAE peaks $R(x)$, eq. (30), for the K-LM and K-MM constrained to the $K\alpha_1$ line
- quadratic or linear background $B(x)$, eq. (28)
- other background lines $P(x)$ with small intensity in the spectra in close neighbourhood of the corresponding x-ray lines with their respective slope functions, can have $\Gamma = 0$ which reduces them to Gaussian lines

The line $\gamma_{9,4}$ is described without the satellite lines and the RAE peaks and with $\Gamma = 0$, which reduces it to a Gaussian line. If we now assume no background peaks in the calibration spectra the parameters being fit are

- amplitude of $K\alpha_1$ ($\gamma_{9,4}$)
- $K\alpha_1$ ($\gamma_{9,4}$) centroid position
- $K\alpha_1$ ($\gamma_{9,4}$) Gaussian width
- background coefficients

Each background line, with small intensity, would add three more parameters (amplitude, centroid position, Gaussian width) into the fit. The whole parameter fixing procedure reduced the number of free parameters in the fit to a necessary minimum. The fixed parameters were obtained from literature values and in the case of energy-like parameters the proper conversion to channels was done by means of fit iterations as already described in detail previously. In Fig. 13 an example of the full fit result and in Fig. 14 plot of the corresponding residuals are shown.

3.5. Spectra analysis

In Fig. 15 a typical calibration spectrum with Ni and As calibration lines is shown. In the figure both of these lines as well as the $\gamma_{9,4}$ have been marked. Together with that, also other lines, which are visible in the spectrum, have been marked. Namely, the $K\beta$ line series of Ni, the 9.7 keV background peak and the Si escape peak are visible. The last two will be discussed further.

As mentioned earlier the purity of the used Ni and As was for both 99.999 % meaning it is not possible to detect any impurities from these pieces with the detector. The radioactive source was checked for radionuclide purity on a HPGe (High Purity Germanium) γ -detector. Evidence for traces of usual byproducts during ^{83}Rb production such as other Rb isotopes was found. These isotopes should radiate no γ -rays in the region of interest. Small traces of Ni in the source were also found. These come most probably from the walls of the krypton target as they are nickel-plated. Finally, the PET foil, in which the radioactive source is placed, as well as the Si(Li) detector material were checked by means of x-ray fluorescence analysis (XFA) with a commercial ^{241}Am source for possible impurities. Negligible amounts of Cu and Zn were detected. A

slightly larger amount of Fe was also detected, but its x-rays are energetically not in the region of interest. No other lines expect for the usual x-rays from ^{241}Am were found during XFA.

Silicon escape peak, subtraction of an experimental “escape spectrum”

The Si escape peak appears in the calibration spectrum as a result of incomplete energy detection of strong $K\alpha$ x-rays emitted from the $^{83}\text{Rb}/^{83\text{m}}\text{Kr}$ source. If such an x-ray knocks out an electron from the innermost shell of Si a vacation on this shell is formed. It gets quickly filled by some outer electron and an x-ray is emitted. There is a small but non-zero probability that this x-ray will escape the detector without being

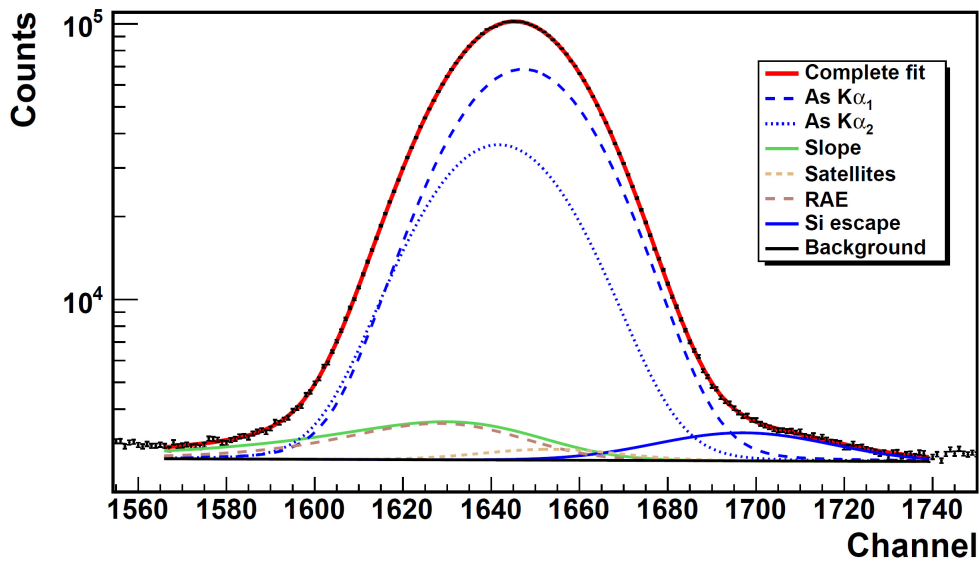


Fig. 13. Example of a complete fit on As $K\alpha_1$ and $K\alpha_2$ lines. Note the logarithmic scale on the vertical axis. The individual components are indicated in the legend. The complete fit is a sum of all these components. The Si escape peak comes from partial detection of strong Kr $K\alpha$ lines and is discussed further.

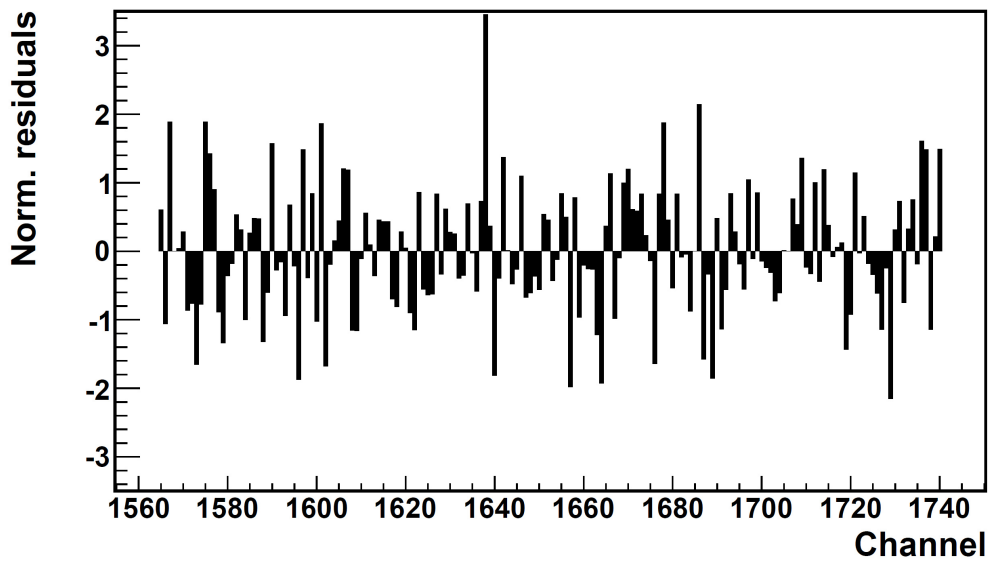


Fig. 14. The normalized residuals of the fit shown above in Fig. 13. The value χ_{red}^2 was 0.87, indicating good fit.

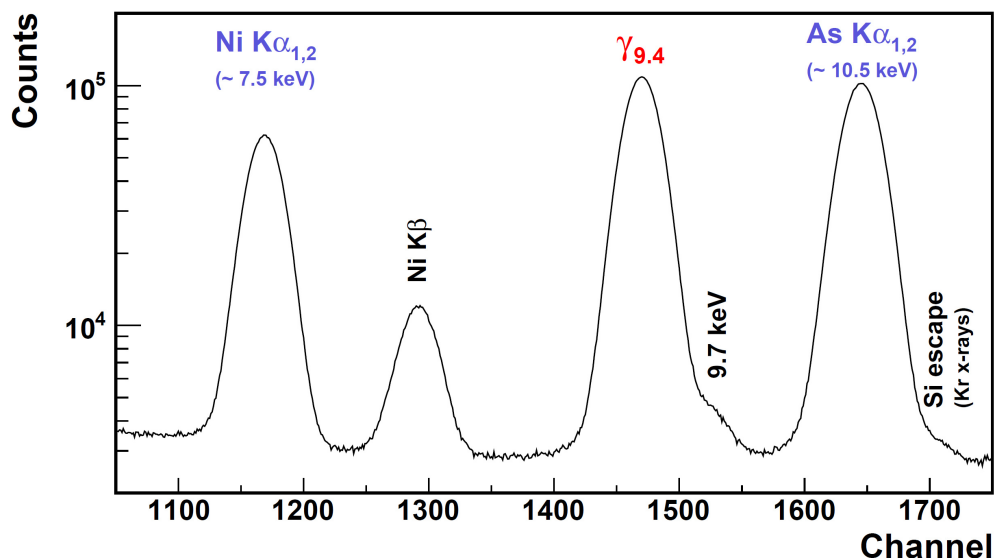


Fig. 15. A typical calibration spectrum with Ni and As calibration lines. Note the logarithmic scale on the vertical axis. The background peaks 9.7 keV and Si escape are discussed in the text.

absorbed. If this happens the energy detected will be lowered by the energy of the x-ray which escaped. In case of Si this energy amounts to roughly 1.8 keV [56]. Therefore, the energy of the Si escape peak of the Kr $K\alpha$ x-rays is about 10.8 keV and is visible on the high energy side of the As $K\alpha$ peak, see Fig. 15.

The fine structure of this escape peak is rather complex because there are more possibilities by which electron can fill the vacancy in Si, which results in different energy of the emitted x-ray. Also there are two energetically close x-rays from Kr, namely the $K\alpha_1$ and $K\alpha_2$. One way to handle this situation is to describe the Si escape peak purely with one Gaussian function with its own amplitude, centroid position and σ -width, neglecting the Γ -widths of the individual components. The result will be, in a good fit, a slightly larger σ -width than what would be expected based on calculation from the channel-to-width calibration.

The second way is as follows. A spectrum is experimentally acquired for which only the radioactive source is placed in the hollow of the lid and the Ni and As pieces are removed. Such a spectrum shall further be called “the escape spectrum”. If this spectrum is measured under similar conditions and for the same amount of time as the calibration spectrum it can be numerically subtracted from the calibration spectrum (i.e. the corresponding part of it) and as a result the Si escape peak will disappear but the As calibration line will remain. Numerically subtracting two spectra means creating a new spectrum, called “subtracted spectrum”, where in each channel the number of counts is taken as difference between the counts in the calibration and in the escape spectra. The errors of these new counts are calculated as a square root of sum of squares of the count errors in the calibration and the escape spectra.

Performing subtraction has also another advantage as it may remove possible K-LL radiative Auger peak from Kr which can be present in the region of the As calibration line. The K-LL peak was not discussed before due to its small intensity and large energy distance from a diagram line. Also to point out subtracting the escape spectrum in the region of Ni calibration line, where no lines from the radioactive source appear, can lead to removal of possible non-linear background. Presence of small amount of Ni in the radioactive source represents no problem during subtraction as it results only in

small reduction of the Ni peak amplitude. Thus, results from fitting of the subtracted spectra can be cross-checked with results from fitting of unsubtracted spectra.

During the experiment (phases II and III) the escape spectra were measured in between measurements of the calibration spectra in order to assure minimal shifts in amplifier gain, which in principle could appear, among the spectra. In Fig. 16 are shown the residuals after fit of the partial spectrum with Ni lines with linear background. In this example the $K\beta$ lines were treated in the same way as the $K\alpha$ lines, i.e. only the $K\beta_1$ parameters were fitted and parameters of the other lines were held fixed relatively to $K\beta_1$. The numerical values for the parameters can be found in the same references as for the $K\alpha$ lines [44, 56, 66]. Residuals after fit of the subtracted partial spectrum are shown in Fig. 17. A clear improvement of the fit for the subtracted spectrum is visible.

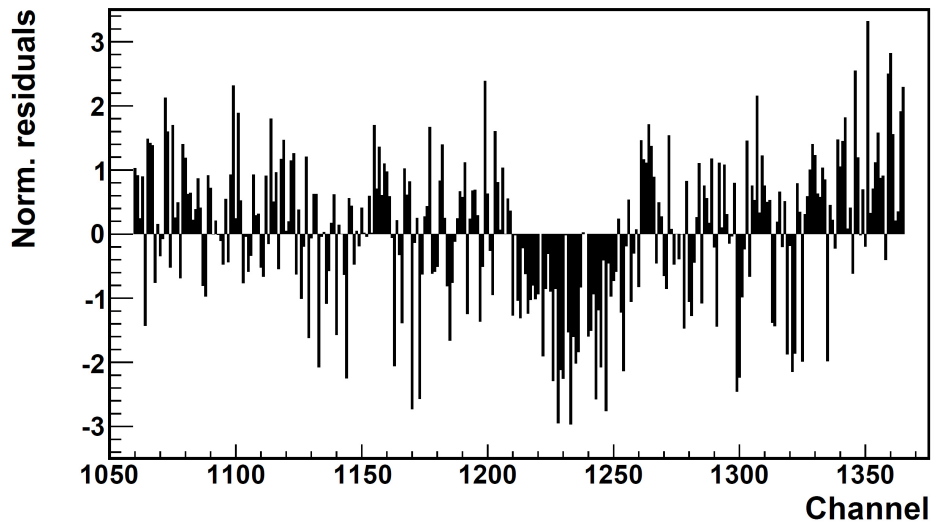


Fig. 16. Residuals after fit of Ni $K\alpha$ and $K\beta$ lines with linear background. The fitted function clearly overestimates the measured counts at around channel 1230; $\chi_{red}^2 = 1.37$.

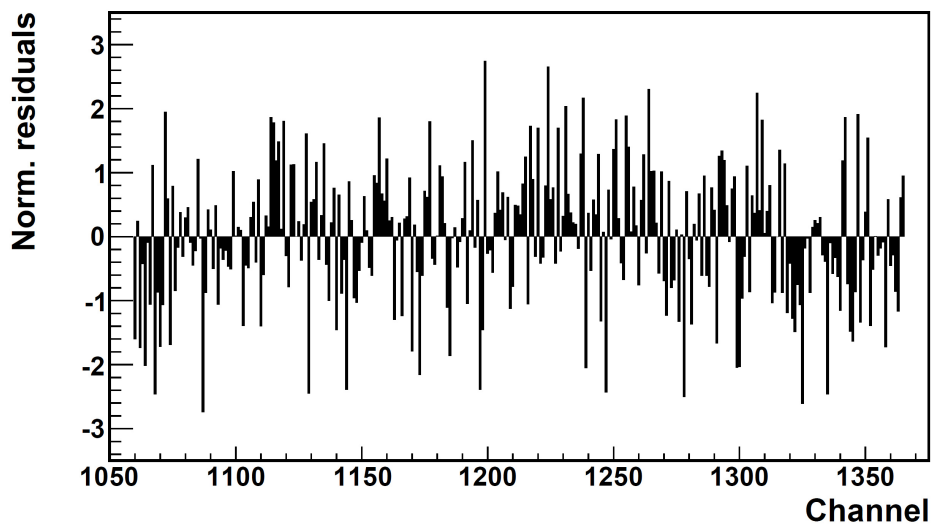


Fig. 17. Residuals after fit of Ni $K\alpha$ and $K\beta$ lines in the subtracted spectrum. The residuals at around channel 1230 disappeared; $\chi_{red}^2 = 1.11$. This clearly indicates their presence in Fig. 16 was due to non-linear background between the $K\alpha$ and $K\beta$ lines. This background is visible also in the escape spectra.

9.7 keV peak

In the calibration spectrum in Fig. 15 a background peak with energy of 9.7 keV is visible. At first sight this peak appeared to be a combination of the $L\alpha_1$ and $L\alpha_2$ line⁷ of Au as energies of these lines are 9713.44(34) eV and 9628.05(33) eV [56]. For that reason the peak was described as two constrained Voigt lines with fixed Γ -widths [44, 66] and with their respective slope functions. However, evaluating the energy of $L\alpha_1$ from the calibration spectra always resulted in energy shifted by about 20 eV to higher energies compared to the value from literature.

An admixture of possible Ge, which can be present in the detector material, was suspected as the energy of $K\alpha_1$ of Ge is 9886.52(11) eV [56]. In order to investigate this the following check was done. A simulated spectrum with Au $L\alpha$ lines and Ge $K\alpha$ lines was created in terms of counts and channels in a way that similar channel-to-energy calibration and peak intensities as in the experimental calibration spectra were assumed. This spectrum was then analysed by means of the standard calibration spectra fitting. It was observed for which intensity of the Ge $K\alpha$ peak the shift of 20 eV of the fitted peak is obtained. This was found to be satisfied for the Ge $K\alpha$ peak intensity of half the intensity of Au $L\alpha_1$. However, such a peak had significantly larger σ -width than what is observed in experimental spectra. The result from this is that no combination of Au and Ge lines can reproduce the effect observed experimentally.

Another suspicion fell on a possible non-tabulated γ -line emitted from the radioactive source. In order to investigate this a spectrum was measured utilizing different isotope, namely ^{81}Rb . This isotope also emits strong $K\alpha$ and $K\beta$ x-rays as ^{83}Rb but no 9.4 keV γ -line [68]. It was prepared at the Řež U-120M cyclotron via the reaction (p,2n) on highly enriched ^{82}Kr (99.9 %) with about 30 MeV of proton energy. It has half-life of only about 4.6 hours [68] so in order to acquire enough statistics the radioactive source had to be successively moved closer to the detector in some time steps. Data acquisition during the replacement was paused and resumed after the source was in the new position. The measured spectrum is depicted in Fig. 18, where the 9.7 keV peak is clearly visible. The experiment was repeated with As powder and the Ni and As characteristic x-rays were used for calibration. Again the energy of 9.7 keV peak showed the mentioned energy shift.

Origin of the 9.7 keV peak was further examined by introducing a 25 μm thick Ni foil between the $^{83}\text{Rb}/^{83\text{m}}\text{Kr}$ source and the detector. The corresponding spectrum is shown in Fig. 19. Presence of the foil resulted in attenuation of the $\gamma_{9.4}$ line and its intensity was reduced by a factor of about 200 compared to intensity without the Ni foil. The Kr $K\alpha$ was on the other hand attenuated by a less degree and its intensity dropped only about 10 times due to its higher energy. If the 9.7 keV line was emitted from the source it would drop also about 200 times like $\gamma_{9.4}$ because their energies are close together. This means the line would not be visible in the spectrum at all since without attenuation it already has small intensity. What was observed, however, that intensity of this line dropped only about 10 times, by the same value as for Kr $K\alpha$.

In order to check the tabulated energy of Au $L\alpha_1$ a thin gold foil was placed on top of the lid and the $^{83}\text{Rb}/^{83\text{m}}\text{Kr}$ source was placed aside, making fluorescence in Au possible but preventing detection of x-rays and γ -rays from the source itself. A similar procedure was done with a platinum foil. Even though a rough calibration using the Fe and Kr $K\alpha$ x-rays was done (their energy can be found in [56]) the tabulated energies were obtained within two standard deviations, i.e. 2 eV from statistical error. No shift on the level of 20 eV occurred.

⁷ The $L\alpha_1$ ($L\alpha_2$) line is emitted when an electron from the M_5 (M_4) subshell falls down to a vacancy on the L_3 subshell.

The ^{81}Rb measurement together with the attenuation measurement clearly indicate the 9.7 keV line observed in the calibration spectra is not emitted from the source but comes from the detector material and is induced by the strong Kr $K\alpha$ x-rays. Its deeper origin, however, remains further unclear. A dedicated study might reveal its origin in the future. At present it is considered purely as a background peak.

Nevertheless, a number of different approaches for the 9.7 keV peak description in the calibration spectra was tried. Specifically, besides the already mentioned doublet also a singlet peak and even subtraction of Au spectrum was examined. The latter one is based on measuring x-rays from thin Au foil induced by radiation from the $^{83}\text{Rb}/^{83\text{m}}\text{Kr}$ source. It is possible to subtract this spectrum with a coefficient different from one and in ROOT code this coefficient can be fitted. In all cases the influence on centroid position of $\gamma_{9.4}$ was negligible. Thus, the easiest way to include the 9.7 keV peak in the analysis is as a simple Gaussian function.

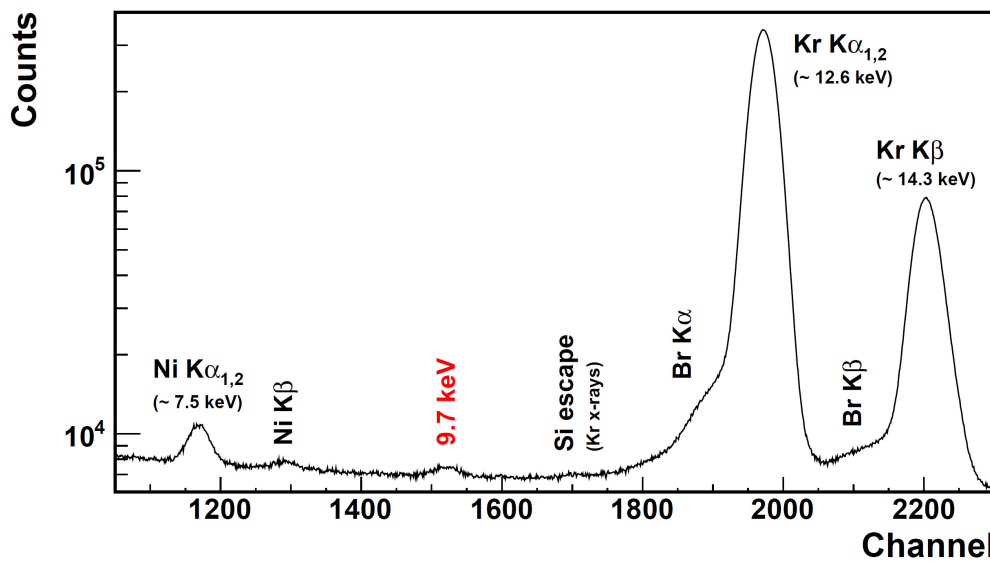


Fig. 18. A spectrum of the ^{81}Rb sample. Contamination Ni lines and possible Br lines are visible. The 9.7 keV peak is present as well.

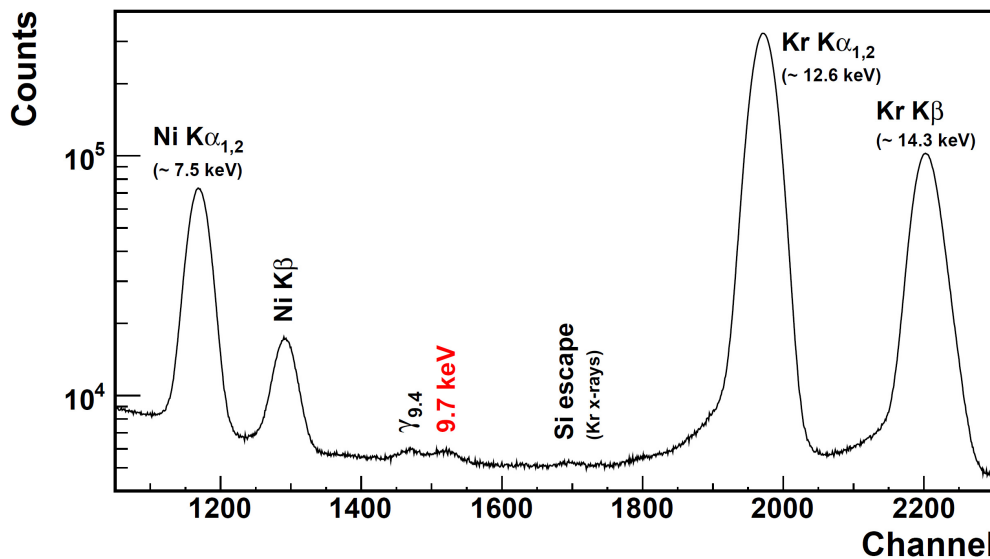


Fig. 19. The $^{83}\text{Rb}/^{83\text{m}}\text{Kr}$ spectrum with Ni attenuation foil. The $\gamma_{9.4}$ line emitted from the source has dropped two orders of magnitude in intensity, but the 9.7 keV peak has not and is still well visible.

Dead time problem

Subtraction of the escape spectrum from the calibration spectrum provided another piece of knowledge about the detector properties and possibility to improve the results. Namely, it was found out that when the average dead time of the detector was higher than about 5.5 % a significant broadening of the peaks in the spectra, especially at the baseline of the peaks, occurred. This resulted in partial overlap of the Kr $K\alpha$ line and the Si escape peak thus disturbing the high energy side of the As calibration line. The reason for such a broadening for this, in the author's opinion, quite small detector load is unknown. No steps were taken in order to investigate this issue. The calibration spectra, which were used for $E_{9,4}$ determination, were subsequently measured under dead time of maximally about 4 % to avoid broadening of the peaks. A dedicated study might be done in future to inspect the issue.

3.6. Measurement results

In all measurements distance of the radioactive source to the detector was always maintained to be between 5 and 7 cm. The time of one spectrum acquisition was set between 10 and 20 hours according to situation.

Phase I

The measurements in phase I were done with a $^{83}\text{Rb}/^{83\text{m}}\text{Kr}$ source with such amount of Ni impurity that no escape spectrum subtraction could be done for the Ni calibration line. Nevertheless, subtraction in the As calibration line region could be done without problem. For the Ni line region only the $K\alpha$ line was fitted. Four calibration spectra and six escape spectra altogether were acquired. The two slope function parameters were obtained as weighted averages from fit of $\gamma_{9,4}$ in the escape spectra (averages are from the last five spectra, i.e. the first one was excluded):

- relative slope amplitude: $A_s/A_{K\alpha_i} = 0.0223(15)$
- absolute slope width: $\beta = 44.3(42)$

There were some differences in the parameters among individual spectra as both parameters are in some way competitive. In Fig. 20 the slope area, which is just the integral over the real axis from the expression in eq. (26), for each escape spectrum is shown. Also shown is the slope area obtained from the calibration spectrum if the slope parameters in fitting of $\gamma_{9,4}$ were free. One can see that except the first escape spectrum all areas are the same within errors. Thus the mentioned differences in the parameters are not of concern once they produce correct slope area.

The obtained slope parameters were held fixed in fit of lines of Ni, As and $\gamma_{9,4}$. In the case of As line the fit was done in two ways. Firstly, the Si escape peak was described as Gaussian line. Secondly, the subtraction method was utilized. The results for $E_{9,4}$ are presented in Tab. 9. In the table only the statistical errors are presented. Systematic error for $E_{9,4}$ is presented in the next section.

The χ_{red}^2 values varied for fits of the Ni line from 1.17 to 1.36. Residuals plot showed the fitted function slightly overestimates experimental counts on the low energy side of the $K\alpha$ peak. Nevertheless, the fit overall quality was satisfactory. For the As line fit in the case of no subtraction no residual structures appeared and χ_{red}^2 varied from 0.97 to 1.13 indicating perfect fit. For the subtraction case χ_{red}^2 from 1.09 to 1.39 indicating a slightly worse but still satisfactory fit. The reason for larger χ_{red}^2 for Ni and As fits can reside in the used fixed slope parameters, which were the same for all lines.

This issue was improved in phases II and III, see further. χ_{red}^2 for $\gamma_{9.4}$ fit was from 0.96 to 1.28 and no structure in residuals emerged. Example of such a fit is shown in Fig. 21 and the corresponding residuals in Fig. 22.

The weighted average values for phase I for the two columns in Tab. 9 are

- for the case Gaussian escape peak: 9405.89(9) eV
- for the case subtraction method: 9405.84(9) eV

Phase II

The measurements in phase II were done with a $^{83}\text{Rb}/^{83\text{m}}\text{Kr}$ source cleaned from Ni impurities by means of ion-exchange chromatography prior to use. Specifically, the ^{83}Rb water solution, acidified to 0.1 M HCl (hydrochloric acid), was applied on a glass column filled with cation exchange resin AG 50W-X8, which was conditioned with 0.1 M HCl. The column was subsequently eluted with 4 ml of 0.1 M HCl, 4 ml of 0.3 M HCl, 4 ml of 0.5 M HCl and 4 ml of 1 M HCl. Activity of ^{83}Rb was then eluted into 2 M HCl and single fractions of 0.5 ml volume were collected. Combined fractions with the highest activity were transferred to a quartz beaker and evaporated to about 0.1 ml. This volume was then part by part applied on a polyethylene foil and evaporated under infrared lamp to dryness.

The impurities were not removed completely but enough for the escape spectrum subtraction to be applicable at the Ni calibration line region. In this case both $K\alpha$ and $K\beta$ series was fitted. The slope function parameters were obtained separately for each line. For the calibration lines separate fluorescence spectra were measured as described previously. One fluorescence spectrum was measured for Ni and one for As. In order to

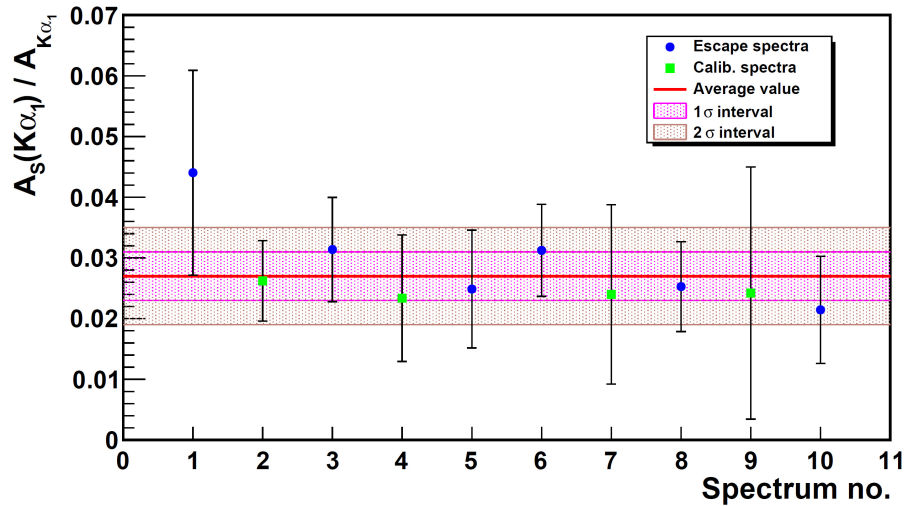


Fig. 20. The relative $K\alpha_1$ slope function amplitude A_S relatively to the amplitude of $K\alpha_1$ for various spectra in phase I. One and two standard deviations σ intervals are shown.

Value no.	$E_{9.4}$ [eV]	
	Gaussian escape peak	Subtraction method
1	9405.90(18)	9405.85(18)
2	9406.01(18)	9406.01(18)
3	9405.80(19)	9405.74(18)
4	9405.84(19)	9405.74(19)

Tab. 9. Results of $E_{9.4}$ determination in phase I. The first column with energy values corresponds to analysis of As calibration line in a way the Si escape peak is considered as Gaussian line. The second column gives results from subtraction of the escape spectrum at the As line.

obtain reliable parameters a quadratic background was used for fitting in these spectra. The parameters for $\gamma_{9,4}$ were again obtained as weighted averages from fits of the escape spectra. The slope parameters are given for all lines in Tab. 10.

Altogether three escape and two calibration spectra were acquired with a similar amplifier gain as in phase I. The results for $E_{9,4}$ are given in Tab. 11 again for two approaches - Si escape peak as Gaussian line and subtraction of the escape spectrum. χ_{red}^2 for Ni line fits were 1.11 and 1.37. The latter one shows some minor residual structures on the side of the $K\beta$ line but the part around the $K\alpha$ line was fitted smoothly. All fits of As line were without any residual structures and χ_{red}^2 was from 0.87 to 1.05. The fit of $\gamma_{9,4}$ showed similar characteristics with χ_{red}^2 of 1.02 and 1.13.

The weighted average values for phase II from the two columns in Tab. 11 are

- for the case Gaussian escape peak: 9405.76(7) eV
- for the case subtraction method: 9405.70(6) eV

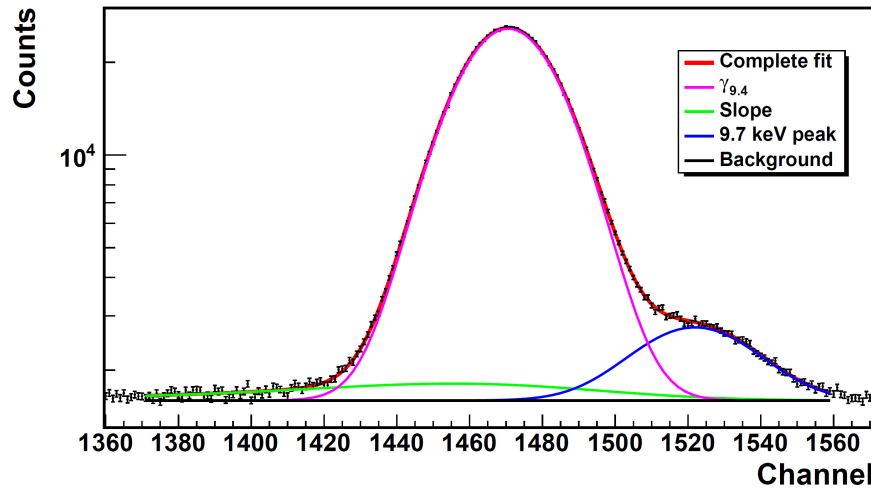


Fig. 21. Example of a fit of the $\gamma_{9,4}$ region. Note the logarithmic scale on the vertical axis.

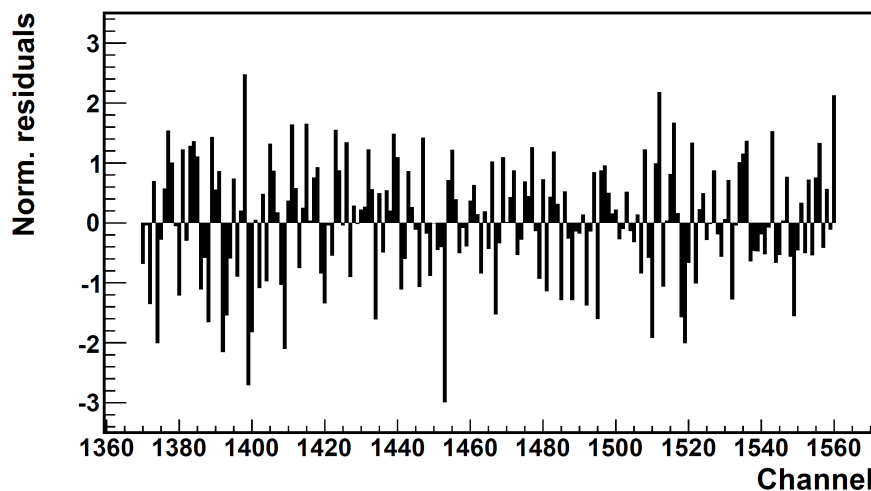


Fig. 22. Normalized residuals from the fit of $\gamma_{9,4}$ region in Fig. 21. χ_{red}^2 was 0.96 indicating good fit.

Phase III

The measurements in phase III were performed with the same $^{83}\text{Rb}/^{83\text{m}}\text{Kr}$ source as in phase II but with different amplifier gain. This was done in order to verify the linearity assumption of the ADC of the spectrometer. The procedure for $E_{9,4}$ determination was the same as in phase II. One fluorescence spectrum for Ni and one for As and two calibration together with two escape spectra were acquired. The obtained slope parameters are given in Tab. 12 and the results for $E_{9,4}$ are given in Tab. 13.

The fit results were similar as in phase II. For the Ni line fit χ_{red}^2 amounted to 1.26 and 1.01 with also some minor residual structures at the $K\beta$ line. For fit of As line χ_{red}^2 was from 1.18 to 1.28 and there were no distinguishable residual structures. Regarding $\gamma_{9,4}$ fit χ_{red}^2 was 1.42 and 1.20 with minor residual structures on the lower energy side.

The weighted average values for phase III from the two columns in Tab. 13 are

- for the case Gaussian escape peak: 9405.91(8) eV
- for the case subtraction method: 9405.78(6) eV

The weighted average values from all three phases are

- for the case Gaussian escape peak: **9405.84 ± 0.05_{stat} eV**
- for the case subtraction method: **9405.76 ± 0.04_{stat} eV**

	$A_S/A_{K\alpha_1}$	β
Ni	0.051(33)	16.8(36)
As	0.023(5)	30.7(35)
$\gamma_{9,4}$	0.035(6)	21.7(18)

Tab. 10. Slope parameters, the relative amplitude A_S and the absolute width β , as obtained for the corresponding lines in phase II.

Value no.	$E_{9,4}$ [eV]	
	Gaussian escape peak	Subtraction method
1	9405.78(9)	9405.75(8)
2	9405.74(9)	9405.65(9)

Tab. 11. Results of $E_{9,4}$ determination in phase II.

	$A_S/A_{K\alpha_1}$	β
Ni	0.087(44)	14.3(22)
As	0.042(8)	23.1(20)
$\gamma_{9,4}$	0.035(6)	21.7(18)

Tab. 12. Slope parameters, the relative amplitude A_S and the absolute width β , as obtained for the corresponding lines in phase III.

Value no.	$E_{9,4}$ [eV]	
	Gaussian escape peak	Subtraction method
1	9405.86(10)	9405.76(9)
2	9405.97(11)	9405.80(8)

Tab. 13. Results of $E_{9,4}$ determination in phase III.

Determination of Ga $K\alpha_1$ energy

In order to verify the applied procedure for $E_{9.4}$ determination an ideal situation would be to measure in the same way another γ -line which has a well-known energy close to $E_{9.4}$. Since to our knowledge no such line exists the verification can be done on a characteristic x-ray line with such properties. Such a line represents the $K\alpha_1$ of Ga the energy of which was already given in Tab. 7.

The measurement was done in the following way. Pieces of already utilized Ni, As and newly Ga (99.99 % purity) were put on top of the lid into the hollow (see geometry in Fig. 7). A 6 mm Sn collimator was used. Fluorescence in the elements was done by means of x-ray and γ -ray radiation from a commercial ^{241}Am source with activity of about 3.5 GBq. The source was placed in a thick hollow iron cylinder with opened bases and irradiated the pieces horizontally. A typical calibration spectrum is shown in Fig. 23. Altogether five calibration spectra were acquired.

Since no reference spectra, from which the slope function parameters could be obtained, were measured it was decided to do a fit of the Ni calibration line with free slope parameters and then use these parameters as fixed for the other lines separately in each spectrum. Since no subtraction could be done for the Ni line part only the $K\alpha$ line was fitted. The Ga $K\alpha$ line was also fitted separately. In the fit of As $K\alpha$ also the Ga $K\beta$ lines had to be included since they overlap significantly. They were included by standard means, i.e. only $K\beta_1$ was fitted and the others were held fixed relatively to this one. χ^2_{red} was for all fits from 0.9 to 1.3 and no residual structures appeared after the fits. Only very minor structures were apparent on the lower energy side in the case of As fit. The results for Ga $K\alpha_1$ energy are presented in Tab. 14.

The weighted average value of the obtained Ga $K\alpha_1$ energy is $9251.63 \pm 0.10_{\text{stat}}$ eV.

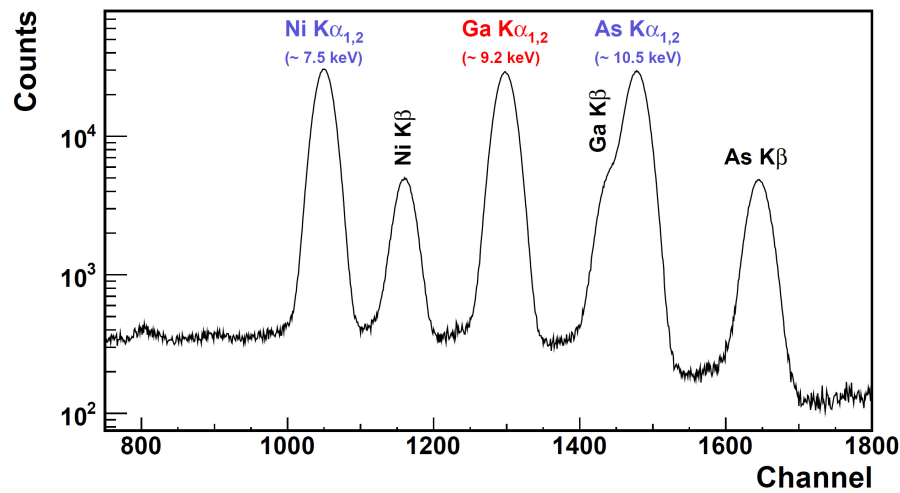


Fig. 23. A typical calibration spectrum for Ga $K\alpha_1$ energy determination. Note the logarithmic scale on the vertical axis.

Value no.	Energy of Ga $K\alpha_1$ [eV]
1	9251.74(20)
2	9251.39(25)
3	9251.76(19)
4	9251.35(27)
5	9251.69(21)

Tab. 14. Results of determination of Ge $K\alpha_1$ line energy.

3.7. Determination of systematic error

The systematic error for energy $E_{9,4}$ was determined from systematic errors of the calibration lines. The errors of the calibration lines were obtained as maximum differences of their positions obtained from fits with the fixed parameters varied inside their one standard deviation intervals. The procedure was as follows.

- 1) For one particular calibration spectrum the mean centroid positions of Ni and As $K\alpha_1$ lines were obtained using mean values of the parameters which are included as fixed in the fit. These positions shall be designated E_0^{Ni} and E_0^{As} .
- 2) In order to determine for which parameter values the maximum difference in centroid position appears the following was done. By means of a computer programme the parameters with value p_i were automatically adjusted according to their respective errors σ_i on the interval $(p_i - \sigma_i, p_i + \sigma_i)$ by the value $\sigma_i/2$ starting at $p_i - \sigma_i$. The parameters adjusted by this way were those from which the largest contribution to shift of the peak centroid position was expected, i.e. with large enough errors. These are
 - p_1 : energy difference of $K\alpha_1$ and $K\alpha_2$
 - p_2 : amplitude ratio of $K\alpha_1$ and $K\alpha_2$
 - p_3 : difference in σ -width of $K\alpha_1$ and $K\alpha_2$
 - p_4 : energy differences of satellite lines and $K\alpha_1$
 - p_5 : amplitude ratios of satellite lines and $K\alpha_1$
 - p_6 : intensities of K-LM (K-MM) RAE peaks relatively to $K\alpha_1$ ($K\beta_1$)

This means altogether 6 parameters to be varied independently. After new values for the parameters had been set a fit was done and its results were stored for each parameter combination. This means performing $5^6 = 15625$ fits, which can be done in reasonable time.

- 3) When completed the computer programme found the maximal positive and negative differences of the line centroid position and the mean position E_0^{Ni} . This maxima and minima finding did not need to be done for E_0^{As} as the combination of parameter values for which these extremes occur was determined from the Ni case. The maximum positive difference was found for

- case $(+\sigma_i)$: p_1, p_2, p_6
- case $(-\sigma_i)$: p_3, p_4, p_5

The maximum negative difference was found for the opposite configuration

- case $(+\sigma_i)$: p_3, p_4, p_5
- case $(-\sigma_i)$: p_1, p_2, p_6

- 4) In this way the positive and negative errors σ^+ and σ^- of the calibration lines were determined (in energy units)
 - for Ni $K\alpha_1$: $\sigma^+ = +0.29 \text{ eV}, \sigma^- = -0.33 \text{ eV}$
 - for As $K\alpha_1$: $\sigma^+ = +0.57 \text{ eV}, \sigma^- = -0.59 \text{ eV}$

This means for the systematic error of $E_{9,4}$ determined by linear interpolation:

$$E_{9,4} \begin{matrix} +0.41 \\ -0.42 \end{matrix} \text{ eV} \approx E_{9,4} \pm 0.4_{\text{sys}} \text{ eV}$$

3.8. Discussion of results

We obtained two values of $\gamma_{9.4}$ line energy as a result of two different approaches:

- description of the Si escape peak as Gaussian line:
 $E_{9.4} = 9405.84 \pm 0.05_{\text{stat}} \pm 0.40_{\text{sys}} \text{ eV}$
- subtraction of the Si escape peak by means of the escape spectra:
 $E_{9.4} = 9405.76 \pm 0.04_{\text{stat}} \pm 0.40_{\text{sys}} \text{ eV}$

We can see these results are the same on the level of one statistical error. Nevertheless, it is impossible to state which approach is the more correct one a which gives more realistic result. Thus, it is reasonable to take as a final result the average value and its error as the square root of sum of the individual statistical errors squared:

$$E_{9.4} = \mathbf{9405.80 \pm 0.06_{\text{stat}} \pm 0.40_{\text{sys}} \text{ eV}}.$$

Comparing our result with the published values in Tab. 2 we can see that we have a perfect agreement with the three γ -spectroscopy measurements done in the Seventies, our precision is better at least by a factor of 20, and together with that also an excellent agreement with the measurement of A. Picard. The agreement with the latest electron spectroscopy value from B. Ostrick is fairly good - at the boundary of the 2σ interval.

In determination of the $\gamma_{9.4}$ line energy a number of data from literature was taken as input. Although from the errors of these data the systematic error for the energy was obtained, an improvement on their precision would be desirable. Specifically, the energy of As $K\alpha_2$ line and also all intensities of the x-ray lines could be determined more precisely. Moreover, present day knowledge about the radiative Auger effect is very limited and could be improved as well. This, however, can not be done by means of semiconductor γ -spectrometry as higher resolution instruments are required.

3.9. Conclusion

We determined the energy of the 9.4 keV γ -ray transition observed in $^{83\text{m}}\text{Kr}$ decay as 9405.8(4) eV. This value will be used for systematic and stability studies in the KATRIN experiment. The values was obtained by means of γ -spectroscopy using a Si(Li) detector by comparison of energetically closely spaced characteristic x-ray lines of nickel and arsenic. Studies of systematic effects related to the x-rays and considerations about proper line shapes contributed to better understanding of the detector energy spectra and a reliable result.

4. Rubidium activity distribution

The ^{83}Rb atoms are transported on the substrates to produce the solid sources by either vacuum evaporation or implantation and they acquire some spatial density distribution along the substrate surface. In the case of implantation also some depth profile of the atoms is established. Knowledge on the distribution is a valuable piece of information because it will enable to do source alignment in the electron spectrometer and also provide a possibility for calculation of the spectrometer detector load, which is a standard check of measurement consistency. It also enables one to analyze K-32 conversion electron spectra with regard of possible doublet line structure as high density of ^{83}Rb atoms can cause serious local damages of the substrate and as a consequence two environments in the source with different electron binding energies can be created.

It is, however, not possible to trace the path of each atom during the production process. Therefore, a dedicated experiment to measure the spatial density distribution afterwards is required. It is the task of this chapter to give results of such a measurement which was done in cooperation with the Institute of Experimental and Applied Physics (IEAP) under the Czech Technical University in Prague by means of the Timepix position sensitive detector, which will also be briefly described. A cross-check of this measurement was done by means of a manual scan machine equipped with a lead collimator and the corresponding results are presented as well. At the end comparison of both methods is given and ^{83}Rb activity spot dimensions and ^{83}Rb density established.

4.1. Timepix measurement

Timepix detector

The Timepix detector [69, 70] is a silicon pixel device which was developed at CERN by the Medipix collaboration. The main part of the device represents a silicon detector chip with 300 μm thickness which is bump-bonded to a read-out chip. The detector chip consists of 256×256 pixels each of dimensions $55 \mu\text{m} \times 55 \mu\text{m}$. This gives the whole sensitive area the shape of a square with size of $14.08 \text{ mm} \times 14.08 \text{ mm}$. Each pixel is independent on the others in the sense it is connected to its respective preamplifier, discriminator and digital counter which are all integrated on the read-out chip. The device can be connected to a PC via the standard USB (universal serial bus) interface and the obtained data analyzed by the Pixelman software package developed at IEAP [71]. In Fig. 24 an overall view on the Timepix detector is shown.

With the Timepix device it is possible to detect various kinds of radiation: electromagnetic, electrons, alpha particles and more. The electronics also enable both to count the incoming particles and measure the energy deposited in each pixel. In our application we were interested in observation of number of photons (both x-rays and γ -rays) and electrons as these radiations are emitted after ^{83}Rb decay. For this case the data obtained from the detector are in the form of a 256×256 matrix of numbers, where each number indicates the relative intensity of any radiation registered in each pixel. From this matrix it is possible to make a radiographic image of the source, i.e. a two-dimensional colour expression of the spatial distribution of ^{83}Rb activity on the source.

The photons leave primarily only one pixel events in the detector because they are absorbed in the detector chip by the photoeffect. The electrons, on the other hand, may leave multi pixel events as they loose their energy in a series of collisions rather than at one time. With use of the analyzing software it is possible to filter the data from these multi pixel events and as a consequence obtain the result for photons and small fraction of low energy electrons only. This makes the interpretation of the obtained activity distribution clearer as blurring from the multi pixel tracks vanishes.



Fig. 24. View on the Timepix detector. Left: detector chip and chipboard with USB readout interface. Red dot on the left side marks the orientation of the solid sources during measurement, see text. Right: geometry of the measurement with source placed in the source holder and covered by a mylar foil.

Measurement setup and results

In order to obtain reliable and sharpened radiographic images of the solid sources it is necessary to move their surface as close to the detector chip surface as possible. Therefore, each source for its respective measurement was placed into a duralumin holder with diameter of 11 mm and with small input edge of 0.5 mm, i.e. the distance between the source surface and the detector was equal to this value. Also a mylar foil with areal density of 1.15 mg/cm^2 and thickness of $8.2 \mu\text{m}$ was placed under the holder in order to avoid contamination of the detector, see Fig. 24.

Time of recording of one frame, i.e. snap of the detected radiation, was always set to 1 ms. For this time the number of detected data was small enough to resolve the one pixel and multi pixel events a consequently to filter the data from high energy electron tracks as discussed previously. The image was then obtained by summing of all filtered frames acquired for the particular source. The total number of frames was chosen roughly inversely proportional to the source activity in order to obtain similar statistics for each measurement. Tab. 15 lists the total data acquisition (DAQ) time for the solid sources. The overall measurement time is larger due to the USB interface capabilities as it is possible to send only a limited number of frames per second. This, nevertheless, does not affect the results.

The images are depicted in Fig. 25 for all acquired data in order to see the activity distributions in detail and in Fig. 26 in the same colour scale for acquired data after 20 s in order to see a direct comparison of the relative activities of the solid sources. Both the horizontal axis x and the vertical axis y are in units of pixels. The whole depicted range therefore corresponds to $14.08 \text{ mm} \times 14.08 \text{ mm}$. The colour scale expresses the relative intensity measured in each pixel. The large red circle marks the edge of the duralumin holder and the red spot marks the orientation of the source in the holder - it points backwards to the USB interface, see Fig. 24. White space in the images marks that no events in these pixels were detected.

source	total DAQ time [s]
S28	265
Pt-30 #1	160
Pt-30 #2	20
Au-30	25
Pt-15	50

Tab. 15. Total data acquisition time for the solid sources measurement by means of the Timepix detector.

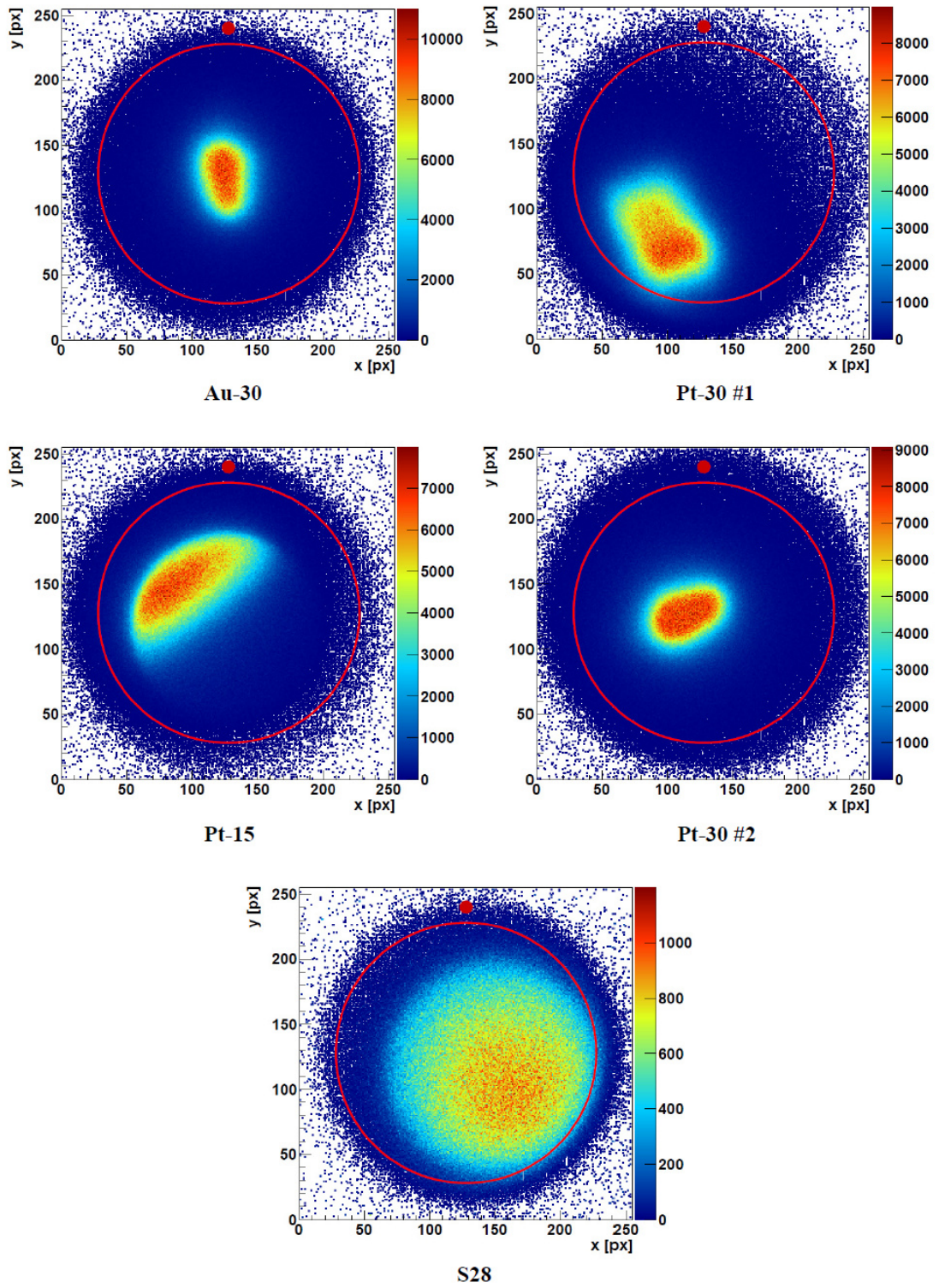


Fig. 25. Timepix radiographic images of the solid sources viewed in detail. Time of the measurement is approximately inversely proportional to the source activity.

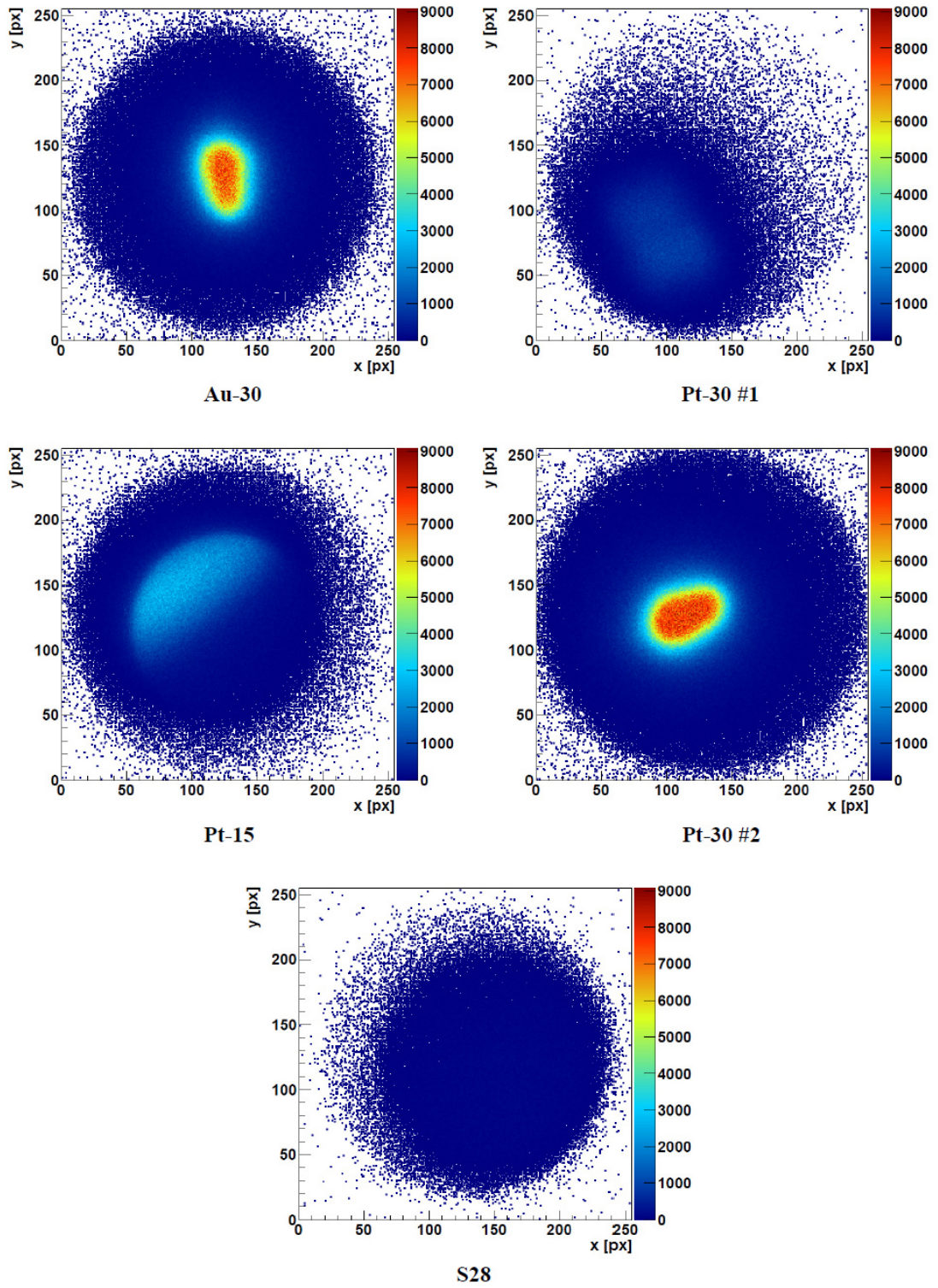


Fig. 26. Timepix radiographic images of the solid sources for the same value of acquisition time equal to 20 s.

From the radiographic images it is possible to obtain one-dimensional profiles of the activity distribution along any arbitrarily chosen direction. A special choice is that two such directions correspond to the longest axis and axis perpendicular to the longest axis of the ^{83}Rb activity spot. Any dimension of the spot needs to be defined at the full width of half maximum (FWHM) of the distribution as the boundaries of the spot are not sharply defined. Then a two dimensional Gaussian function can be used for approximation of the activity distribution. An example for the source Pt-30 #2 for the longest axis of the spot is given: in Fig. 27 the view of the profile track is shown and in Fig. 28 the profile itself is shown. In Tab. 16 the obtained dimensions of the activity spot for the solid sources from similar one-dimensional profiles are given.

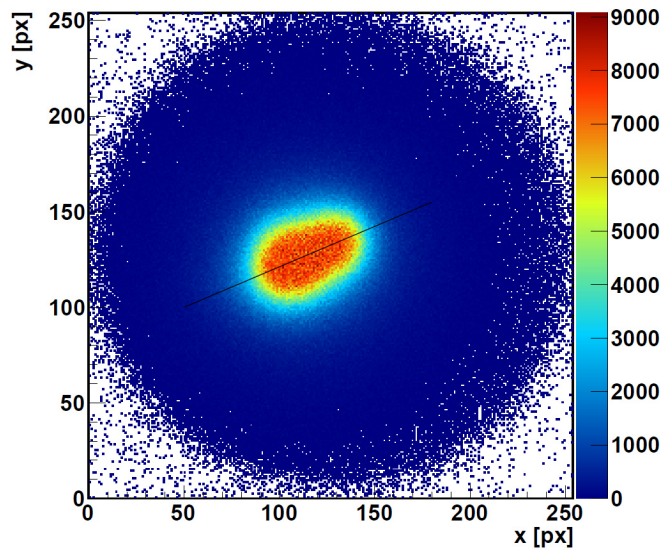


Fig. 27. View of the one-dimensional profile track along the longest axis of the Pt-30 #2 source activity spot.

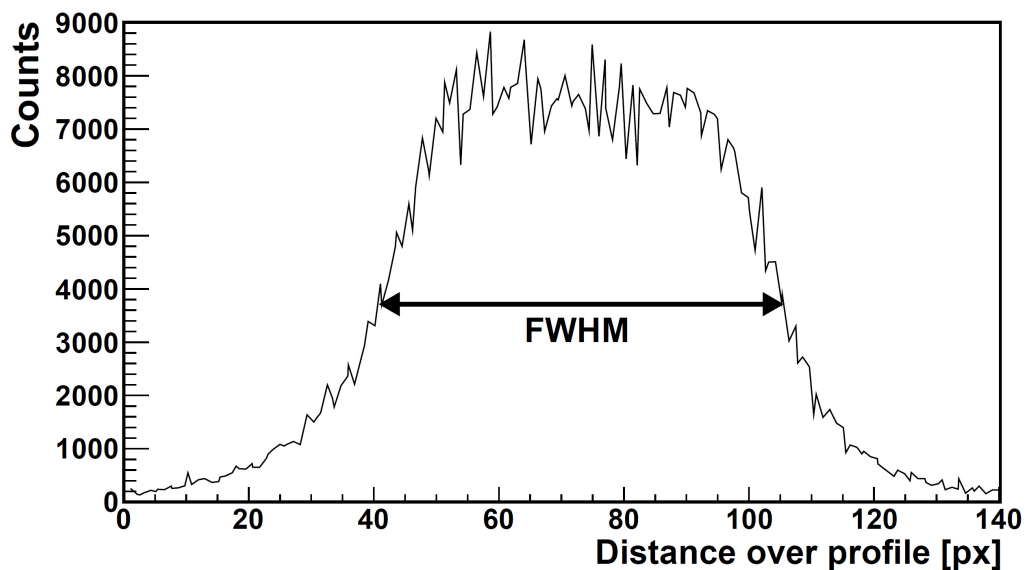


Fig. 28. One-dimensional activity profile along the longest axis of the Pt-30 #2 activity spot and visualization of the spot dimension at the full width at half maximum.

source	FWHM dimensions [mm]
S28	Ø 7.9
Pt-30 #1	4.4 × 3.2
Pt-30 #2	3.6 × 2.5
Au-30	3.3 × 2.1
Pt-15	6.0 × 3.5

Tab. 16. Obtained solid sources dimensions from FWHM of the ^{83}Rb activity spot.

4.2. Manual scan equipment measurement

Manual scan equipment

In order to independently check the results obtained by means of the Timepix detector a manual scan equipment was applied to measure the solid sources one-dimensional activity profiles. The device is equipped with Pb collimator with diameter of 0.5 mm and height of 8 mm. It can be attached on top of a standard commercial Si(Li) Canberra detector, see Fig. 29. The solid source is placed into a Cu(Au) holder with input edge of 1.2 mm and put into a compartment made for this purpose on the scan device (visible in the figure as well). The source holder is then mechanically movable by means of an adjustable wheel relatively to the fixed collimator which is set just above the detector axis. As the motion distance is controllable and known a very precise scan of the source profile by observing the intensity of x-ray $K\alpha_{1,2}$ line of Kr (energy of 12.6 keV [56]) is possible.

Measurement setup and results

For comparison the source Pt-30 #2 was chosen and installed as described previously. Starting position of the source holder was set to 2 mm from the holder edge and the scan step was maintained to be 0.5 mm. Altogether 14 measurement steps were applied, i.e. 15 spectra measured. Time of measurement of one spectrum was set to 15 minutes. An example of one activity profile is depicted in Fig. 30. In Fig. 31 the corresponding profile obtained from the Timepix measurement is shown. It can be seen that despite the fact both profiles have similar shape the FWHM obtained from the Timepix profile is larger by 0.6 mm.

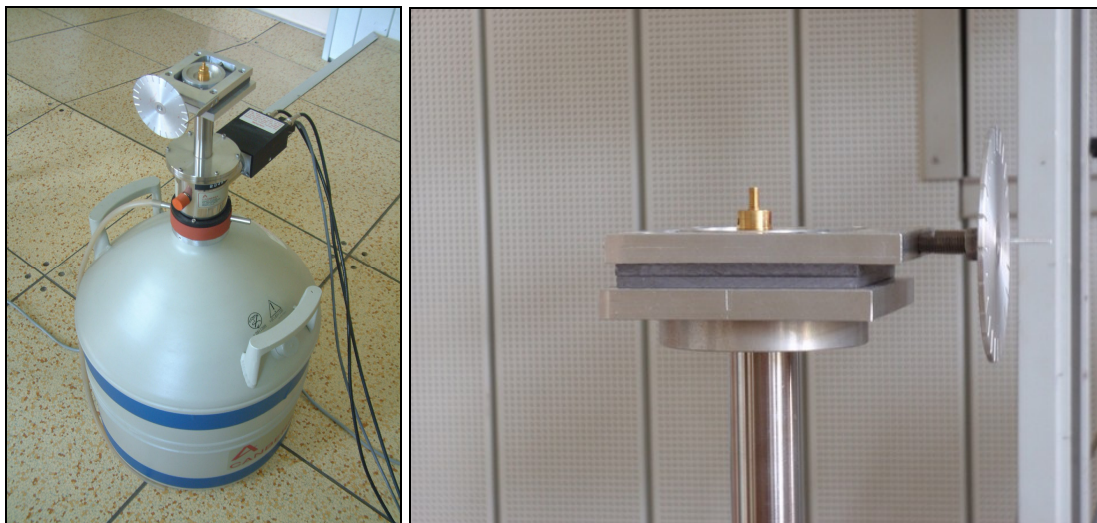


Fig. 29. View on the Pb collimator scan machine. Left: scan equipment together with source in holder installed on the Si(Li) detector. Right: closeup on the geometry.

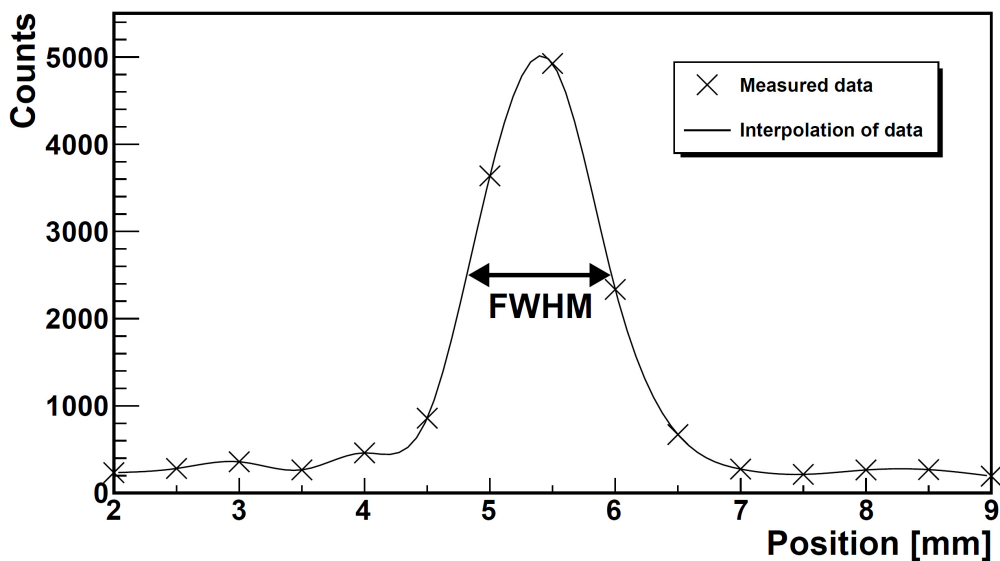


Fig. 30. Example of the activity profile of Pt-30 #2 measured with the manual scan equipment.

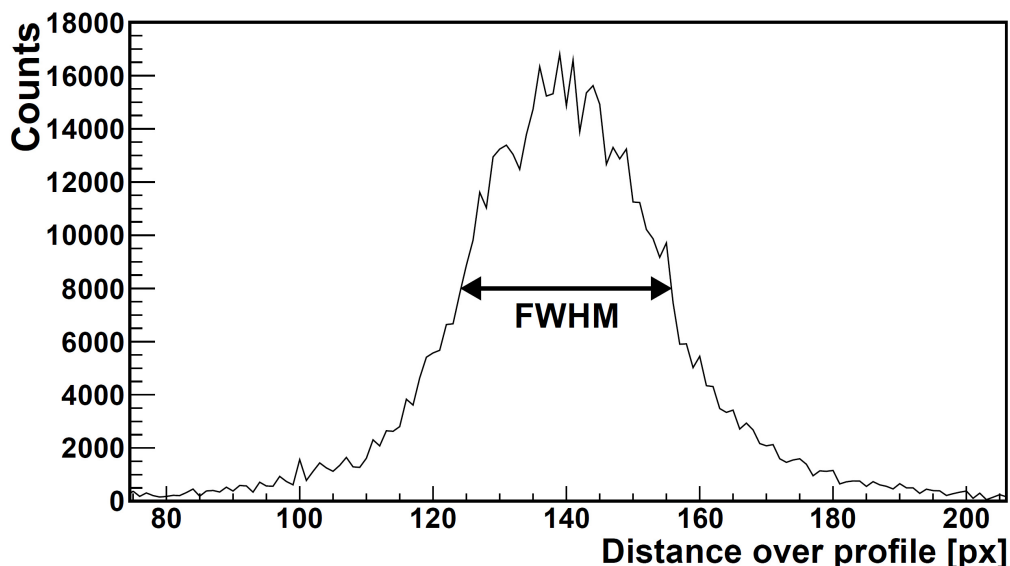


Fig. 31. Timepix activity profile of Pt-30 #2 corresponding to the profile measured with the scan equipment, see Fig. 30.

When the source activity spot dimensions are determined again for the longest axis and axis perpendicular to the longest axis, as was done in the Timepix measurement, we obtain dimensions which also differ from the Timepix ones in Tab. 16 by 0.6 mm, i.e. they are lower by this value. The discrepancy can generally be explained that some blurring is expected in Timepix measurements as the source is not placed directly on the top of the detector chip. This results in the fact no collimation of the radiation emitted from the source is done.

The correspondence between the Timepix dimensions and real ones was further investigated. If a homogeneous sharpened $^{83}\text{Rb}/^{83\text{m}}\text{Kr}$ source with known dimensions is made it can be measured the same way as the solid sources, i.e. by Timepix and the scan equipment, and its dimensions cross-checked. Therefore, such a source was prepared on a ionex paper substrate with 6 mm width and 8 mm length by dropping in about 6 MBq of ^{83}Rb water solution. The paper was then cut into three pieces from which the middle

one (in expectation to the best homogeneity), with dimensions of $2.7 \text{ mm} \times 8 \text{ mm}$, was glued on an aluminium foil and further fixed in the standard source holder. Its denomination for further reference will be *ionex*₂.

In Fig. 32 the profiles measured by the scan equipment along the longer side (rotation of 0 degrees), along the shorter side (90 degrees) and along 45 degrees are depicted. It can be seen the activity distribution is far from homogeneity. Nevertheless, if we count all points above the background and multiply the result with size of one measurement step we get the correct results for dimensions of the source, i.e. $3 \text{ mm} \times 8 \text{ mm}$ and for the 45 degrees profile, which should be equal to $2.7 \cdot \sqrt{2} = 3.8 \text{ mm}$, we get 4 mm. Therefore, this confirms that measurements with the scan equipment give true results of the source dimensions. From the profiles it is possible to obtain the corresponding FWHM's which are given in Tab. 17.

The same source was measured also by means of the Timepix detector, see the radiographic image in Fig. 33. Similar one-dimensional profiles as for the scan equipment measurement were obtained and their corresponding FWHM values determined. They are given also in Tab. 17.

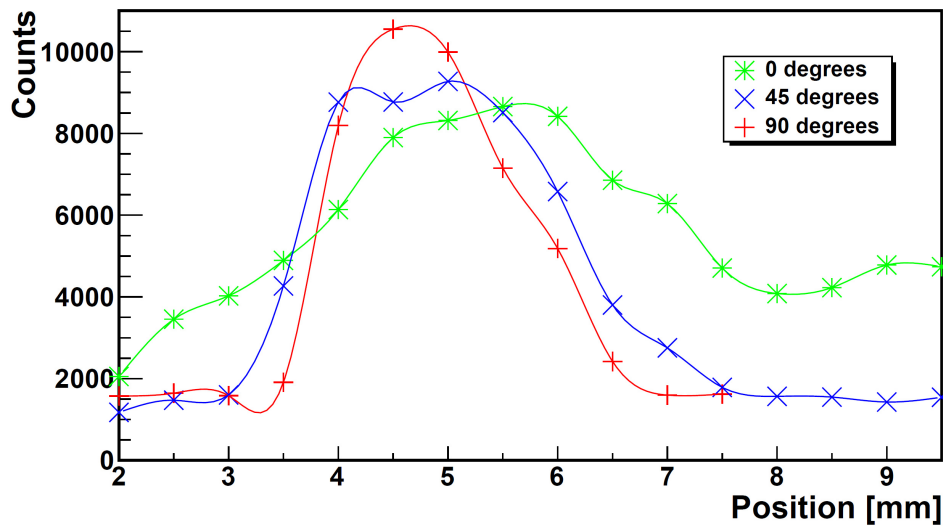


Fig. 32. Measured profiles of the dimensionally well defined source *ionex*₂ by the scan equipment.

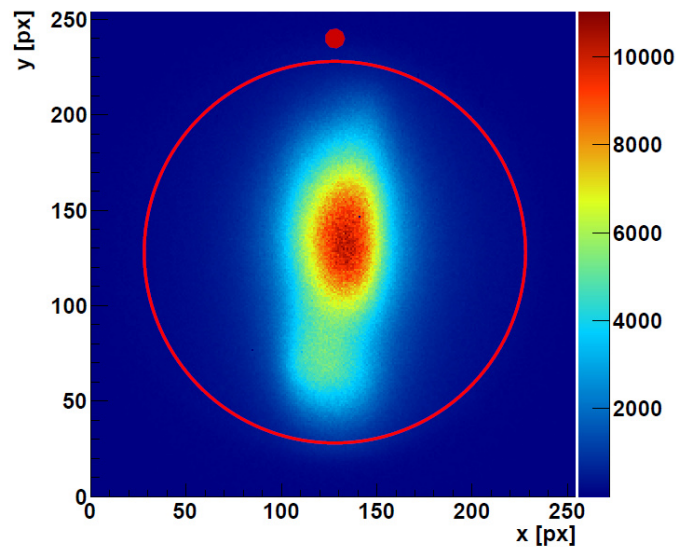


Fig. 33. Radiographic image of the source *ionex*₂ obtained with the Timepix detector.

profile	FWHM [mm]	
	scan equipment	Timepix
90 degrees	2.0	2.5
45 degrees	2.7	3.2

Tab. 17. Obtained dimensions for the source *ionex2* by the scan equipment and Timepix.

We see a difference is present for both profiles, i.e. the values obtained from the Timepix measurement are larger by 0.5 mm than those obtained by the manual scan equipment measurement. This value is close to the one established previously for the measurement of Pt-30 #2 source. This means that every FWHM value obtained by the Timepix measurement needs to be lowered by 0.6 mm in order to obtain real dimensions which are not affected by the blurring effect. Remarks on the error of this value will be discussed further.

4.3. ^{83}Rb areal density

In order to obtain the information about the maximum and mean ^{83}Rb atoms areal density the activity areal distribution $a(x, y)$ was approximated by a two-dimensional Gaussian function in the form

$$a(x, y) = K \exp\left(-\frac{(x-\mu_1)^2}{2\sigma_1^2}\right) \exp\left(-\frac{(y-\mu_2)^2}{2\sigma_2^2}\right), \quad (33)$$

where μ_i and σ_i , $i = 1, 2$, are positive parameters and K is for now an arbitrary constant. For simplicity let $\mu_i = 0$. The parameters σ_i describe the width of the shape in two orthogonal directions and correspond to our measured values FWHM_i by the relation

$$\text{FWHM}_i = 2\sqrt{2\ln 2} \sigma_i. \quad (34)$$

If we integrate over the two dimensions in eq. (33) we get

$$\int_{-\infty}^{+\infty} \int_{-\infty}^{+\infty} a(x, y) dx dy = 2\pi K \sigma_1 \sigma_2. \quad (35)$$

Integrating over the distribution is equal to summing all counts, which were measured in some time interval. This is exactly the definition of activity A (if we take the time interval to be equal to 1 s). Therefore, taking the arbitrariness of constant K into consideration, we can set

$$\int_{-\infty}^{+\infty} \int_{-\infty}^{+\infty} a(x, y) dx dy = 2\pi K \sigma_1 \sigma_2 = A. \quad (36)$$

From this follows that K can be expressed in known values as

$$K = \frac{A}{2\pi \sigma_1 \sigma_2} \quad (37)$$

and has units of $\text{Bq}\cdot\text{cm}^{-2}$. As the exponentials are dimensionless the whole function $a(x, y)$ can be interpreted as the areal density of activity of the source.

Next, it is known that the activity is in relation with the change of number of radioactive nuclei in time

$$A(t) = -\frac{dN(t)}{dt} \quad (38)$$

and this holds also for densities $a(t)$ and $n(t)$ (because the area does not change in time). From this we get

$$\begin{aligned} a_0(x, y)e^{-\lambda t} &= n_0(x, y)\lambda e^{-\lambda t} \\ n_0(x, y) &= \frac{a_0(x, y)}{\lambda}. \end{aligned} \quad (39)$$

The index 0 marks initial values, i.e. at time $t = 0$. It will further be omitted.

Now, we are firstly interested in the maximal density of ^{83}Rb atoms n_{max} . In the maximum holds $a_{max} = K$ and using eq. (34), (37) and (39) we can express the density of Rb atoms as

$$\boxed{n_{max} = \frac{4AT_{1/2}}{\pi ab}}, \quad (40)$$

where $T_{1/2}$ is the half-life of ^{83}Rb and $a \equiv FWHM_1$, $b \equiv FWHM_2$. Secondly, we would also like to know the mean density \bar{n} of ^{83}Rb atoms located inside an ellipse with axes of dimensions a and b . The mean density can be calculated

$$\bar{n} = \frac{4T_{1/2}K}{\pi ab \ln 2} \int_0^{2\pi} \int_0^{a/2} \exp\left(-\frac{r^2 \cos^2 \varphi}{2\sigma_1^2}\right) \exp\left(-\frac{d^2 r^2 \sin^2 \varphi}{2\sigma_2^2}\right) dr d\varphi, \quad (41)$$

where the original integral (36) has been transformed into elliptical coordinates (i.e. $x = r \cos \varphi$, $y = d r \sin \varphi$) and $d = \sigma_2 / \sigma_1$. The integral can be calculated numerically and after division by the denominator in K in eq. (37) it always gives the result 0.5. Therefore,

$$\boxed{\bar{n} = \frac{2AT_{1/2}}{\pi ab \ln 2}}. \quad (42)$$

In Tab. 18 the following information is given: the FWHM dimensions of the solid sources subtracted by 0.6 mm from the original values in Tab. 16, the activity of the sources after production and maximal n_{max} and mean \bar{n} densities of ^{83}Rb atoms calculated from eq. (40) and (42).

4.4. Discussion of results

The Timepix detector showed itself to be a reliable device for determination of the areal activity distribution of the solid sources due to its significantly large spatial resolution and capabilities of the fast connection interface and analysing software. Its main advantage rests in possibility of observing the activity distribution of the whole source simultaneously which is completely missing in the manual scan equipment measurements.

source	a [mm]	b [mm]	A [MBq]	n_{max} [10^{14} cm^{-2}]	\bar{n} [10^{14} cm^{-2}]
S28	7.3	7.3	5.0	0.9	0.6
Pt-30 #1	3.8	2.6	3.3	3.2	2.3
Pt-30 #2	3.0	1.9	4.8	8.0	5.8
Au-30	2.7	1.5	3.3	7.7	5.6
Pt-15	5.4	2.9	2.0	1.2	0.9

Tab. 18. FWHM dimensions a and b of the solid sources reduced by 0.6 mm, activity A of the sources directly after production and maximal n_{max} and mean \bar{n} ^{83}Rb areal densities calculated from approximation of the activity spot by a two-dimensional Gaussian function.

The obtained radiographic images in Fig. 25 show for the implanted sources that the ^{83}Rb activity is positioned in specific location in each substrate. Moreover, the activity spot size is relatively small compared to the substrate size. A small exception from the usual spot dimensions is the spot of the source Pt-15 during whose production a retarding system for ^{83}Rb atoms was used in order to achieve the 15 keV of implantation energy. We can see this resulted in some defocusing of the beam. The image of the vacuum evaporated source S28 shows expected distribution which is homogeneous in approximation due to the mechanism used for its production.

Due to a nonzero distance of the source from the Timepix chip a blurring is expected to be present in the images and consequently in the one-dimensional profiles from which the dimensions of the sources are determined. This expectation was confirmed by the scan equipment measurement and the Timepix obtained dimensions had to be subtracted by 0.6 mm in order to obtain blurring-free values.

As far as the ^{83}Rb density is concerned, it is known from [72] that density values lower than 10^{12} cm^{-2} are considered as low dose and densities higher than 10^{14} cm^{-2} are considered as high dose. At low dose individual local damages of the substrate are separated and at high dose they tend to join together which can lead to creation of zones with different properties. From Tab. 18 we can see that for the implanted sources there is a risk for such high dose effects. This can lead to possible differences of electron binding energies and subsequently to doublet line structure in electron spectra, which indeed is reported to be seen [73]. As a result the following is recommended: less ^{83}Rb atoms should be implanted and the ^{83}Rb beam should be made to vibrate during implantation. After the implantation eventually positive influence of the source annealing should be tested.

All calculations and results in this chapter are affected by the correction value for the Timepix values of 0.6 mm. This number is based on comparison of measurements which both are liable to statistical fluctuations of the individual data points. Moreover, the FWHM obtained from the scan equipment measurement is based on interpolation of the data points. In addition to that the collimator diameter of 0.5 mm brings another uncertainty as the detector may see at once a part of the source where its activity distribution may be changing rapidly, i.e. there may be a non-negligible change of the distribution over distances smaller than 0.5 mm.

All these facts bring into the correction of 0.6 mm uncertainties which are hard to be estimated reliably. The error is certainly at the order of tens of percent but without sophisticated experimental studies and Monte Carlo simulations for the specific geometry used it is not possible to determine the error more precisely. Nevertheless, the exact study of the blurring effect was not the main task of the measurements. This means the important facts are knowledge on the activity spot dimensions with fairly

good precision and ability to determine whether a second environment in any source is expected or not and this certainly was achieved.

4.5. Conclusion

In the electron spectrometer an alignment of the solid $^{83}\text{Rb}/^{83\text{m}}\text{Kr}$ source is necessary for proper functioning of the spectrometer. A calculation of the expected detector load as a check of measurement consistency is desirable as well. Both these procedures can be completed with knowledge of the ^{83}Rb activity areal distribution on the solid sources. In addition, this knowledge also provides determination of the possibility of a doublet line structure in electron spectra. This doublet may appear as a result of changes of electron binding energies due to presence of two different environments in the source when density of ^{83}Rb atoms is high enough.

The activity distribution for the solid sources was obtained by means of the Timepix position and energy sensitive detector and the corresponding radiographic images are depicted in Fig. 25. From these images it was possible to obtain one-dimensional profiles of the activity spot along the longest axis and axis perpendicular to the longest axis, see example in Fig. 28. The profiles enabled us to determine the dimensions of the activity spot at FWHM, see Tab. 16.

An independent check of the obtained results was done by means of the manual scan equipment. Similar one-dimensional profiles were obtained, see Fig. 30, and the corresponding dimensions at FWHM determined. It was, however, found out that the Timepix values are larger by 0.6 mm.

In order to further understand the correspondence between real and Timepix dimensions an attempt to make a special homogeneous and dimensionally well-defined source was performed. From measurement of this source by Timepix and the scan equipment the difference was confirmed and explained as a result of blurring in Timepix measurement. The cause for this blurring is the nonzero distance of the source to the Timepix detector chip and absence of collimation of the radiation emitted from the source.

The final results of activity spot dimensions at FWHM of the solid sources are shown in Tab. 18 together with estimated maximum ^{83}Rb atoms densities. Based on information from literature it was found out that the density for the implanted sources is high enough that environments in the substrate with different properties can possibly appear. This would result in doublet line structure in the electron spectra. Certain recommendations were given in order to reduce the risk of high ^{83}Rb doses in the future.

5. ^{83m}Kr retention

The daughter product of ⁸³Rb decay in the solid sources, the isomeric state ^{83m}Kr, is a gas. Dependent on the source some of this gas may escape the source well before it decays into the ground state. The conversion electrons emitted from ^{83m}Kr, however, can not be efficiently detected after this happens because in electron spectrometers the solid sources are expected to be placed in a limited space. This results in the fact that overall available count rate is reduced and stronger source (i.e. with higher Rb activity) has to be used in order to compensate it. Knowledge of how much Kr escapes the source and how much remains inside thus provides valuable information on expected Kr activity, i.e. also on the number of conversion electrons leaving the source. It is the task of this chapter to give results of gamma spectroscopy measurement of such a feature.

The quantity describing this feature of a solid source is called retention. It is a number between 0 and 1 in relative units (or equivalently between 0 % and 100 %) and is defined as portion of Kr atoms which remain in the source out of all Kr atoms produced by decay. For example, 0 % means that all Kr atoms escape the source before their own decay takes place and 100 % means that all Kr atoms remain inside the source and also decay there.

Two methods of measuring the retention were tested - comparison of intensities of gamma lines with energies of 32 keV and 9.4 keV in ⁸³Rb decay with relations in ⁸³Rb decay scheme, and comparison of 32 keV line intensities measured with source placed in a closeable chamber. Both methods will be described and compared. At the end, the retention of all sources will be established.

5.1. Method 1: Comparison of 32 keV and 9.4 keV lines intensities

5.1.1. Theory

When looking at the ⁸³Rb decay scheme in Fig. 5 it is clear that the retention of the source can be established after measuring the intensities of 9.4 keV and 32 keV lines. Let the fraction which feeds the 9.4 keV energy level except from the 32 keV transition be k . Then the line intensity $I_\gamma(9.4)$ can be expressed as

$$I_\gamma(9.4) = [k + (1-k)R] \frac{1}{1 + \alpha_{tot}(9.4)}, \quad (43)$$

where R is the retention in relative units and $\alpha_{tot}(9.4)$ is the total internal conversion coefficient for this transition. As the 42 keV level decays only by 32 keV transition we can use for the intensity of 32 keV line $I_\gamma(32)$ the expression

$$I_\gamma(32) = (1-k)R \frac{1}{1 + \alpha_{tot}(32)}. \quad (44)$$

Actually, it is not necessary to know the internal conversion coefficients as the ratio $I_\gamma(32)/I_\gamma(9.4)$ has been measured experimentally for $R = 1$ in [74], i.e. in this case

$$\frac{I_\gamma(32)}{I_\gamma(9.4)} = (1-k) \frac{1 + \alpha_{tot}(9.4)}{1 + \alpha_{tot}(32)} \equiv v = (6.11 \pm 1.59) \cdot 10^{-3}. \quad (45)$$

In measurement with gamma detector we measure the intensity of a line of energy E with some efficiency ε and we get its area A as $A_\gamma(E) = I_\gamma(E) \varepsilon_\gamma(E)$. This means for the ratio of intensities of 9.4 keV and 32 keV line

$$\frac{I_\gamma(32)}{I_\gamma(9.4)} = \frac{A_\gamma(32)}{A_\gamma(9.4)} \frac{\varepsilon_\gamma(9.4)}{\varepsilon_\gamma(32)} = \frac{A_\gamma(32)}{A_\gamma(9.4)} \varepsilon_{rel} \cdot \quad (46)$$

Since ε_{rel} can be established experimentally for particular detector we can use eq. (43) through (46) and express the retention in relative units as

$$R = \varepsilon_{rel} \frac{A(32)}{A(9.4)} \cdot \frac{k}{v - \varepsilon_{rel} \frac{A(32)}{A(9.4)} (1-k)} \cdot \quad (47)$$

5.1.2. Measurement results and discussion

The measurement was done for all five sources. The areas of the γ -lines were obtained by a fit in ROOT framework. The lines were described by Gaussian function on a linear background. It was found previously that for applied geometry $\varepsilon_{rel} = 0.68$. We also know from the decay scheme of ^{83}Rb that the fraction $k = 0.23$ ($= 0.064 + 0.16 + 0.0066$ when rounded and when the other small contribution is neglected). Tab. 19 lists for all sources obtained result of retention as the weighted average of retention calculated from individual spectra from eq. (47). Time of measurement of each spectrum was 5 hours. The errors of parameters v , ε_{rel} and k are not included.

Discussion of results

The method had been used previously for orientation establishment of the retention for vacuum evaporated sources. In determining the errors it is necessary to include aside from the errors of the areas also the errors of the parameters v , ε_{rel} and k . While errors of ε_{rel} and k amount to 5 % the error of v is about 25 %. However, changing v in eq. (47) inside the $\pm 1\sigma$ interval may change the retention up to ± 50 %. This is of course not acceptable as we want to know the retention with error up to a few percent maximum. An improvement on the calculation would be to know the value v more precisely.

A systematic shift was found for the measurements of sources with platinum pad. The problem lies in the fact that Pt $L\alpha$ lines, which are greatly induced in the pad as fluorescent x-rays, coincide energetically with 9.4 keV line. According to [56] the energy of Pt $L\alpha_1$ is 9442.39(32) eV and energy of Pt $L\alpha_2$ is 9361.96(21) eV. The energy of 9.4 keV line is between these two values and the detector resolution does not allow us to resolve these lines among each other. As a result the area of 9.4 keV line is strongly enhanced and consequently the retention is reduced.

source	retention [%]
S28	27 ± 2
Pt-30 #1	25.0 ± 0.5 *
Pt-30 #2	26.1 ± 0.3 *
Au-30	99 ± 3
Pt-15	23.0 ± 0.3 *

Tab. 19. Obtained values of retention for the solid sources with means of method 1: comparison of 9.4 keV and 32 keV γ -lines intensities. The 1σ errors of the retention are given by statistical errors of the lines areas only. *Retention established for Pt sources has a systematic shift, see the text.

Nevertheless, despite these disadvantages we can see the fact that the retention of the implanted Au-30 source is very high and quite close to 100 % in contrast to the vacuum evaporated source S28.

5.2. Method 2: Closeable chamber

5.2.1. Method description

Taking major disadvantages of the previous method into consideration a second method, which uses a closeable chamber, was developed. When a source is placed into an open chamber the krypton gas may freely leave the chamber as it would if there was no chamber at all. In this configuration we detect the 32 keV line intensity which exactly corresponds to the retention of the source. On the other hand, if the chamber is closed from outer environment all the krypton gas accumulates inside and we detect the line intensity corresponding to 100 % retention (if there is a passage way for the gamma rays to reach the detector). In first approximation, by just dividing the measured areas of the 32 keV line A_{open} and A_{closed} we get the retention R in relative units

$$R = \frac{A_{open}}{A_{closed}}. \quad (48)$$

Again, this is justifiable as if the source had 0 % retention we would see no 32 keV line at all when placed in the open chamber, if it had 100 % retention we would see the same line areas in both open and closed configurations.

This approach has a clear advantage - we get rid of the parameters ν , ϵ_{rel} and k , which the previous method incorporates. As no other lines are energetically close to 32 keV line, also no interference from other lines occurs. The situation is, however, not so straightforward as the simple ratio in eq. (48) gives shifted result if some corrections are not taken into account. Specifically, two corrections are of concern: correction for ^{83}Rb decay and correction for finite volume of the chamber. It is also important for avoidance of a systematic error to have knowledge about $^{83\text{m}}\text{Kr}$ - ^{83}Rb transient equilibrium. All these features are to a large extent calculable theoretically and are described and derived further.

Chamber realization

The chamber was assembled using DN-10-KF vacuum components and a photo of it when dismantled is shown in Fig. 34. The scheme of the chamber with dimensions is depicted in Fig. 35. It consists of a standard blank flange, a blank plexi-glass flange with thin window, a centering ring, a standard rubber o-ring, a cut o-ring and clamping rings. The cut in the o-ring together with radial hole in the centering ring serves as a passage way for $^{83\text{m}}\text{Kr}$ atoms in the open configuration to left the chamber into open space. The window in the plexi-glass flange with thickness of 1.4 mm enables to detect the 32 keV γ -rays with small attenuation.

5.2.2. Correction for ^{83}Rb decay

The retention calculation by division of the line areas relies on constancy of the source activity. However, as ^{83}Rb decays with half-life of 86 days, the same activity can not be maintained for both measurements. The two measured spectra, which correspond to open and closed chamber configurations, are obtained in different times and this difference is not negligible compared to the rubidium half-life. Nevertheless, a correction based on the exponential decay law is calculable.

The activity A of ^{83}Rb is described as a function of time t by the familiar law (see Fig. 36)

$$A(t) = A_0 e^{-\lambda t}, \quad (49)$$

where A_0 is the activity in time $t = 0$ and λ is the decay constant. Eq. (49) is in general valid not only for the overall source activity but also for count rate of any of desired gamma lines. This is applicable also for the 32 keV line even if it originates in the daughter nucleus $^{83\text{m}}\text{Kr}$ whenever the transient equilibrium of both rubidium and krypton decays is established. It is therefore applicable for both open and closed configurations if waiting for the transient equilibrium to occur after closure is done (see further).

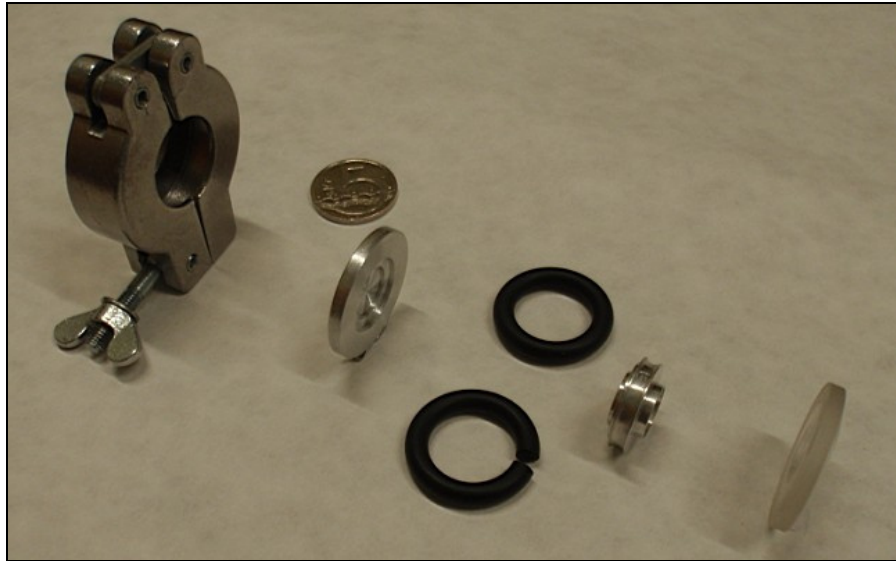


Fig. 34. Photograph of the dismantled chamber components. A coin is present for comparison of size.

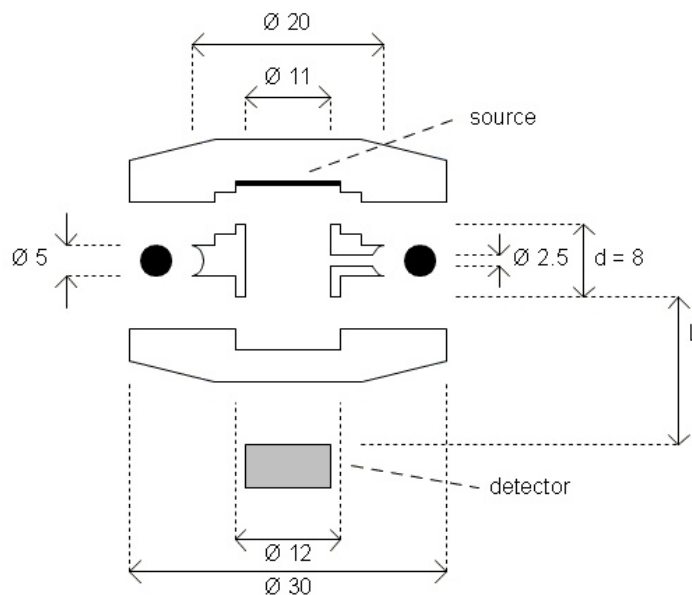


Fig. 35. Schematic layout and dimensions of the dismantled chamber. The dimensions are given in mm. The plexi-glass is positioned as the closest part to the detector which is depicted as grey rectangle in the bottom. The solid source is held on top of the chamber volume. The value d is height of the free volume in the chamber. The value L is defined as the distance between the bottom of the chamber and surface of the detector, i.e. the distance between the solid source and the detector surface equals $L+d$. Both of these values are used in the text.

Suppose we measure the line counts from time t_1 to time t_2 and again from t_3 to t_4 , $t_1 < t_2 < t_3 < t_4$. This is exactly what we do when determining the krypton retention. The number of counts N is equal to the area below the curve described by eq. (49), see Fig. 36, and expressed mathematically as (the lower index indicates the first or the second measurement)

$$N_1(t_1, t_2) = \int_{t_1}^{t_2} A(t') dt' = \int_{t_1}^{t_2} A_{01} e^{-\lambda t'} dt' = -\frac{A_{01}}{\lambda} (e^{-\lambda t_2} - e^{-\lambda t_1}), \quad (50)$$

analogously for $N_2(t_3, t_4)$. It is clearly seen that generally $N_1(t_1, t_2) \neq N_2(t_3, t_4)$ even if we ensure the same measurement conditions (which would give $A_{01} = A_{02}$). These conditions are not the same as we compare number of counts from open and closed chamber measurements. Now all we want to do is to express $N_1(t_1, t_2)$ with means of times t_3 and t_4 , i.e. to determine how much would it be if we measured from t_3 to t_4 . Obviously,

$$N_1(t_3, t_4) = -\frac{A_{01}}{\lambda} (e^{-\lambda t_4} - e^{-\lambda t_3}) \quad (51)$$

and using eq. (50) and (51) we get

$$N_1(t_3, t_4) = \frac{e^{-\lambda t_4} - e^{-\lambda t_3}}{e^{-\lambda t_2} - e^{-\lambda t_1}} N_1(t_1, t_2). \quad (52)$$

As $N_1(t_1, t_2)$ and $N_2(t_3, t_4)$ are measured experimentally and everything else is known the krypton retention can be obtained by proper division of $N_2(t_3, t_4)$ by $N_1(t_3, t_4)$ or vice versa, depending on open / closed chamber assignment.

5.2.3. ^{83m}Kr transient equilibrium with ^{83}Rb in closed chamber

Whenever a source does not have 100% krypton retention, after closing it into the chamber the krypton begins to accumulate until there is enough of it that it decays at the same rate it is created from rubidium. At this point it is said transient equilibrium between rubidium and krypton decay has been established. Let us calculate explicitly

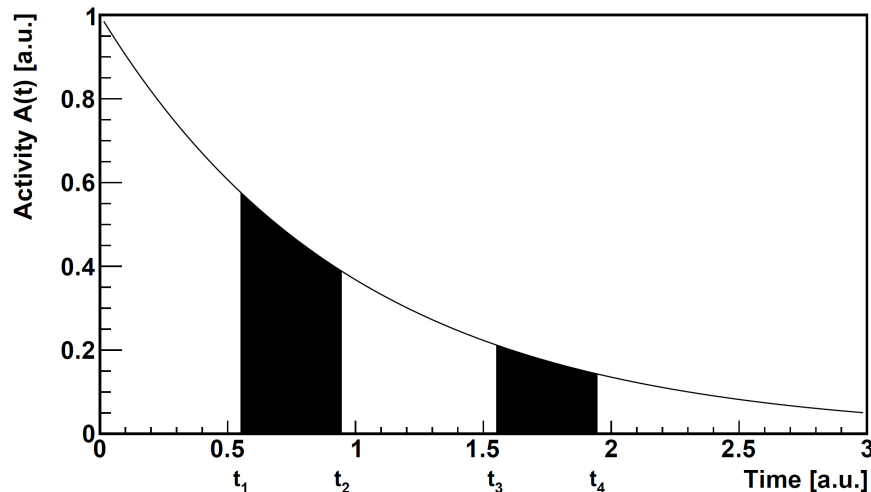


Fig. 36. Exponential decay illustration. Number of measured counts as area under the curve.

after how much time this situation occurs.

Firstly, the ^{83}Rb atoms undergo radioactive decay and their number N as a function of time t satisfies the well-known relation with decay constant λ ($= 9.307 \cdot 10^{-8} \text{ s}^{-1}$)

$$\frac{dN(t)}{dt} = -\lambda N(t). \quad (53)$$

This immediately leads to the exponential law in eq. (49) (with A replaced by N). Secondly, the $^{83\text{m}}\text{Kr}$ atoms are being continuously generated from the decaying Rb atoms, but undergo their own decay as well with decay constant λ_2 ($= 1.052 \cdot 10^{-4} \text{ s}^{-1}$)

$$\frac{dN_2(t)}{dt} = -\lambda_2 N_2(t) + \lambda N(t). \quad (54)$$

When we insert the solution of eq. (53) into eq. (54) we get

$$\frac{dN_2(t)}{dt} = -\lambda_2 N_2(t) + \lambda N_0 e^{-\lambda t}. \quad (55)$$

This is the equation for the unknown time function of isomeric Kr atoms number. It leads to the solution

$$\boxed{N_2(t) = \frac{N_0 \lambda}{\lambda_2 - \lambda} \left[(R-1)e^{-\lambda_2 t} + e^{-\lambda t} \right]}, \quad (56)$$

where R is the retention of the source in relative units, i.e. the initial number of $^{83\text{m}}\text{Kr}$ atoms is incorporated.

The function (56) is depicted in Fig. 37 (in arbitrary scale, starting at zero number of $^{83\text{m}}\text{Kr}$ atoms in the beginning). The transient equilibrium occurs after such time t_{trans} for which the first exponential in eq. (56) is negligible to the second one, i.e. when $^{83\text{m}}\text{Kr}$ nuclei decay at the same rate as Rb atoms. For decay constants corresponding to our situation the time t_{trans} was chosen to be 13 hours as for this value $e^{-\lambda_2 t_{trans}} / e^{-\lambda t_{trans}} \approx 0.007$ so the contribution of the first exponential to the whole function is less than 1 %. For sources with retention higher than 0 % the contribution is even smaller due to the presence of R in eq. (56).

5.2.4. Correction for finite volume of closed chamber

When determining the krypton retention it is assumed in eq. (48) the source of gamma rays is located in the same distance from the detector for both open and closed measurements. However, in fact this does not hold. When closed, the conditions in the chamber are more like the situation depicted in Fig. 38 - the source is held on the top of the chamber and the rest of the krypton gas is located beneath it towards the detector. If the source itself has retention R , i.e. out of possible $^{83\text{m}}\text{Kr}$ atoms number in the chamber a fraction R is located in the source, then the remaining $^{83\text{m}}\text{Kr}$ gas in the rest of the chamber volume corresponds to the fraction $1 - R$.

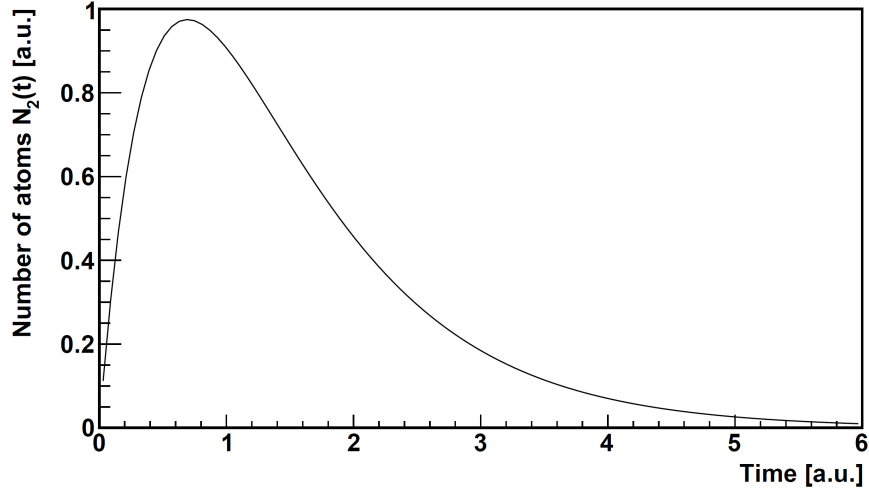


Fig. 37. Time evolution of ^{83m}Kr atoms number (taken with arbitrary decay constants, $\lambda_2 < \lambda$) in arbitrary time and number of atoms units. The transient equilibrium with Rb atoms is achieved for higher times on the right hand side of the figure, i.e. where the function behaves as function of exponential decay of Rb atoms.

According to the sketch in Fig. 35 the chamber height is d and distance from its bottom to the detector surface is L . Let the spatial distribution of free Kr atoms in the chamber be homogeneous. Then on each horizontal slice of infinitesimal height dr inside the chamber falls fraction $dr(1-R)/d$ of Kr atoms. If we assume radiation intensity falls down with distance r to the detector surface as $1/r^2$ (this is to be checked experimentally and by a Monte Carlo simulation, see further) the contribution to area of a spectral line from a slice in distance r from the detector is proportional to $(1-R)/(d \cdot r^2)$.

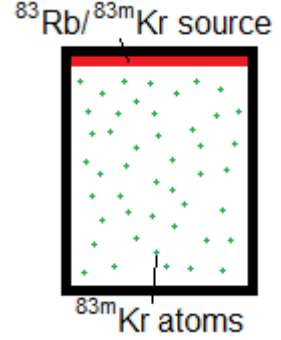


Fig. 38. Closed chamber and ^{83m}Kr atoms situation.

What we register in the detector is contribution a from all slices in the chamber

$$a = \int_L^{L+d} \frac{1-R}{d} \frac{1}{r^2} dr = \frac{1-R}{L(L+d)}. \quad (57)$$

Together with radiation from the source itself the whole registered area A_{closed} of the line is (K is a suitable constant)

$$A_{closed} = K \left[\frac{R}{(L+d)^2} + \frac{1-R}{L(L+d)} \right]. \quad (58)$$

We would like to know the real value R calculated with corrected closed area A_{closed}^{corr}

$$R = A_{open} / A_{closed}^{corr}. \quad (59)$$

This corrected value can be obtained by using eq. (58) as we know that $A_{closed}^{corr} = K / (L+d)^2$ (this means all ^{83m}Kr atoms would reside in the source itself and none of them would be present free in the chamber volume)

$$A_{closed}^{corr} = \frac{1/(L+d)^2}{R/(L+d)^2 + (1-R)/(L(L+d))} A_{closed} = \frac{1}{R + (1-R)\frac{L+d}{L}} A_{closed}. \quad (60)$$

We insert this result into eq. (59) and obtain for R

$$R = \frac{A_{open}(d+L)}{A_{open}d + A_{closed}L}. \quad (61)$$

The retention is now fully calculable from measured areas of open and closed configurations (of course after correction for ^{83}Rb decay).

This is, nevertheless, not the end of the whole problem. In the existing closed chamber there exists a volume V_{inv} in which Kr atoms reside but which is not visible to the detector as the gamma rays are not able to pass through the chamber material. This volume was estimated by micrometer measurements to be $\sim 19.2 \text{ mm}^3$. This means that from the whole value a in eq. (57) we see only the fraction $f = V/(V+V_{inv})$, where V is the volume of the closed chamber visible to the detector. As we have 11 mm diameter and 8 mm height of the chamber the volume V is equal to 760 mm^3 . Therefore, the fraction is $f = 0.975$.

Eq. (60) transforms into

$$A_{closed}^{corr} = \frac{1}{R + f(1-R)\frac{L+d}{L}} A_{closed} \quad (62)$$

and for the retention R we have

$$R = \frac{A_{open}f(d+L)}{A_{open}f(d+L) + (A_{closed} - A_{open})L}. \quad (63)$$

For further considerations this result can also be modified to

$$R = \frac{A_{open}Y}{A_{closed} + A_{open}(Y-1)}, \quad Y \equiv f \frac{d+L}{L}. \quad (64)$$

Correction for random summing

In order to compare experimental results with a simulation (see further) we have to correct them also for random summing. This is an effect which happens when two photons reach the detector simultaneously or within a time window when the detector chain is in the analysis process of the first photon, i.e. the dead time interval. The higher count rate is the more probably this situation occurs. According to [75] if the measured line area is A , count rate R and dead time τ the true line area A_T can be calculated as

$$A_T = A e^{2R\tau}. \quad (65)$$

The value τ was approximated by the detector resolution time which was set to $6 \mu\text{s}$.

5.2.5. Monte Carlo simulation to improve inverse square law dependence

From the previous discussion it is clear that the correction for finite volume of the chamber, see eq. (64), depends primarily on the $1/r^2$ dependence of the radiation intensity, where r is the distance of the infinitesimally thin slice in the chamber to the detector surface. Strictly speaking, this law holds only on a sphere (or part of it) with radius r with a point-like source placed in its center. In the case of retention measurement with closeable chamber the detector is neither a part of any thought sphere nor is the source itself point-like but rather slice-like (any height distribution of the activity inside the source can be safely neglected with respect to the dimensions of the whole setup). Because of this the dependence of radiation intensity on distance can be changed. It is difficult and time-consuming (and for smaller distances even impossible because of high dead time) to establish the altered dependence with enough experimental data so they could be reliably interpolated in between. Therefore, a Monte Carlo simulation for this task was developed in *Wolfram Mathematica 6.0*. Results of this simulation were then compared with a few experimental data points available.

The idea was to generate in the simulation random gamma rays from a source with specified energy and simulate their detection in the detector. It is exactly the same situation which happens in real measurement, although it is calculated numerically on a computer and the results are obtained much faster. Only the geometry specifications of the experiment are included and altered. As soon as the photon is simulated to be absorbed by the photoelectric effect it is taken as one count, so no simulation of charge transport inside the detector is done. This approach significantly reduces the complexity of the simulation. After all, we are only interested in how change of the geometry, especially the distance r , of the experiment affects the change of the count rate and not in the properties of the detector.

The simulation was done for discrete set of distance points and the results were interpolated inside the whole region of interest. The interpolated function $S(r)$, i.e. the dependence of number of counts on distance r , can be used for a more reliable correction for finite volume of the chamber. The situation is very similar to what has been shown previously, see eq. (58). The area A_{closed} will now be

$$A_{closed} = K' \left[R S(L+d) + \frac{1-R}{d} \int_L^{L+d} S(x) dx \right]. \quad (66)$$

Let us label for simplicity for given L and d :

$$S(L+d) \equiv s, \quad \int_L^{L+d} S(x) dx \equiv S. \quad (67)$$

From that follows

$$A_{closed}^{corr} = \frac{s}{R s + f \frac{1-R}{d} S} A_{closed} = \frac{1}{R + f \frac{1-R}{d} \frac{S}{s}} A_{closed} \quad (68)$$

and for retention we have (in the same form as in eq. (64) for comparison)

$$R = \frac{A_{open} X}{A_{closed} + A_{open} (X-1)}, \quad X \equiv \frac{f S}{d s}. \quad (69)$$

In the simulation the following configuration and processes were used:

- circular homogeneous isotropic source with diameter of 11 mm placed in a distance r above the detector upper surface
- homogeneous detector of cylindrical shape with diameter of 10 mm and height of 5 mm made of silicon
- standard photoelectric effect with cross-section dependent on radiation energy; after this effect takes place the photon is detected as a count
- coherent scattering of radiation inside the detector with cross-section dependent on radiation energy; after it scatters the photon may interact again (via the photoelectric effect or again the coherent scattering) or may escape the detector

The diameter of the simulated source corresponds to the diameter of the individual slices of ^{83m}Kr gas inside the chamber volume. The dimensions of the detector are provided by the manufacturer. The mentioned interactions of photons with matter are two of the three possibilities for energies around 32 keV. The third possibility is incoherent scattering and represents much more complicated process for simulation. The photon may lose only that much energy as to excite an electron but not enough to free it and also only portion of the photon energy may be detected as the photon with remaining energy may escape the detector. In further considerations this type of scattering will be neglected because of these substantial difficulties.

In the following a description of the simulation algorithms and its structure are given.

Generation of random gamma ray in the source

All random numbers generated by the computer are in fact pseudorandom - they are calculated according to some formula. Therefore, “random” numbers mentioned further will always be meant in such manner.

Firstly, a random origin point $(x_0, y_0, z_0 \equiv 0)$ in the slice source is generated according to uniform probability distribution (which corresponds to a homogeneous source). The coordinates have to satisfy $x_0^2 + y_0^2 \leq r_{source}^2$, where r_{source} is the radius of the source. Secondly, a random direction in three dimensional space is generated as follows. A unit vector v can be written as

$$v = (\sin \theta \cos \varphi, \sin \theta \sin \varphi, \cos \theta) \quad (70)$$

with θ and φ as defining angles. The isotropic distribution is achieved if we set

$$\begin{aligned} n_\theta &\equiv \cos \theta = \text{random} \in (-1, 1) \\ n_\varphi &\equiv \varphi = \text{random} \in (0, 2\pi) \end{aligned} \quad (71)$$

and then the vector v will be

$$v = \left(\sqrt{1-n_\theta^2} \cos n_\varphi, \sqrt{1-n_\theta^2} \sin n_\varphi, n_\theta \right). \quad (72)$$

Now the track of the photon can be described parametrically in coordinates (x, y, z) with parameter t as

$$\begin{aligned}
x &= x_0 + t\sqrt{1-n_\theta^2} \cos n_\varphi \\
y &= y_0 + t\sqrt{1-n_\theta^2} \sin n_\varphi . \\
z &= tn_\theta
\end{aligned} \tag{73}$$

Interaction in the detector

After a random gamma ray is generated we have to determine whether it reaches the upper surface of the detector (reaching the side surface of the detector is neglected). If not, the gamma ray is discarded, new one is generated and the whole process starts over. If the ray reaches the surface a distance d_{det} representing the overall length over which the ray may interact within the detector is determined (based on knowledge of the detector dimensions).

The probability $P(x)$ for a photon to pass through some material of thickness x is expressed in the well-known form

$$P(x) = e^{-\mu x}, \tag{74}$$

where μ is the total attenuation coefficient for given photon energy and material type - here sum of the coefficients for photoelectric absorption and coherent scattering $\mu = \mu_{pho} + \mu_{coh}$. In order to determine the interaction place we have to randomly generate a value for the photons free-path length. As these lengths are distributed according to eq. (74) we can use a random number ξ_1 , which is uniformly distributed on $(0,1)$, to produce the free-path lengths x_e according to the transformation [76]

$$x_e = -\frac{1}{\mu} \ln(1 - \xi_1), \tag{75}$$

If this x_e is larger than d_{det} the whole gamma ray is discarded as no interaction over the possible distance inside the detector takes place.

If the interaction takes place inside the detector we now have to determine the type of interaction. This is done with use of a uniformly distributed number $\xi_2 \in (0,1)$ and knowledge of the individual attenuation coefficients μ_{pho} and μ_{coh} . Let k be the ratio of the coefficient for scattering to the total coefficient $k = \mu_{coh} / \mu$. Then if $\xi_2 < k$ the scattering occurs, otherwise the photoelectric effect takes place and the photon is registered.

Generation of a gamma ray after coherent scattering

After the coherent scattering takes place we have to generate new direction in space of the scattered photon (the origin of its track is known - it is the interaction point). However, in this case the spatial distribution will not generally be isotropic. It will be given by the differential cross section of coherent scattering on detector Si atoms $d\sigma/d\Omega$.

Such distribution is available e.g. in [77] for energies around the desired one of 32 keV, i.e. for 20, 30 and 40 keV. We may use these distributions to obtain the one for 32 keV by quadratic interpolation. The result (normalized to angle 0°) is depicted in Fig. 39. The simulation now continues as described previously, but now the random value

$n_\theta \equiv \cos(\theta)$ is not distributed uniformly but according to the function in Fig. 39 ($d\sigma/d\Omega$ is assumed to be independent on the other angle φ).

This non-uniform distribution is obtained in the following way. A random number ξ_3 is generated according to a uniform probability distribution on the interval $(0^\circ, 180^\circ)$. Then a second random number ξ_4 is generated according to the same distribution on $(0, 1)$. A value $d\sigma/d\Omega(\xi_3)$ is calculated and if $\xi_4 \leq d\sigma/d\Omega(\xi_3)$ then $\theta = \xi_3$, otherwise the value ξ_3 is discarded and the process starts over until n_θ is successfully obtained. After the new direction in space is generated the whole simulation repeats itself from the calculation of the interaction possibility over part of the photon path which lies inside the detector volume.

The whole simulation process is repeated by means of a loop until reasonable statistics in registered counts are achieved. Then for other distances of the source to the detector the same number of loops is set in order to achieve comparable results.

Results of simulation and discussion

Tab. 20 lists all attenuation coefficients available for the photon energy of 32 keV [78] and the total coefficient, which includes the coefficients for photoelectric absorption and coherent scattering. The coefficients are given in the form μ/ρ , where ρ is the volume density of Si, which was taken to be $\rho = 2.329 \text{ g}\cdot\text{cm}^{-3}$ [79]. The dependence of the density on material temperature (the detector itself is held on liquid nitrogen temperature) can be safely neglected.

The simulation was performed for various values of distance r going from 7 mm up to 100 mm and also especially for the distances used in real measurement, which were 22.7, 26.8, 38.1 and 52.6 mm. The interpolation of results for the whole interval of values r is shown in Fig. 40 together with experimentally measured values (normalized to the value of simulation at 52.6 mm) and with the k/r^2 dependence (normalized

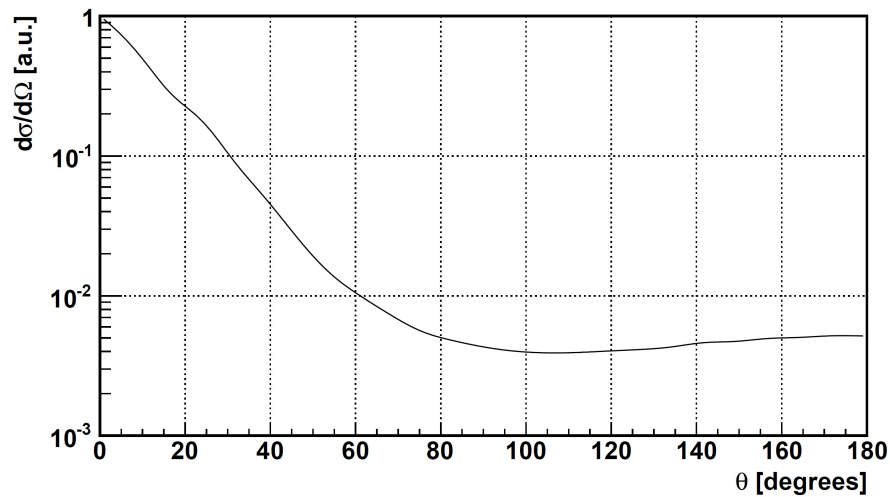


Fig. 39. Normalized (to angle 0°) differential cross section $d\sigma/d\Omega$ of coherent scattering as a function of angle for radiation energy of 32.15 keV [77]. The plot is given for scattering of photons on Si atoms.

E [eV]	$\mu_{\text{pho}}/\rho [\text{cm}^2\cdot\text{g}^{-1}]$	$\mu_{\text{coh}}/\rho [\text{cm}^2\cdot\text{g}^{-1}]$	$\mu/\rho [\text{cm}^2\cdot\text{g}^{-1}]$
32 150	0.934	0.112	1.046

Tab. 20. Attenuation coefficients for photons with energy of 32.150 keV in Si [78]. The total coefficient is taken as a sum of coefficients for photoelectric absorption and coherent scattering, which are both included in the Monte Carlo simulation.

similarly) in order to compare. In Fig. 41 a close-up on the region with experimental data is depicted. Statistical errors of the individual values are too small to be shown in the figures.

We see that the experimental data deviate from the assumed inverse square law. Use of this function is therefore not fully justified as it represents only an approximation. On the other hand, the results from the Monte Carlo simulation are much closer to the experimental data and represent almost the same behavior as in real situation. Small deviations, which can be seen for the lowest values, can be accounted for additional weak effects which were not included in the simulation, e.g. incoherent scattering, some internal detector effects, etc. Effects resulting from these phenomena were not studied as the current results are already satisfactory enough.

5.2.6. Retention measurement results and discussion

For all sources several measurements were done. The single peak of 32 keV line was described again in fit in ROOT framework with Gaussian distribution on a linear background. The results are summarized in Tab. 21. In this table the following information can be found: geometry of measurement G , i.e. distance of the solid source to the detector surface, number of measurement series for given source, retention uncorrected for the finite volume of the chamber but for the ^{83}Rb decay, correction factor Y , see eq. (64), based on inverse square dependence $1/r^2$, correction factor X , see eq. (69), based on dependence obtained from Monte Carlo simulation and final retention values calculated from eq. (69), i.e. with use of the correction factor X . No correction for random summing is needed here as in both open and closed measurements the registered count rate is very much the same.

Discussion of results

Firstly, note the correction factors Y and X in Tab. 21. It is clearly seen that without the correction for finite chamber volume (either with the inverse square law derived factor Y or the more realistic Monte Carlo simulation derived factor X) the retention results are changed by a few percent. Moreover, this correction is more significant for retention values farther from the edges 0 % and 100 %.

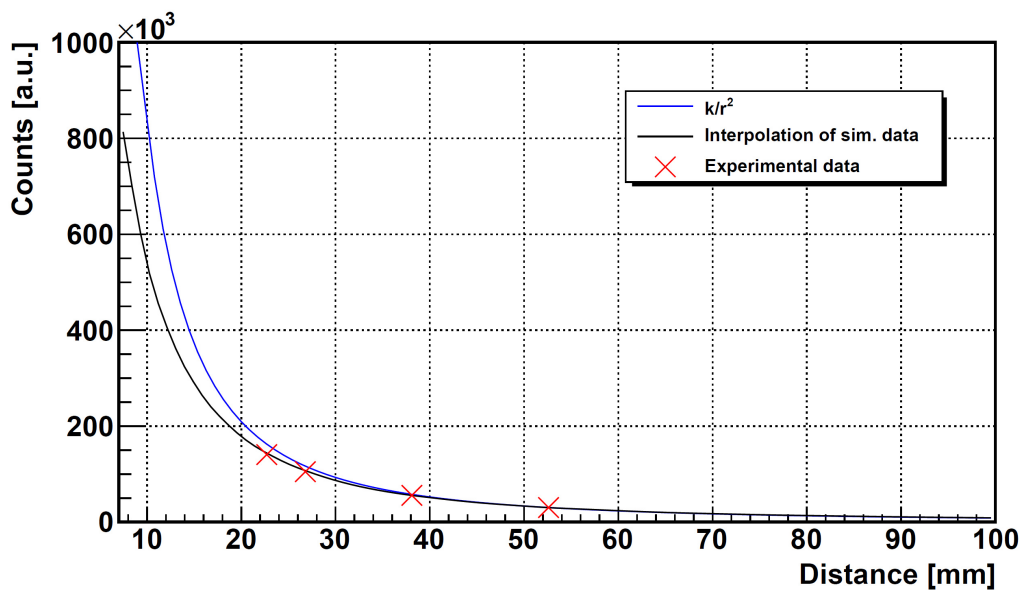


Fig. 40. Comparison of simulation results with experimental data and k/r^2 dependence of counts on distance r of the source from the detector surface. The data are normalized to the point 52.6 mm.

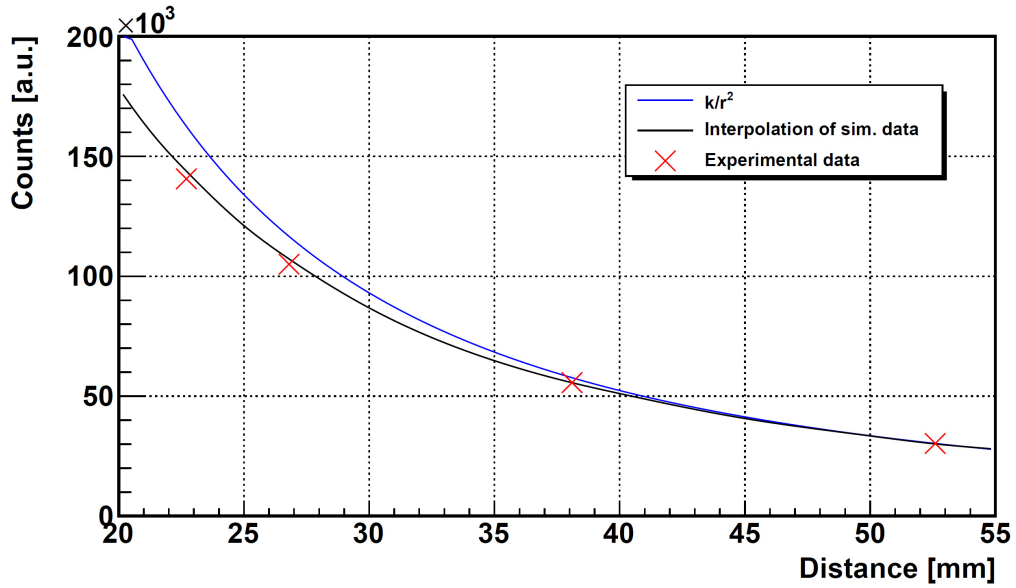


Fig. 41. Comparison of the same results as in Fig. 40, close-up on region with experimental data.

As far as the correction factors are concerned, both clearly differ from each other. This was expected already from the results in graphs in Fig. 40 and Fig. 41 as the factors are based on the dependences plotted in the figures. It is also seen that the difference between the values is larger for smaller geometry, i.e. when the source is closer to the detector. This was also expected as both dependences differ more for lower distances.

Nevertheless, this difference of correction factors is still small enough and can be neglected when determining the retention with accuracy of a few percent as we have here. Despite the fact the retention values in Tab. 19 were calculated using the factor X , the same results would be obtained using the factor Y . Any difference in the retention results would be seen for retention values of about 50 % where it manifests itself to the maximum extent.

Regarding the retention results a few remarks should be added. The sources Pt-30 #1 and Pt-30 #2 should have similar properties due to the similar material used for implantation (platinum) and also the same implantation energy 30 keV if the whole implantation process is reproducible. The results in Tab. 21 show that this is indeed realized well, although not fully as there is some small difference in the retentions. We also see when smaller implantation energy is used (15 keV) the retention for the source Pt-15 is slightly smaller compared to the other two platinum sources. This may reflect

source	G [mm]	no. of series*	retention [%] (uncorrected)	Y	X	retention [%]
S28	22.7	2	19 ± 2	1.54	1.42	26 ± 2
Pt-30 #1	22.7	2	95 ± 2	1.54	1.42	97 ± 2
Pt-30 #2	38.1	2	92 ± 2	1.27	1.22	93 ± 1
Au-30	38.1	3	89 ± 1	1.27	1.22	91 ± 1
Pt-15	22.7	1	83 ± 2	1.54	1.42	88 ± 1

Tab. 21. Obtained values for retention for the solid sources by means of method 2: closeable chamber method. The 1σ errors of the retentions are given by statistical errors of the 32 keV line areas. The uncorrected retention are values which are not corrected for finite volume of the chamber. *A series represents both an open and a closed chamber measurement of the same source.

the fact the rubidium atoms are positioned closer to surface of the source and more krypton may thus escape. The retention is, nevertheless, still very high.

On the other hand, when looking at the result for S28, which was prepared by vacuum evaporation, we see the retention is small and most of the krypton atoms escape before they decay into the ground state. This is probably caused by the fact the rubidium atoms reside on the surface and therefore it is quite easy for the krypton atoms to leave the source into free space.

5.3. Conclusion

The product of ^{83}Rb decay is the isomeric state $^{83\text{m}}\text{Kr}$ which is the source of conversion electrons. Under normal conditions it exists as a gas and may escape a solid source before it decays. Retention is a value which characterizes the portion of Kr atoms remaining in the source and thus provides valuable information about it. Two methods using gamma spectroscopy were developed to measure the retention of all the sources experimentally: measurement of intensities of 9.4 keV and 32 keV lines in $^{83\text{m}}\text{Kr}$ decay and measurement of intensity of 32 keV line by means of a closeable chamber.

For the first method a formula for retention calculation was derived and the retention was experimentally measured, the results are listed in Tab. 19. However, major systematic uncertainties were found and for platinum based sources the method was stated inapplicable due to interference between the 9.4 keV line and $L\alpha$ x-rays of platinum.

The second method relies on the fact that when a source is closed in a chamber 100 % of Kr atoms are captured and we may use the measured intensity of 32 keV line in this configuration as a reference value to determine the retention. This method showed to be much more reliable and without the systematic uncertainties which occurred in the first method. Some theoretical corrections were derived in order to obtain reliable and realistic results.

One of these corrections relies on the inverse square law for radiation intensity, which does not, however, fully correspond to our situation. To establish a better dependence a Monte Carlo simulation was programmed and its results showed to be more realistic and very close to a few experimental data measured. These simulation results were then used for improvement of the theoretical correction mentioned.

For all the five sources several measurements were done and retention values determined. The final results are summarized in Tab. 21. It was found out that all the implanted sources have high retention. On the contrary, the retention for the vacuum evaporated source was found to be low. From this point of view, the implanted sources are well-suited to be used as conversion electron sources for the monitoring spectrometer in the KATRIN experiment.

6. Conclusion

The aim of this thesis was to study the properties of the solid $^{83}\text{Rb}/^{83\text{m}}\text{Kr}$ conversion electron sources which are planned to be used for monitoring of the KATRIN experiment. The features reported were the determination of precise 9.4 keV γ -ray transition energy in $^{83\text{m}}\text{Kr}$ and the rubidium activity distribution and $^{83\text{m}}\text{Kr}$ retention in the sources.

The precise 9.4 keV γ -ray transition energy was investigated because the kinetic energy of the conversion electrons is derived apart other terms from this energy and because existing values were obtained precisely only by indirect methods, i.e. by means of electron spectroscopy. The determination was done by means of semiconductor γ -ray spectroscopy using a commercial Si(Li) detector by direct comparison of the 9.4 keV line with energetically closely spaced characteristic x-ray lines of nickel and arsenic. Systematic effects related to the atomic shell processes and proper description of lines in detector energy spectra were investigated. The energy value of 9405.8(4) eV was obtained. The energy determination procedure was tested for Ga $K\alpha_1$ line energy and a value compatible to the tabulated one was obtained. Our result improves the precision of the energy to sub-eV level compared to other γ -spectroscopy results and it is in a good agreement with previous results.

Knowledge on the rubidium activity distribution of the sources is desirable for proper alignment of the sources inside the electron monitoring spectrometer in KATRIN as well as for determination whether or not possible damages of the substrate lattice can occur. The damages can result in shifts of electron binding energies. The investigation was done by means of the Timepix position sensitive detector and the manual scan equipment. For the first case two-dimensional profiles of the sources were established and from them one-dimensional profiles were obtained. These were compared with profiles determined for the second case. Dimensions of the sources activity spots and maximum rubidium densities were then determined. Based on these densities it was stated that there is a risk for the implanted sources of high densities of ^{83}Rb which can result in doublet line structures in electron spectra. Recommendations were given in order to reduce such a risk.

The retention of krypton describes how many $^{83\text{m}}\text{Kr}$ atoms, which emit the conversion electrons, out of all produced from ^{83}Rb decay inside the source. Knowledge on the retention thus provides valuable information about the number of conversion electrons leaving the source. A closeable chamber method was developed in order to measure the retention. Several theoretical calculations were done in order to account for systematic effects. It was found out the retention is high for the implanted sources but low for the vacuum evaporated source. Together with that, retention of the sources implanted with ^{83}Rb of the same energy was found to be similar and retention of the source implanted with lower ^{83}Rb energy was found to be slightly lower. This means almost all $^{83\text{m}}\text{Kr}$ atoms produced from ^{83}Rb decay inside the implanted sources and provide high enough conversion electrons leaving the source.

With regard to high $^{83\text{m}}\text{Kr}$ retention and its reproducibility and the rubidium activity distribution properties of the implanted sources, these sources are suitable for monitoring in KATRIN and should be preferred over vacuum evaporated sources if actions are taken in order to reduce the risk for high ^{83}Rb densities. A decision on which source specifically is to be used should be made on basis of time stability of the K-32 conversion electron line. In case a new implanted source is produced it should be checked for the mentioned properties and investigations should be done if they are found not reproducing the properties reported here.

References

- [1] F. Reines, C. L. Cowan Jr., *The Neutrino*, Nature **178** (1956) 446, *Detection of the Free Neutrino: a Confirmation*, Science **20** (1956) 103, *Free Antineutrino Absorption Cross Section. I. Measurement of the Free Antineutrino Absorption Cross Section by Protons*, Phys. Rev. **113** (1959) 273.
- [2] K. Zuber, *Neutrino Physics*, Taylor & Francis Group, New York, 2004.
- [3] J. Hořejší, *Fundamentals of Electroweak Theory*, The Karolinum Press, Prague, 2002.
- [4] ALEPH, DELPHI, L3, OPAL and SLD Collaborations, LEP Electroweak Working Group, SLD Electroweak Group, SLD Heavy Flavour Group, *Precision electroweak measurements on the Z resonance*, Phys. Rep. **427** (2006) 257.
- [5] Y. Fukuda *et al.* (Super-Kamiokande Collaboration), *Evidence for Oscillation of Atmospheric Neutrinos*, Phys. Rev. Lett. **81** (1998) 1562, *Tau Neutrinos Favored over Sterile Neutrinos in Atmospheric Muon Neutrino Oscillations*, Phys. Rev. Lett. **85** (2000) 3999.
- [6] S. Fukuda *et al.* (Super-Kamiokande Collaboration), *Constraints on Neutrino Oscillations Using 1258 Days of Super-Kamiokande Solar Neutrino Data*, Phys. Rev. Lett. **86** (2001) 5656.
- [7] Q. R. Ahmad *et al.* (SNO Collaboration), *Measurement of the Rate of $\nu_e + d \rightarrow p + p + e^-$ Interactions Produced by ^8B Solar Neutrinos at the Sudbury Neutrino Observatory*, Phys. Rev. Lett. **87** (2001) 071301.
- [8] A. Suzuki *et al.* (KamLAND Collaboration), *Results from KamLAND*, Nucl. Phys. B (Proc. Suppl.) **137** (2004) 21.
- [9] K. Nakamura *et al.* (K2K Collaboration), *Status of the K2K long-baseline neutrino-oscillation experiment*, Nucl. Phys. A **663-664** (2000) 795c.
- [10] E. Fermi, *Versuch einer Theorie der β -Strahlen*, Z. Phys. **88** (1934) 161.
- [11] K. Nakamura *et al.* (Particle Data Group), J. Phys. G **37** (2010) 075021.
- [12] J. Angrik *et al.* (KATRIN Collaboration), *KATRIN Design Report 2004*, Forschungs-zentrum Karlsruhe GmbH, Karlsruhe, 2005.
- [13] S.-C. Wu, *Nuclear Data Sheets for $A = 83$* , Nucl. Data Sheets **92** (2001) 893.
- [14] F. Ajzenberg-Selove, *Energy levels of light nuclei $A = 13-15$* , Nucl. Phys. A **523** (1991) 1.
- [15] K. Zuber, *The status of the COBRA double-beta-decay experiment*, Prog. Part. Nucl. Phys. **64** (2010) 267.

- [16] R. Arnold *et al.*, *Probing new physics models of neutrinoless double beta decay with SuperNEMO*, Eur. Phys. J. C **70** (2010) 927, *Technical design and performance of the NEMO 3 detector*, Nucl. Instr. Meth. A **536** (2005) 79.
- [17] K. Zuber *et al.* (SNO+ Collaboration), *Nd double beta decay search with SNO+*, AIP Conf. Proc. **942** (2007) 101.
- [18] M. Pedretti *et al.*, *Cuore experiment: The search for neutrinoless double beta decay*, Int. J. Mod. Phys. A **23** (2008) 3395.
- [19] S. Schöner *et al.* (GERDA Collaboration), *The GERmanium Detector Array (GERDA) for the search of neutrinoless $\beta\beta$ decays of ^{76}Ge at LNGS*, Nucl. Phys. B **145** (2005) 242.
- [20] R. Barbieri *et al.*, *Neutrino masses in grand unified theories*, Phys. Lett. B **90** (1980) 91.
- [21] T. Yanagida, *Horizontal Symmetry and Masses of Neutrinos*, Prog. Theor. Phys. **64** (1980) 1103.
- [22] R. N. Mohapatra, G. Senjanović, *Neutrino Mass and Spontaneous Parity Nonconservation*, Phys. Rev. Lett. **44** (1980) 912.
- [23] S. Hannenstad, *Neutrinos in cosmology*, New J. Phys. **6** (2004) 108.
- [24] T. Weiler, *Resonant Absorption of Cosmic-Ray Neutrinos by the Relic-Neutrino Background*, Phys. Rev. Lett. **49** (1982) 234.
- [25] Z. Fodor, S. D. Katz, A. Ringwald, *Determination of Absolute Neutrino Masses from Bursts of Z Bosons in Cosmic Rays*, Phys. Rev. Lett. **88** (2002) 171101.
- [26] K. S. Capelle *et al.*, *On the detection of ultra high energy neutrinos with the Auger observatory*, Astropart. Phys. **8** (1998) 321.
- [27] J. F. Beacom, R. N. Boyd, A. Mezzacappa, *Black hole formation in core-collapse supernovae and time-of-flight measurements of the neutrino masses*, Phys. Rev. D **63** (2001) 073011, *Technique for Direct eV-Scale Measurements of the Mu and Tau Neutrino Masses Using Supernova Neutrinos*, Phys. Rev. Lett. **85** (2000) 3568.
- [28] G. W. Rodeback, J. S. Allen, *Neutrino Recoils Following the Capture of Orbital Electrons in ^{37}Ar* , Phys. Rev. **86** (1952) 446.
- [29] R. G. H. Robertson *et al.*, *Limits on $\bar{\nu}_e$ mass from observation of the β -decay of molecular tritium*, Phys. Rev. Lett. **67** (1991) 957.
- [30] E. Holzschuh, M. Fritschi, W. Kündig, *Measurement of the electron neutrino mass from tritium β -decay*, Phys. Lett. B **287** (1992) 381.
- [31] H. Kawakami *et al.*, *New upper bound on the electron anti-neutrino mass*, Phys. Lett. B **256** (1991) 105.

- [32] W. Stoeffl, D. J. Decman, *Anomalous Structure in the β -decay of Gaseous Molecular Tritium*, Phys. Rev. Lett. **75** (1995) 3237.
- [33] V. M. Lobashev *et al.*, *Direct search for mass of neutrino and anomaly in the tritium β -spectrum*, Phys. Lett. B **460** (1999) 227.
- [34] Ch. Weinheimer *et al.*, *High precision measurement of the tritium β -spectrum near its endpoint and upper limit on the neutrino mass*, Phys. Lett. B **460** (1999) 219.
- [35] V. M. Lobashev, *The search for the neutrino mass by direct method in the tritium beta-decay and perspectives of study it in the project KATRIN*, Nucl. Phys. A **719** (2003) C153.
- [36] Ch. Kraus *et al.*, *Final results from phase II of the Mainz neutrino mass search in tritium β decay*, Eur. Phys. J. C **40** (2005) 447.
- [37] R. Davis Jr., *Solar Neutrinos. II. Experimental*, Phys. Rev. Lett. **12** (1964) 303.
- [38] G. Beamson, H. Q. Porter, D. W. Turner, *The collimating and magnifying properties of a superconducting field photoelectron spectrometer*, J. Phys. E **13** (1980) 64.
- [39] V. M. Lobashev, P. E. Spivak, *A method for measuring the electron antineutrino rest mass*, Nucl. Instr. Meth. A **240** (1985) 305.
- [40] V. M. Lobashev *et al.*, *Numerical simulation of a low-energy electron electrostatic integral spectrometer with adiabatic magnetic collimation*, Nucl. Instr. Meth. A **238** (1985) 496.
- [41] A. Picard *et al.*, *A solenoid retarding spectrometer with high resolution and transmission for keV electrons*, Nucl. Instr. Meth. B **63** (1992) 345.
- [42] D. Vénos *et al.*, *The development of a super-stable standard for monitoring the energy scale of electron spectrometers in the energy range up to 20 keV*, Meas. Techniques **53** (2010) 573.
- [43] Z. Kovács *et al.*, *Excitation functions for the formation of some radioisotopes of rubidium in proton induced nuclear reactions on ^{nat}Kr , ^{82}Kr and ^{83}Kr with special reference to the production of ^{81}Rb (^{81m}Kr) generator radionuclide*, App. Rad. Isot. **42** (1991) 329.
- [44] R. B. Firestone, V. S. Shirley, *Table of isotopes*, 8th edition, John Wiley & Sons, Inc., Berkeley, 1996.
- [45] D. Vénos *et al.*, *^{83m}Kr radioactive source based on ^{83}Rb trapped in cation-exchange paper or in zeolite*, App. Rad. Isot. **63** (2005) 323.
- [46] D. Vénos *et al.*, *Precise energy of the weak 32-keV gamma transition observed in ^{83m}Kr decay*, Nucl. Instr. Meth. A **560** (2006) 352.

- [47] S. L. Ruby, R. G. Klark, L. E. Glendenin, *Internal-conversion coefficients in the decay of ^{83m}Kr* , Phys. Lett. A **36** (1971) 321.
- [48] M. de Bruin, P. J. M. Korthoven, *Low-energy gamma rays from isotopes produced by (n,γ) reactions*, J. Radioanal. Chem. **10** (1972) 125.
- [49] B. Kolk, F. Pleiter, W. Heeringa, *Internal conversion measurements on ^{83m}Kr* , Nucl. Phys. A **194** (1972) 614.
- [50] A. Kovalík, V. M. Gorozhankin, *A conversion-electron investigation of the 9.4 keV $M1+E2$ transition in ^{83}Kr* , J. Phys. G **19** (1993) 1921.
- [51] A. Picard *et al.*, *Precision measurement of the conversion electron spectrum of ^{83m}Kr with a solenoid retarding spectrometer*, Zeit. Phys. A **342** (1992) 71.
- [52] B. Ostrick, *Eine kondensierte ^{83m}Kr -Kalibrationsquelle für das KATRIN-Experiment*, Ph.D. thesis, University of Münster, 2008.
- [53] M. Slezák, *The determination of energy of the 9.4 keV gamma ray transition in ^{83}Rb decay with a precision at level of 1 electronvolt*, Bachelor thesis, Charles University in Prague, 2009.
- [54] K. Debertin, R. G. Helmer, *Gamma and X-ray Spectrometry with Semiconductor Detectors*, North-Holland, Amsterdam, 1988.
- [55] R. G. Helmer, C. van der Leun, *Recommended standards for γ -ray energy calibration (1999)*, Nucl. Instr. Meth. A **450** (2000) 35.
- [56] R. D. Deslattes *et al.*, *X-ray transition energies: new approach to a comprehensive evaluation*, Rev. Mod. Phys. **75** (2003) 35.
- [57] *ROOT, Object-Oriented Data Analysis Framework* [online], available: <http://root.cern.ch>, 2011.
- [58] L. G. Parratt, *$K\alpha$ Satellite Lines*, Phys. Rev. **50** (1936) 1.
- [59] Ch. H. Shaw, L. G. Parratt, *$K\alpha$ Satellite Lines for Elements Zn(30) to Pd(46)*, Phys. Rev. **50** (1936) 1006.
- [60] A. C. Thompson *et al.*, *X-ray Data Booklet*, 3rd edition, Lawrence Berkeley National Laboratory, Berkeley, 2009.
- [61] L. G. Parratt, *Excitation potential of $K\alpha_{3,4}$ satellite lines*, Phys. Rev. **49** (1936) 132.
- [62] Ch. Herren, J.-Cl. Dousse, *Experimental evidence for the K-LM radiative Auger effect in medium-mass atoms*, Phys. Rev. A **56** (1997) 2750.
- [63] Ch. Herren, J.-Cl. Dousse, *High-resolution measurements of the K-MM radiative Auger effect in medium-mass atoms*, Phys. Rev. A **53** (1996) 717.

- [64] A. Mühleisen, M. Budnar, J.-Cl. Dousse, *K-LM and K-MM radiative Auger effect from Kr and Xe*, Phys. Rev. A **54** (1996) 3852.
- [65] J. H. Scofield, *Exchange corrections of K x-ray emission rates*, Phys. Rev. A **9** (1974) 1041.
- [66] J. L. Campbell, T. Papp, *Widths of the atomic K-N7 levels*, Atomic Data and Nuclear Data Tables **77** (2001) 1.
- [67] J. L. Campbell *et al.*, *Analytic fitting of monoenergetic peaks from Si(Li) X-ray spectrometers*, Nucl. Instr. Meth. B **9** (1985) 71.
- [68] C. M. Baglin, *Nuclear data sheets for A = 81*, Nucl. Data Sheets **109** (2008) 2257.
- [69] X. Llopart *et al.*, *Timepix, a 65k programmable readout chip for arrival time, energy and/or photon counting measurements*, Nucl. Instr. and Meth. A **581** (2007) 485.
- [70] J. Jakubek, *Energy-sensitive X-ray radiography and charge sharing effect in pixelated detector*, Nucl. Instr. and Meth. A **607** (2009) 192.
- [71] T. Holý, D. Tureček, Z. Vykydal, *Pixelman* [online], available: <http://aladdin.utef.cvut.cz/ofat/others/Pixelman/Pixelman.htm>, Institute of Experimental and Applied Physics, Czech Technical University, Prague, 2011.
- [72] J. A. Davies, L. M. More, *Basic implantation processes in Site characterization and aggregation of implanted atoms in materials*, eds. A. Perez, R. Coussement, Plenum Press, New York, 1980.
- [73] M. Zbořil, *Development of calibration sources and upgrade of the monitor spectrometer for the KATRIN experiment*, Ph.D. thesis, University of Münster, 2011 (to be published).
- [74] S. Väisälä *et al.*, *Levels of ^{83}Kr populated in the decay of ^{83}Rb and ^{83}Br* , Phys. Rev. C **13** (1976) 372.
- [75] G. R. Gilmore, *Practical Gamma-ray spectrometry*, 2nd edition, John Wiley & Sons, Ltd., Warrington UK, 2008.
- [76] J. S. Hendricks, *A Monte Carlo code for particle transport*, Los Alamos Science **22** (1994) 32.
- [77] R. T. Brown, *Coherent photon scattering cross sections*, Atomic Data and Nuclear Data Tables **15** (1975) 112.
- [78] M. J. Berger *et al.*, *XCOM: Photon Cross Section Database* (version 1.4) [online], available: <http://physics.nist.gov/xcom>, National Institute of Standards and Technology, Gaithersburg, 2011.
- [79] J. Emsley, *The Elements*, 3rd edition, Oxford University Press, Oxford UK, 1999.